



AD-A235 579



ANALYSIS OF HIGH FREQUENCY SEISMIC DATA

by

*Hans Israelsson
Jerry Carter*

Science Applications International Corporation
Center for Seismic Studies
1300 N. 17th Street, Suite 1450
Arlington, VA 22209

31 January 1991

Scientific Report No. 2

Approved for Public Release;
Distribution Unlimited

DTIC
ELECTED
MAY 13 1991
S E D



PHILLIPS LABORATORY
AIR FORCE SYSTEMS COMMAND
HANSOM AIR FORCE BASE, MASSACHUSETTS 01731-5000

DTIC EDITION COPY

01 5 13 053

SPONSORED BY
Defense Advanced Research Projects Agency
Nuclear Monitoring Research Office
ARPA ORDER NO. 5307

MONITORED BY
Phillips Laboratory
F19628-88-C-0159

The views and conclusions contained in this document are those of the authors and should not be interpreted as representing the official policies, either expressed or implied, of the Defense Advanced Research Projects Agency or the U.S. Government.

This technical report has been reviewed and is approved for publication.

[Signature]
JAMES F. LEWKOWICZ
Contract Manager
Solid Earth Geophysics Branch
Earth Sciences Division

[Signature]
JAMES F. LEWKOWICZ
Branch Chief
Solid Earth Geophysics Branch
Earth Sciences Division

FOR THE COMMANDER

[Signature]
For: DONALD H. ECKHARDT, Director
Earth Sciences Division

This report has been reviewed by the ESD Public Affairs Office (PA) and is releasable to the National Technical Information Service (NTIS).

Qualified requestors may obtain additional copies from the Defense Technical Information Center. All others should apply to the National Technical Information Service.

If your address has changed, or if you wish to be removed from the mailing list, or if the addressee is no longer employed by your organization, please notify PL/IMA, Hanscom AFB, MA 01731-5000. This will assist us in maintaining a current mailing list.

Do not return copies of this report unless contractual obligations or notices on a specific document requires that it be returned.

UNCLASSIFIED

SECURITY CLASSIFICATION OF THIS PAGE

REPORT DOCUMENTATION PAGE

Form Approved
OMB No 0704-0188
Exp Date Jun 30, 1986

1a REPORT SECURITY CLASSIFICATION UNCLASSIFIED		1b RESTRICTIVE MARKINGS			
2a SECURITY CLASSIFICATION AUTHORITY		3 DISTRIBUTION/AVAILABILITY OF REPORT Approved for public release: Distribution Unlimited			
2b DECLASSIFICATION/DOWNGRADING SCHEDULE					
4 PERFORMING ORGANIZATION REPORT NUMBER(S) SAIC CSS Technical Report 90-03		5. MONITORING ORGANIZATION REPORT NUMBER(S) PL-TR-91-2032			
6a NAME OF PERFORMING ORGANIZATION Science Applications International Corporation	6b OFFICE SYMBOL (if applicable)	7a. NAME OF MONITORING ORGANIZATION Phillips Laboratory			
6c ADDRESS (City, State, and ZIP Code) Center for Seismic Studies 1300 N. 17th Street, Suite 1450 Arlington, VA 22209		7b ADDRESS (City, State, and ZIP Code) Hanscom AFB, MA 01731-5000			
8a NAME OF FUNDING/SPONSORING ORGANIZATION Defense Advanced Research Projects Agency	8b OFFICE SYMBOL (if applicable)	9. PROCUREMENT INSTRUMENT IDENTIFICATION NUMBER F19628-88-C-0159			
8c. ADDRESS (City, State, and ZIP Code) 1400 Wilson Boulevard Arlington, VA 22209		10 SOURCE OF FUNDING NUMBERS			
		PROGRAM ELEMENT NO 62714E	PROJECT NO 8A10	TASK NO DA	WORK UNIT ACCESSION NO AT
11 TITLE (Include Security Classification) Analysis of High Frequency Seismic Data					
12 PERSONAL AUTHOR(S) Hans Israelsson, Jerry Carter					
13a TYPE OF REPORT Scientific #2	13b TIME COVERED FROM 10/1/89 TO 10/1/90	14 DATE OF REPORT (Year, Month, Day) 1991 January 31	15 PAGE COUNT 94		
16 SUPPLEMENTARY NOTATION					
17 COSATI CODES		18 SUBJECT TERMS (Continue on reverse if necessary and identify by block number) High Frequency Ripple-Fired Quarry Blasts Regional Waveforms NORESS			
19 ABSTRACT (Continue on reverse if necessary and identify by block number) See Attached Sheet.					
20 DISTRIBUTION/AVAILABILITY OF ABSTRACT <input checked="" type="checkbox"/> UNCLASSIFIED/UNLIMITED <input type="checkbox"/> SAME AS RPT <input type="checkbox"/> DTIC USERS		21. ABSTRACT SECURITY CLASSIFICATION Unclassified			
22a. NAME OF RESPONSIBLE INDIVIDUAL James Lewkowicz		22b. TELEPHONE (Include Area Code) (617) 377-3028	22c. OFFICE SYMBOL PL/LWH		

19. Abstract

This report summarizes the work completed on high frequency seismology by the Center for Seismic Studies research staff between 1 October 1989 and 1 October 1990. The aim of the research was to characterize the high frequency content of noise and signals, and to develop methods of discriminating between mine blasts and other sources using high frequency seismic data. Data for these studies came from the NORESS small aperture array in Norway and its' high frequency (up to 125 Hz) central element. The major results of the research include:

- The upper frequency limits of teleseismic P-wave spectra for events recorded at the NORESS high frequency element were between 5 and 20 Hz.
- Path spectra for explosions from Balapan follow the attenuation models proposed by other authors (apparent $T = 0.14$) up to 15 Hz, but from 15 to 20 Hz, the attenuation of the Balapan-NORESS path spectra is greater than that extrapolated from the previous models.
- Scatter in delay times between successive blasts of a ripple-fired explosion have a deteriorating effect on spectral modulation.
- For the few blasts that are ideal, i.e., having no or negligible errors in time delays; the delay time between shots as well as the *number* of shots in the explosion can be estimated.
- The shape of wavefronts from Balapan explosions as recorded at NORESS were nearly identical for 33 events studied.
- Wavefronts from events in the northeastern section of the Balapan test site were characterized by a consistent tilt with respect to the wavefronts measured from events in the southwestern section of the test site.

TABLE OF CONTENTS

List of Figures	iv
Foreword	vii
1.1 High Frequency Content of Teleseismic P-Waves	1-1
References	1-30
2.1 Estimating Characteristics of Ripple-Fired Explosions	2-1
References	2-13
3.1 Slowness Estimation with Interpolated NORESS Data	3-1
References	3-28



Accession For	
NTIS GRA&I DTIC TAB Unannounced Justification	
By _____	
Distribution/ _____	
Availability Codes	
Dist	Avail and/or Special
A-1	

LIST OF FIGURES

Figure	Page
1.1 Amplitude response curve (in Volts per m/s) of the recording channels of the high frequency element at the NORESS array.	1-3
1.2 The paths from the events to the NORESS mini-array in Norway for data analyzed here.	1-5
1.3a Records from the NORESS high frequency element (vertical component) from a presumed underground explosion at Balapan in the Eastern Kazakh testing grounds.	1-6
1.3b Records from the NORESS high frequency element (vertical component) from a presumed underground explosion in Central Siberia.	1-7
1.3c Records from the NORESS high frequency element (vertical component) from a presumed underground explosion in the Ural Mountains region.	1-8
1.4 Comparison of P-wave spectra corrected for instrument response obtained with a standard cosine taper (10%) and with multiple window tapers for one of the events (Apr 17, 1987 at Balapan).	1-10
1.5 Standard deviation of the ratio of <i>estimated</i> and <i>actual</i> noise power spectra.	1-12
1.6 Far field displacements as a function of frequency for an explosion source model by Von Seggern and Blandford (1972).	1-14
1.7 Path spectra for Balapan test site explosions.	1-15
1.8 Relative locations of explosions in the Balapan test site.	1-17
1.9 Path spectra for two explosions in Mount Degelen and three closely spaced explosions in Central Siberia.	1-18
1.10 Path spectra for the traverse: Sinkiang-E.Kazakh-Ural Mountains- NORESS.	1-20
1.11 Schematic of ray paths for explosions along the traverse: Sinkiang-E.Kazakh-Ural Mountains- NORESS.	1-21
1.12 Path spectra for deep focus earthquakes.	1-22
1.13 Path spectra of some shallow earthquakes.	1-23
1.14 Path spectra for some events at regional distances (i.e., less than 30°).	1-25
1.15 Path spectra for PKP phases.	1-26

1.16	Range of variation for noise power spectra for the data studied here.	1-27
2.1	Local magnitudes, M_L , plotted against charges of ripple-fired explosions for two paths in Fennoscandia.	2-2
2.2	Standard deviation of time delay (in percent of delay between successive shots) as a function of shot number (after Fauske, 1990).	2-4
2.3	Time delays and charges of a ripple-fired explosion at Dala Kalk consisting of five individual blasts (from Dahle <i>et al.</i> , 1989).	2-6
2.4	Modulation functions for ripple-fired explosion defined in <i>Figure 3</i>	2-7
2.5	Examples of modulation functions for the ripple-fired explosion defined in <i>Figure 3</i> , assuming errors in scatter of delay times according to <i>Figure 2</i>	2-8
2.6	Synthetic example illustrating the computation of the autocorrelation function for the modulation function.	2-10
2.7	Estimated autocorrelations of the modulation function for two presumed ripple-fired explosions.	2-12
3.1	Epicenters of the events at the Balapan Test Site.	3-4
3.2	Examples of recorded P-waves at some of the elements at NORESS from events on Aug 2 1987 and Dec 17 1988.	3-6
3.3	Example of interpolated data values.	3-8
3.4	Maximum correlation values against distance, d , between element pairs for all events analyzed here.	3-9
3.5	Traces aligned from time delays determined to the nearest ms, for events on Aug 2 1987 and Dec 17 1988.	3-10
3.6	Difference between element corrections for events Mar 12 and Apr 17 1987 and average corrections for five events in southwestern Balapan.	3-13
3.7	Average element correction as a function of element elevation.	3-14
3.8	Average element corrections (with correction for elevation) as a function of horizontal element coordinates.	3-15
3.9	Standard deviation of azimuth error for 11 events in southwestern Balapan as a function of array ring.	3-17
3.10	Standard deviation of slowness error for 11 events in southwestern Balapan as a function of array ring.	3-18
3.11	Azimuth error (from D-ring data) as a function of theoretical azimuth for all Balapan events.	3-20

3.12 Difference between element corrections for events in northeastern Balapan (Dec 2 1984 and Nov 12 1988) and average corrections for five events in southwestern Balapan.	3-21
3.13 Perspective diagram of plane wave residuals plotted as a function of horizontal coordinates and second degree polynomial surface approximation to the residuals.	3-23
3.14 Plane wave residuals as a function of horizontal coordinates.	3-24
3.15 Lower hemisphere projection of the directions of a theoretical plane wave and apparent plane waves for the two portions of the Balapan test site.	3-25

FOREWORD

This report summarizes the work completed on high frequency seismology by the Center for Seismic Studies research staff between 1 October 1989 and 1 October 1990. The aim of the research was to characterize the high frequency content of noise and signals, and to develop methods of discriminating between mine blasts and other sources using high frequency seismic data. Data for these studies came from the NORESS small aperture array in Norway and its' high frequency (up to 125 Hz) central element. A brief description of the contents of the report are given below.

The first section is a study of the high frequency content of telesismic P-waves as recorded at the NORESS high frequency element. The data included recordings of both large underground nuclear explosions and earthquakes. The upper frequency limits of the P-wave spectra for the 33 events studied were between 5 and 20 Hz. Path spectra for explosions from Balapan follow the attenuation models proposed by other authors up to 15 Hz. From 15 to 20 Hz, the attenuation of the Balapan-NORESS path spectra is greater than that extrapolated from the previous models. Other path spectra follow the standard attenuation model with apparent $\tilde{T} \approx 0.14$, but do not have data above 15 Hz.

In the second section, data from the high frequency element at NORESS is used to estimate the characteristics of ripple-fired explosions in Fennoscandia. The assumption of equal time delays between successive blasts in a ripple-fire leads to optimistic assessments of our ability to evaluate these blasts. The few case studies that have been undertaken have had mixed success in observing any spectral modulation effects. We discuss the deteriorating effect on spectral modulation that scatter in delay times between successive blasts of a ripple-fired explosion may have. The study is based on actual observations of scatter in time delays of some explosive detonators used by the mining industry. For the few blasts that are ideal, i.e., having no or negligible errors in time delays; we present a method that estimates the delay time between shots as well as the *number* of shots in the explosion.

The third and final section of this report is a study of slowness and backazimuth estimation using interpolated NORESS data. The normal 25 ms sampling interval of the NORESS array elements was reduced to 1 ms through interpolation. This data was then used to study the characteristics of wavefronts from explosions at the Soviet test site Balapan, and provided some very interesting results. The shape of the wavefronts after making corrections for the elevations of the individual elements were nearly identical for all events studied. However, wavefronts from events in the northeastern section of the test site were characterized by a consistent tilt with respect to the wavefronts measured from events in the southwestern section of the test site. This is further evidence of the differences between these two sections of the test site.

1.1 HIGH FREQUENCY CONTENT OF TELESEISMIC P-WAVES

ABSTRACT

In this note we determine upper frequency limits of spectra for P-waves traveling teleseismic distances. Data recorded at the high frequency element of the NORESS mini-array are analyzed from 33 seismic events in various regions and of different source types. The procedure to estimate high frequency spectra using multiple window tapering in combination with multi-sample noise correction employed in this study seems to extend the upper frequency limit of the path spectra somewhat compared to conventional tapering and noise correction applied to "low" frequency double averaged array data. The P-wave spectra have upper frequency limits between 5 and 20 Hz. This limit is, to some extent, dependent on the seismic noise that varies considerably with daily and weekly cycles. The highest upper limits, around 20 Hz, were obtained from some large explosions in E. Kazakh. Central Siberian explosions and deep earthquakes in the Sea of Okhotsk had upper limits of about 13 Hz, and energy up to 10 Hz were detected for several other paths from deep earthquakes. Spectra shaped by the path are constructed by correcting for instrument response and for source effects. Such path spectra for explosions in the Balapan area fairly closely follow earlier proposed attenuation models to the upper limit of 15 Hz. In the band 15-20 Hz, however, the attenuation of the Balapan path spectra is higher than would be expected from extrapolation of the models beyond 15 Hz. The amplitude of path spectra for other teleseismic paths (30-90°) decay with frequency according to a standard attenuation model with apparent $\tilde{\tau}=0.14$. The decay is, however, often over-printed with significant undulations. Some or most of this undulation may be due to the fact that simple smooth source models were used to construct the path spectra.

1.1.1 Introduction

Recordings of very high-frequency seismic waves have recently become an area of interest for discrimination between earthquakes and explosions. A number of seismological stations have been equipped with systems for recording seismic waves with high fidelity up to and beyond frequencies of 20 Hz.

In this paper we analyze data collected at one of these high-frequency stations, the NORESS seismic array in Norway, to study the propagation of high-frequency P-waves over *teleseismic* distances. More specifically we address the question: at what high frequency limit may significant P-wave energy be detected along teleseismic paths?

The frequency band for teleseismic recordings of P-waves has traditionally been centered at frequencies around or just above 1 Hz. However, observations of significant energy at much higher frequencies have been reported for some teleseismic paths. For example, Bache *et al.* (1985) reported observable P-wave energy out to the high-frequency limit (8 Hz) of the recording system at the UK seismic arrays EKA, GBA, WRA, and YKA from nuclear explosions at the Eastern Kazakh testing grounds. The path from Eastern Kazakh to the NORESS array has also been known to be transparent to high frequency energy. Bache *et al.* (1986) and Walck (1988) reported significant energy up to 12 Hz and 15 Hz for events at Degelen Mountain and at Balapan at the Eastern Kazakh testing grounds.

1.1.2 Data

The data used here were recorded at the high frequency element of the NORESS array in Norway. The analysis is limited to data obtained at a vertical component Teledyne Geotech GS-13 seismometer placed in the surface vault at the center element (site NRAO) of NORESS. The data were sampled at 125 samples/s and the amplitude response curve of the instrument and recording system is approximately flat to velocity in the band 5 to 50 Hz (*Figure 1*).

1987 and early 1988 data were retrieved from the database at the Center for Seismic Studies for the high frequency element at NORESS. Source parameters compiled and reported by ISC for the seismic events for which data were analyzed are listed in Table 1. The paths from the event epicenters to the NORESS array are shown in the map in *Figure 2*. The events were selected on the basis of their potential to generate high frequencies and include presumed underground nuclear explosions in the USSR and China, deep earthquakes, very large shallow earthquakes, and earthquakes that were reported with a high signal to noise ratio in the NORESS daily bulletins. Some examples of recorded signals from explosions are displayed in sections of *Figure 3*.

Amplitude Response NRAO

High Frequency Element

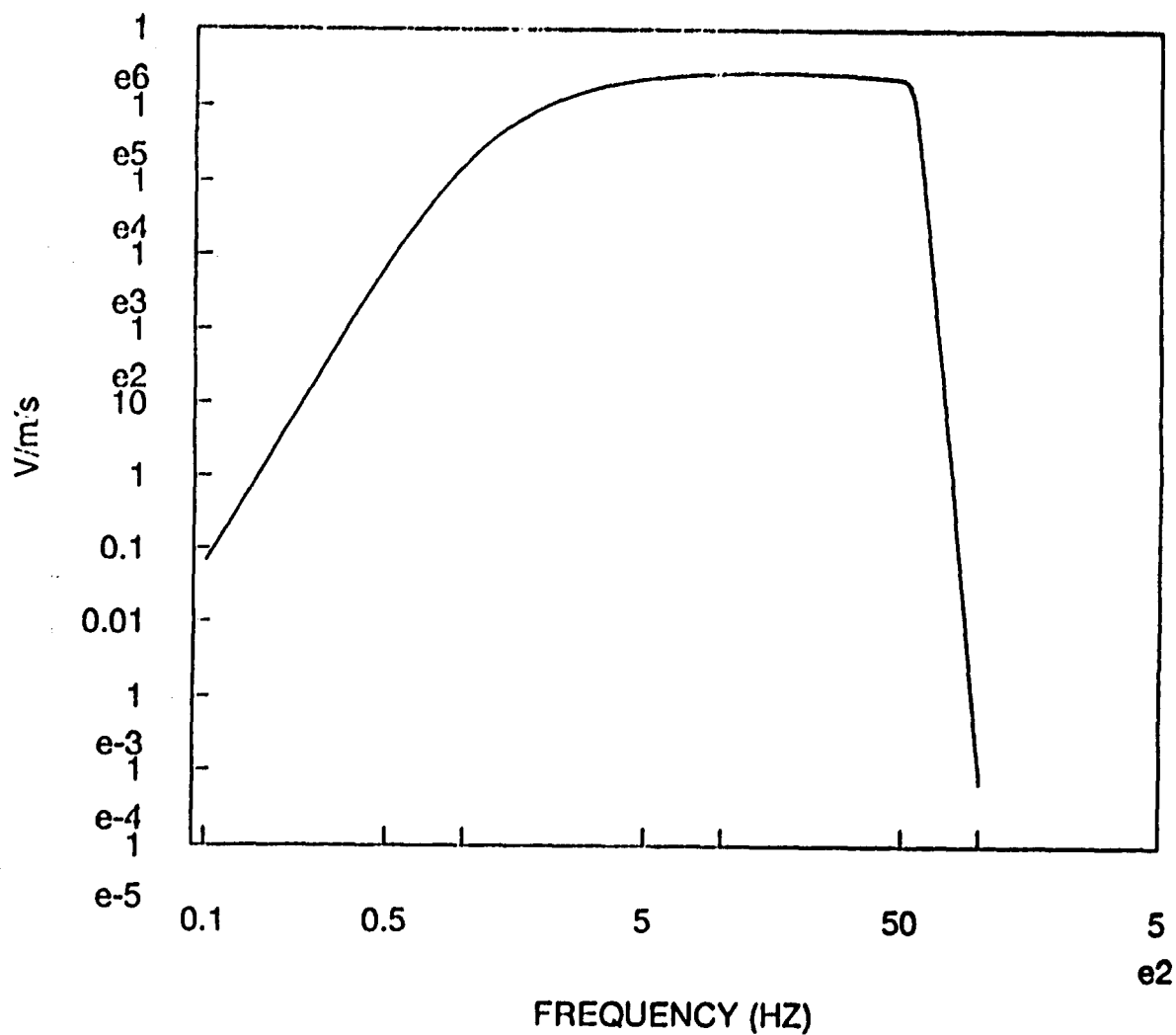


Figure 1. Amplitude response curve (in Volts per m/s) of the recording channels of the high frequency element at the NORESS array.

TABLE I

EVENT SOURCE PARAMETERS							
Date		Origin time	Latitude	Longitude	Depth (km)	m_b (ISC)	M_0 (HRVD) (Nm)
1987	Jan	5 22:52:46.5	41.96	81.32	17	5.9	$4.1 \cdot 10^{17}$
1987	Jan	14 11:03:48.7	42.57	142.85	102	6.5	$1.7 \cdot 10^{19}$
1987	Mar	3 01:32:12.3	46.35	152.01	96	5.8	$4.6 \cdot 10^{17}$
1987	Mar	9 23:58:50.4	-25.49	179.67	483	4.9	-
1987	Mar	12 01:57:17.3	49.93	78.78	1	5.5	-
1987	Apr	17 01:03:04.8	49.89	78.69	1	6.0	-
1987	Apr	19 03:59:57.1	60.52	57.08	1	4.5	-
1987	Apr	19 04:04:55.6	60.81	57.55	1	4.4	-
1987	May	6 04:02:05.7	49.83	78.13	1	5.6	-
1987	May	6 04:06:14.1	51.27	-179.90	20	6.3	$8.5 \cdot 10^{18}$
1987	May	7 03:05:49.1	46.74	139.23	430	6.0	$1.8 \cdot 10^{19}$
1987	May	18 03:07:34.1	49.28	147.69	542	6.1	$1.7 \cdot 10^{19}$
1987	May	19 00:14:33.1	29.86	139.07	417	5.5	-
1987	Jun	5 04:59:58.3	41.58	88.74	1	6.2	$2.6 \cdot 10^{17}$
1987	Jun	6 02:37:07.0	49.86	78.10	1	5.3	-
1987	Jun	10 14:50:11.5	37.23	21.47	41	5.2	$1.1 \cdot 10^{17}$
1987	Jun	20 00:53:04.8	49.91	78.74	1	6.1	-
1987	Jul	6 23:59:56.7	61.50	112.80	1	5.1	-
1987	Jul	7 18:12:53.4	-25.83	178.17	649	5.4	$2.7 \cdot 10^{17}$
1987	Jul	14 23:46:03.5	49.63	147.83	576	5.9	$8.3 \cdot 10^{17}$
1987	Aug	2 01:59:59.8	73.34	54.62	1	5.8	-
1987	Aug	10 10:52:19.9	29.87	63.84	165	5.6	$1.4 \cdot 10^{18}$
1987	Aug	12 01:29:56.8	61.46	112.76	1	5.0	-
1987	Sep	7 11:32:27.3	39.37	54.76	37	5.5	$4.2 \cdot 10^{17}$
1987	Oct	2 07:38:27.8	27.35	139.94	464	5.5	$4.9 \cdot 10^{17}$
1987	Oct	3 15:14:57.4	47.61	56.23	1	5.2	-
1987	Oct	4 18:34:22.6	55.58	161.62	54	6.0	$9.1 \cdot 10^{17}$
1987	Oct	6 20:11:35.1	52.96	159.97	34	6.1	$7.3 \cdot 10^{20}$
1987	Nov	30 19:23:19.5	58.68	-142.79	10	6.7	$7.3 \cdot 10^{20}$
1987	Dec	12 04:51:50.5	29.69	140.02	164	6.3	$3.6 \cdot 10^{18}$
1987	Dec	13 03:21:04.8	49.99	78.84	1	6.1	-
1987	Dec	27 03:05:04.7	49.86	78.76	1	6.1	-
1988	Feb	13 03:05:05.9	49.95	78.91	1	0.0	-

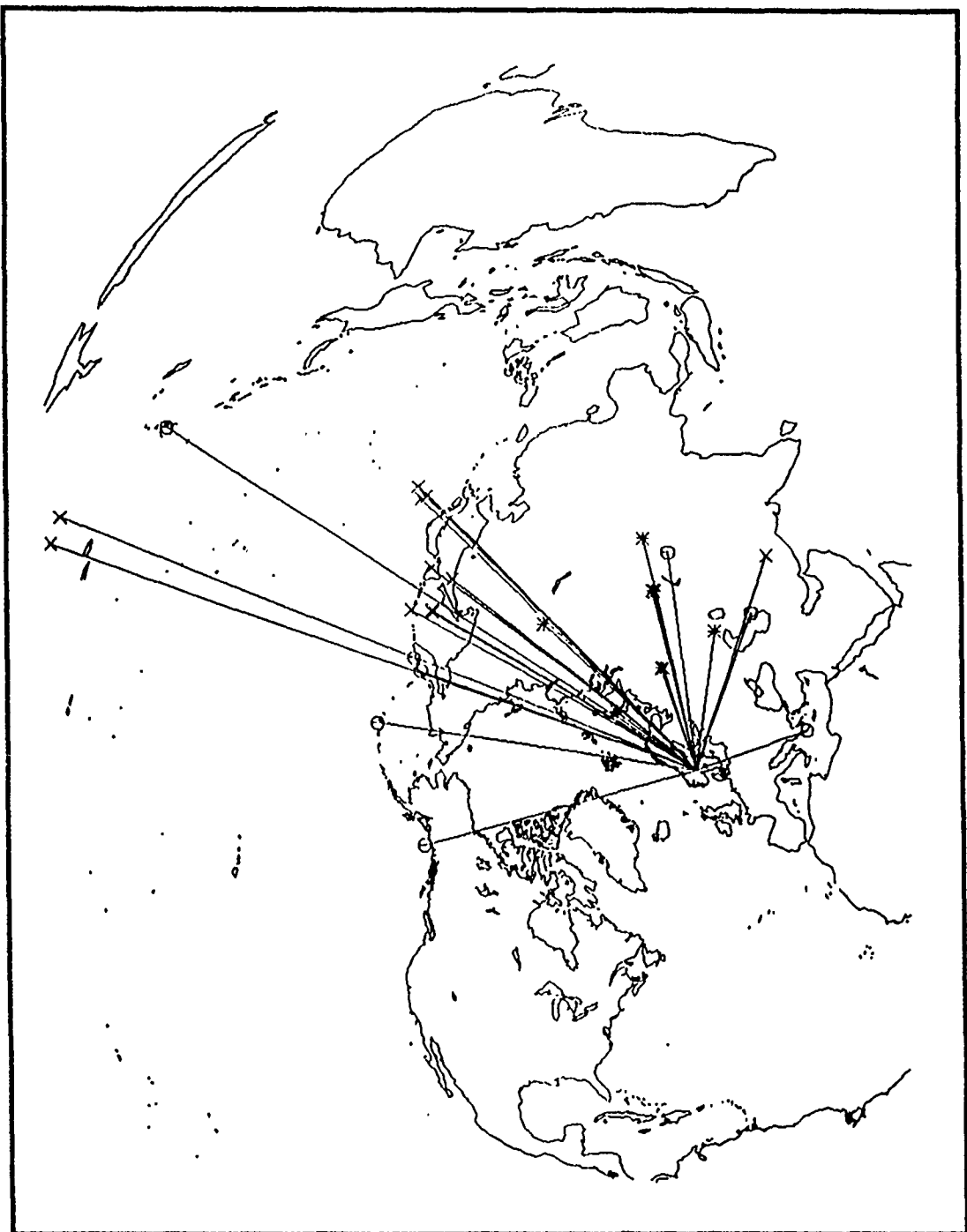


Figure 2. The paths from the events to the NORESS mini-array in Norway for data analyzed here. Asterisks, circles and crosses are used to indicate presumed underground explosions, shallow and deep earthquakes respectively.

Shagan Events at NORESS

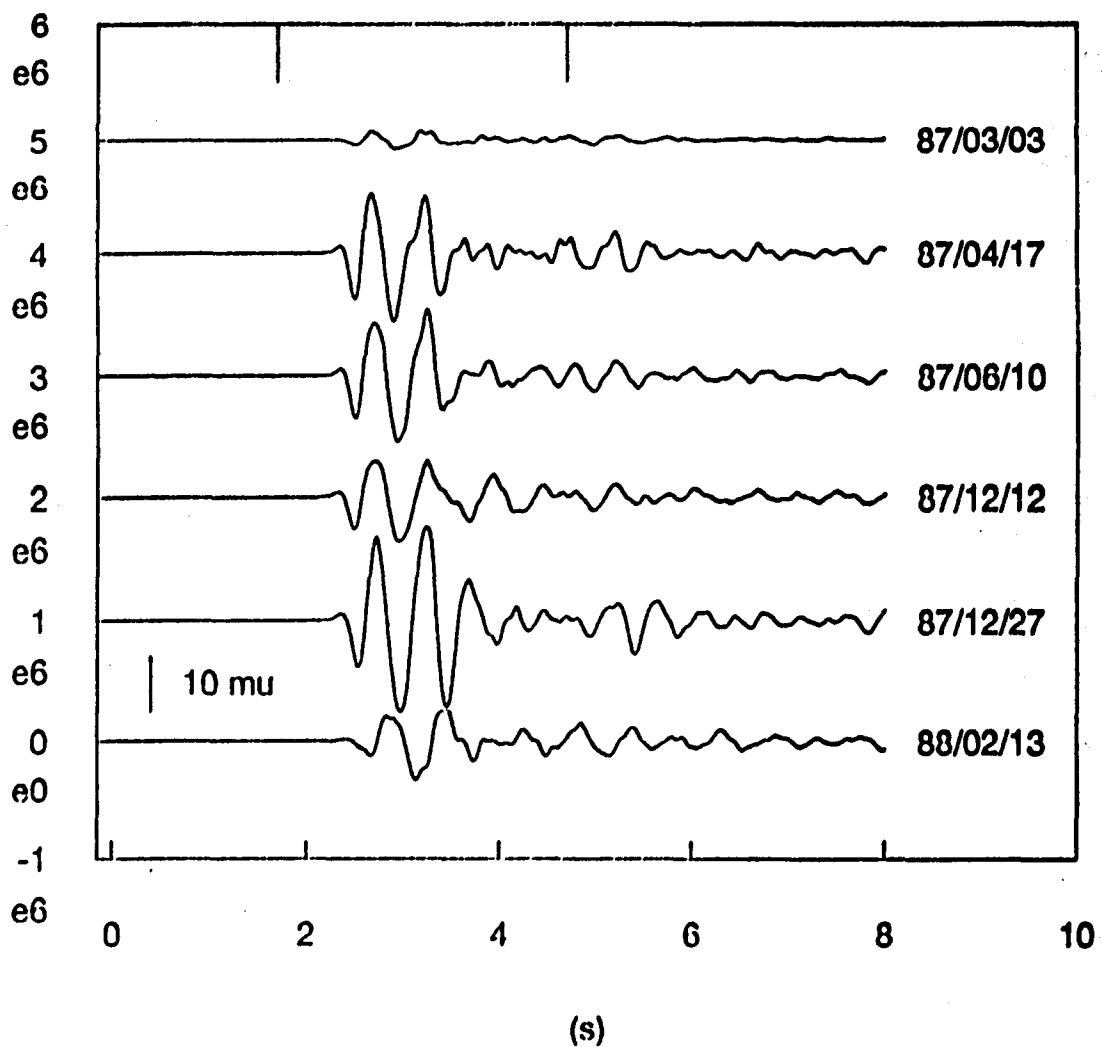


Figure 3a. Records from the NORESS high frequency element (vertical component) from a presumed underground explosion at Balapan in the Eastern Kazakh testing grounds. The timewindow used for the spectral estimates is indicated at the top of the record section. The amplitude scaling differs for the three sections.

Central Siberian Events at NORESS

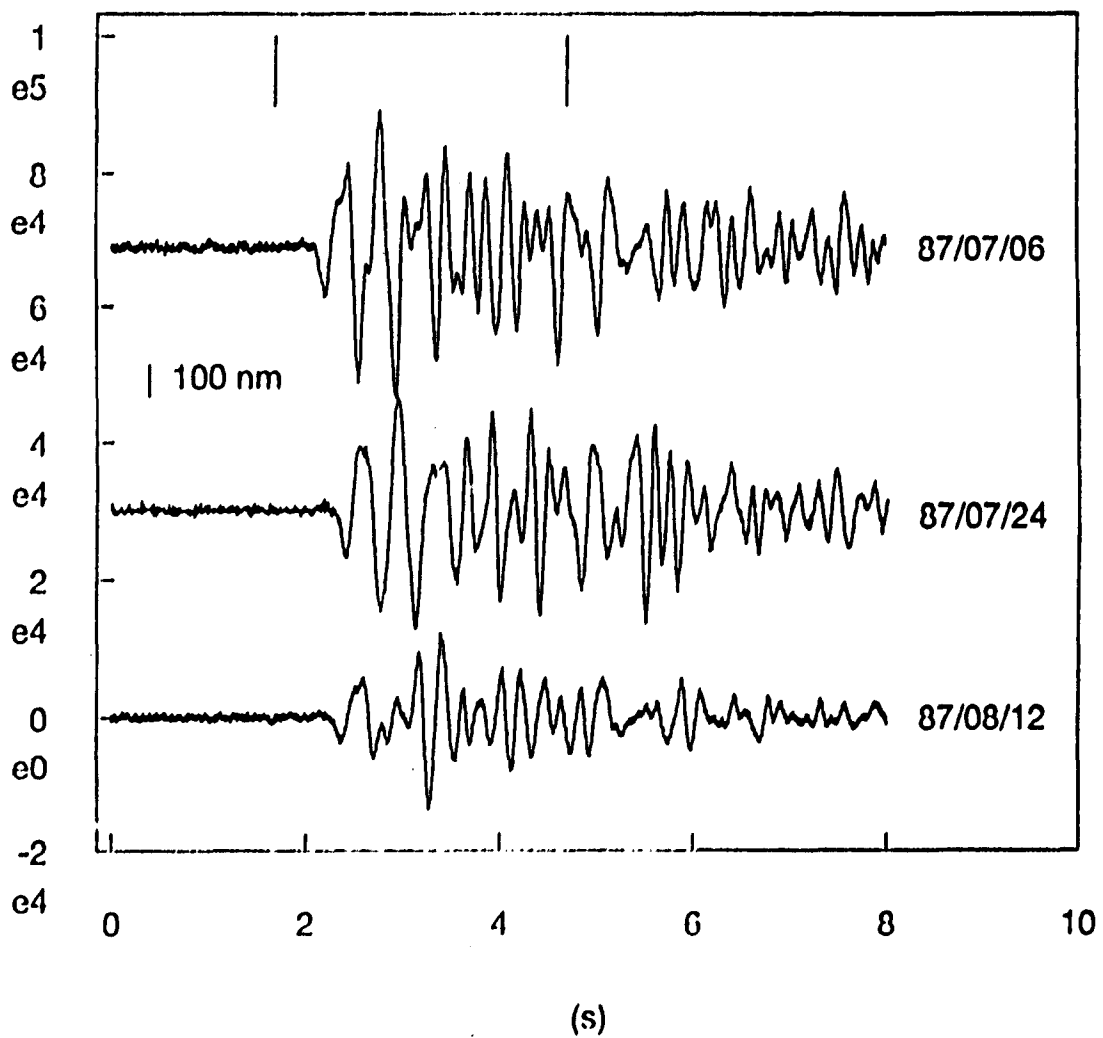


Figure 3b. Records from the NORESS high frequency element (vertical component) from a presumed underground explosion in Central Siberia. The timewindow used for the spectral estimates is indicated at the top of the record section. The amplitude scaling differs for the three sections.

Ural Events at NORESS

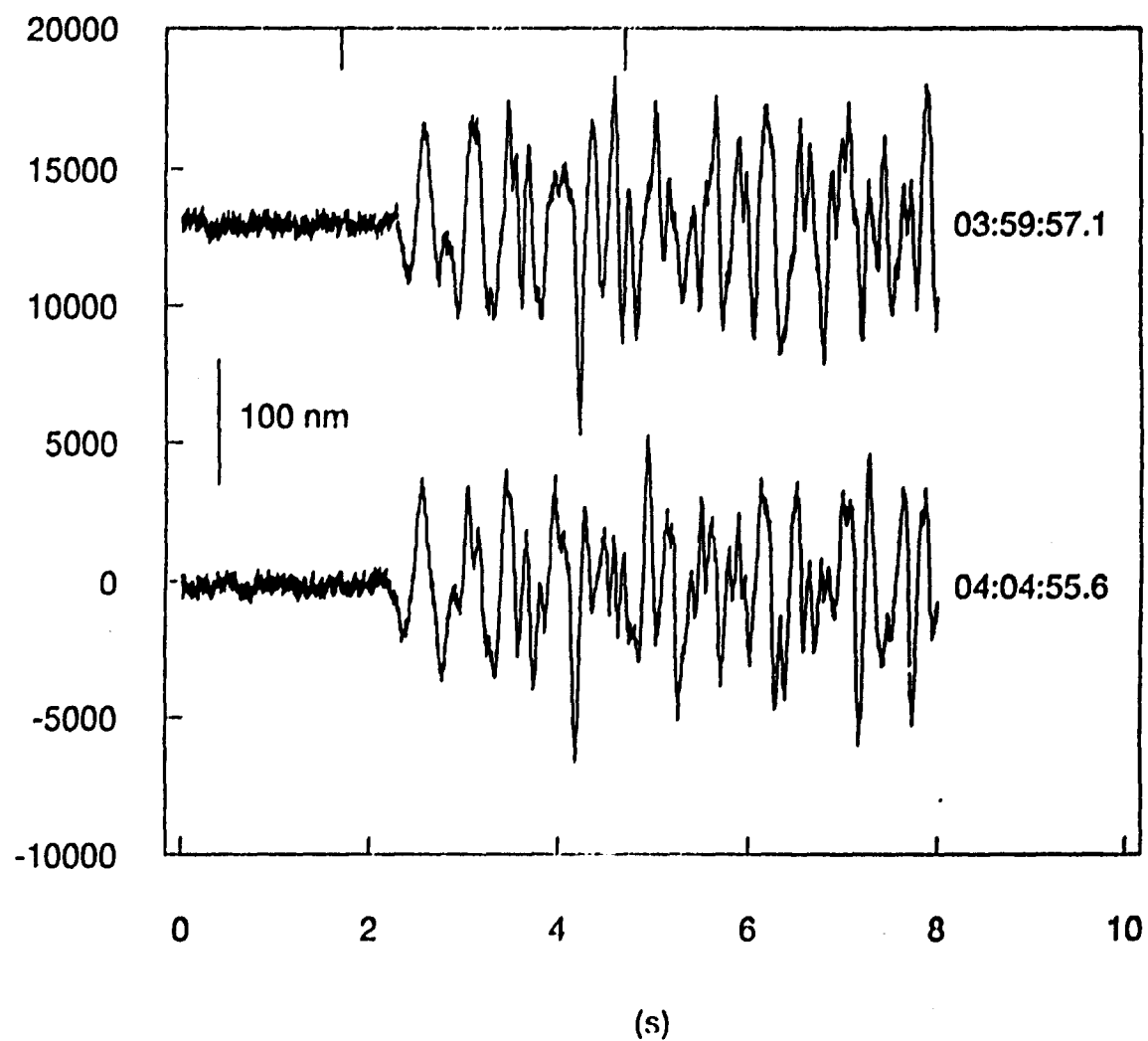


Figure 3c. Records from the NORESS high frequency element (vertical component) from a presumed underground explosion in the Ural Mountains region. The timewindow used for the spectral estimates is indicated at the top of the record section. The amplitude scaling differs for the three sections.

1.1.3 Data Analysis

An amplitude spectrum was estimated for the initial P-wave of each recorded event. The estimates were based on a 3.0 s time window to isolate the first arriving P wave pulse. The data window started 0.3 s prior to the manually read onset time. The time windows are marked on the record sections in *Figure 3*.

Spectra, calculated from the initial P wave window, were corrected for noise using the 20 s noise segment prior to the data window of the P signals. In order to optimize the trade-off between leakage resistance and variance of the spectral estimate, we used the multiple window spectral analysis method of Thompson (1982). This technique has been applied by Zhu *et al.* (1989) to teleseismic recordings of underground nuclear explosions. After some experimentation with data, the time bandwidth product was set to 4.0 in the spectral calculations.

The power spectrum of an initial P phase, $P_s(f)$, was corrected for noise according to the formula:

$$\hat{P}_s(f) = P_s(f) - \bar{P}_N(f),$$

where average noise spectra, $\bar{P}_N(f)$, is defined as

$$\bar{P}_N = \frac{1}{n} \cdot \sum_{i=1}^n P_{Ni}(f),$$

with the noise spectra, $P_{Ni}(f)$ ($i=1,\dots,6$), being calculated in the same manner as the spectrum for the initial P wave for six consecutive data windows prior to the P wave window.

Only estimates for frequencies, f , such that $P_s(f) > 2.0 \cdot \max_i(P_{Ni}(f))$, are used in the subsequent analysis. This somewhat conservative cut-off criterion should avoid any biasing noise contamination.

Single station spectra are sometimes considered to be more ambiguous than average array spectra (Bache *et al.*, 1985). The multiple window spectra technique, however, gives smoothed spectra as can be seen from the comparison of spectra calculated with multiple windows and with the 10% cosine taper that is often used (*Figure 4*).

The noise correction applied here is somewhat different from those of Bache *et al.* (1985) and Walck (1988), for example, who base their correction on one sample of noise data of about the same length as the signal window that immediately precedes the signal. Here we use an average of several consecutive noise samples ($n=6$) preceding the signal and can thereby reduce the scatter in the correction significantly. We illustrate this effect with a computational exercise on the noise data segments. Clearly the true noise contaminating a signal power spectrum, $P_s(f)$, can

COMPARISON OF SPECTRAL ESTIMATES

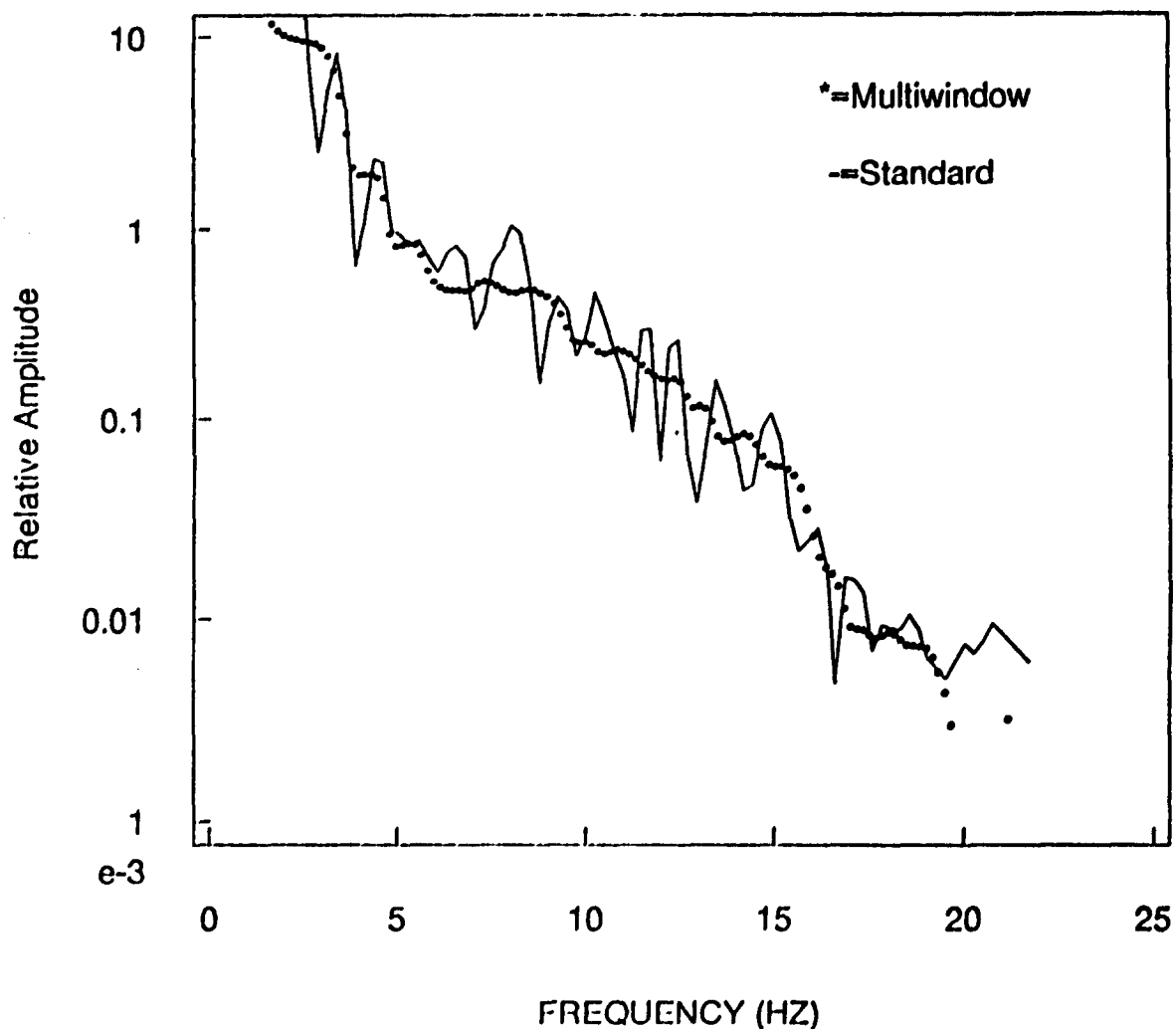


Figure 4. Comparison of P-wave spectra corrected for instrument response obtained with a standard cosine taper (10%) and with multiple window tapers for one of the events (Apr 17, 1987 at Balapan).

only be estimated and not determined exactly. We can study the quality of such a noise estimate using the noise data segments. Rather than estimating the noise portion of the signal data window, we can assume that we want to estimate the spectrum of a noise data window using only data prior to that window. The estimated noise spectrum can then be compared with the calculated spectrum for the actual noise data window. Ideally the ratio of the estimated and the calculated noise spectra should be equal to 1 regardless of frequency. The standard deviation of the ratio can be used as a measure of the quality of the noise power spectrum estimate. *Figure 5* compares the standard deviation of the ratio as a function of frequency for two estimation procedures. The upper and lower curves represent estimates obtained from one noise sample with Hanning tapering and from five consecutive samples with multiple window tapering, respectively. The latter estimation procedure reduces the standard deviation of the ratio by nearly a factor of four.

Variations among spectra based on recordings at the same station from different events in the same source area can be expected due to differing yields, depth of burial, near source geology, and contribution of secondary sources like tectonic release (Bache *et al.*, 1985). However, distinct differences among spectra from groups of closely spaced events have also been observed. Walck (1988) found that some explosions at Shagan River had a flat spectral slope between 3 and 7 Hz, whereas others decayed rather smoothly in this band. However, signals recorded under similar noise conditions from closely spaced sources of different strength are expected to have different high frequency limits, and spectral averaging of events would have to be based on weightings. For these reasons spectra for events in the same source region are not averaged.

1.1.4 Path Spectra

Following the approach of Bache *et al.* (1985), we represent the noise corrected spectra as *path* spectra, $p(f)$. The square root of the noise corrected spectrum is taken, then corrected for the amplitude response curve, $I(f)$, and the source, $D(f)$:

$$p(f) = \left(\hat{p}_s(f) \right)^{\frac{1}{2}} / (I(f) \cdot D(f)).$$

Different models have been used in the literature for source corrections, $D(f)$. Bache *et al.* (1986) and Walck (1988) use a model by Mueller and Murphy (1971), and Zhu *et al.* (1989) use a model by Von Seggern and Blandford (1972). Both of these models are mainly derived from observations at the Nevada test site. Their validity for the events studied here with regard to, for example, near source structure is unknown. Furthermore, there was no information available on parameters like shot depth and yield for the explosions in Table 1. Because of these uncertainties we employ the somewhat simpler model of Von Seggern and Blandford (1972)

Scatter in Noise Correction

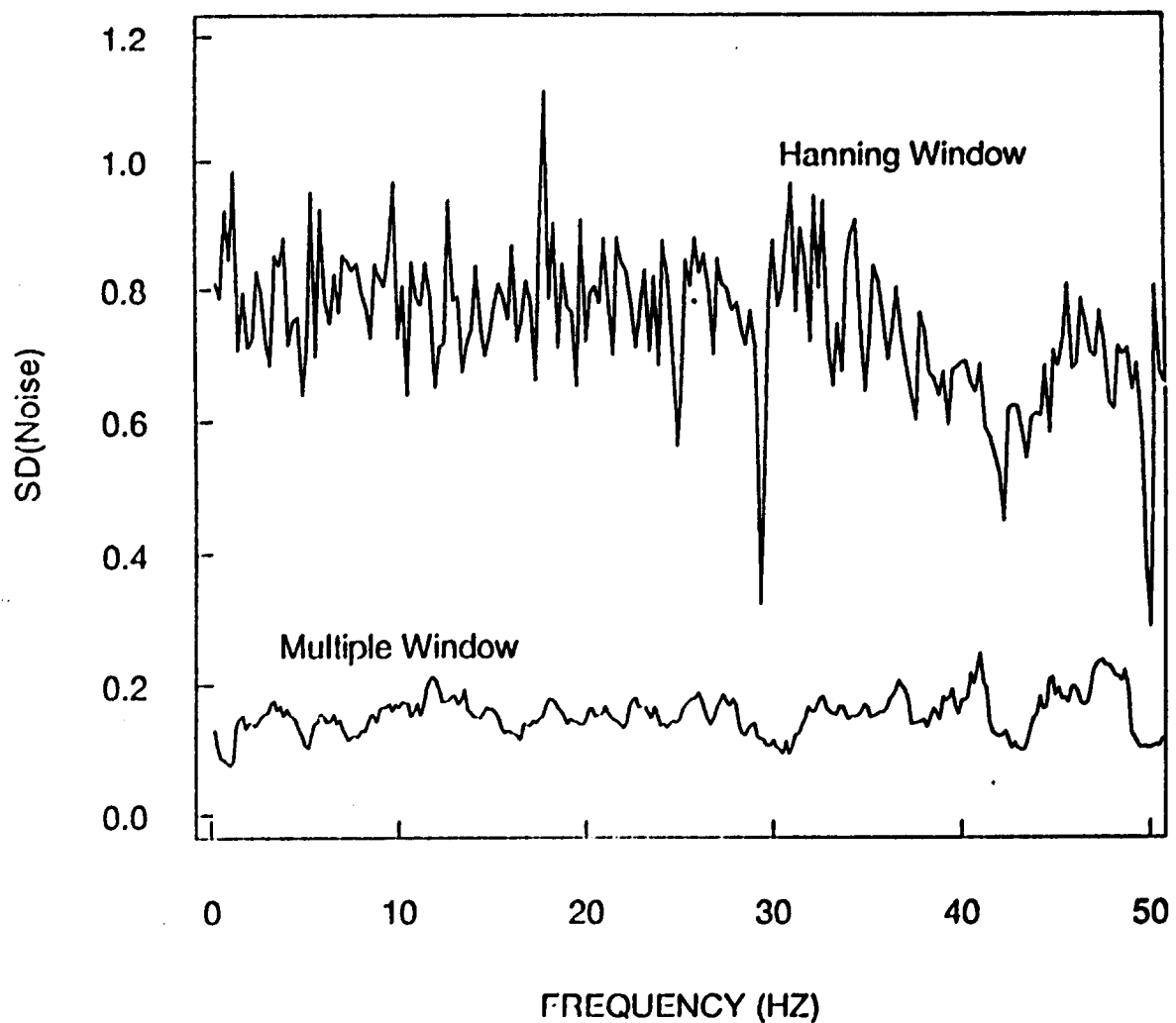


Figure 5. Standard deviation of the ratio of *estimated* and *actual* noise power spectra. The *estimated* spectrum for the upper curve is based on one data window immediately preceding the data window for the *actual* noise. Standard Hanning tapering was applied in the spectral calculations. The *estimated* spectrum for the lower curve represents an average of spectra for five data windows immediately preceding the *actual* noise. Multiple window tapering was applied in the calculations. The two curves illustrate that the combined use of several noise data windows and multiple window tapering reduces the standard deviation in the estimate of the *actual* noise significantly.

for a granitic source medium:

$$D(f) = \frac{\left(A' \cdot (2\pi f/k)^2 + 1 \right)^{1/2}}{\left((2\pi f/k)^2 + 1 \right)^{1/2}}$$

The parameters $A=4.08$ and $k=28.7276 \cdot W^{-1/3}$. The yield, W , is assumed to scale with $m_b(\text{ISC})$ according to the linear relation $m_b(\text{ISC})=4.55+0.7 \cdot \log_{10}(W)$ estimated by Vergino (1989). The m_b - yield relation is based on announced yield information for explosions in Eastern Kazakh. Reduced displacement potentials calculated for this model are shown in *Figure 6* for the magnitude range $m_b(\text{ISC})=4.5-6.0$.

Due to the relation between magnitude and corner frequency at high frequencies, the source term can be simplified for events above a threshold magnitude. The body magnitudes, $m_b(\text{ISC})$ of the explosions in Table 1, are all equal to or greater than 4.5. Bache *et al.* (1985) concluded that source corner frequency effects are contaminating path spectra for E. Kazakh explosions below 2.5 Hz or so for events with $m_b(\text{ISC})>5.4$. Bache *et al.* (1986) find that source corner effects can be seen up to 3 Hz for the small explosions at Degelen Mountain ($m_b(\text{ISC})=4.5$). The curves in *Figure 6* for the model by Von Seggern and Blandford (1972) show source corner effects around 5 Hz for $m_b(\text{ISC})=4.5$. This suggests that the path spectra obtained with $D(f)=1/f^2$ are valid at frequencies greater than about 5 Hz.

For earthquakes, we use $D(f)=1/f^2$. Table 1 includes estimates of seismic moments, M_o , of the earthquakes (HVRD solutions published in the ISC Monthly bulletins). We assume a standard omega square model for the earthquake sources, i.e., $M_o/(1+(f/f_c)^2)$, with the corner frequency f_c scaling with seismic moment as $f_c=k \cdot M_o^{-1/3}$. Using corner frequency and moment estimates for some 50 earthquakes in California, Turkey, and Tonga-Kermadec (Hanks and Boore, 1984; Molnar and Wyss, 1972), we normalize the constant $k=(1.77 \cdot 10^{16})^{1/3}$ for $f_c=1.0$ Hz. According to this corner-frequency model, the smallest seismic moment of the earthquakes studied would correspond to a corner frequency of 0.5 Hz. This means that a source correction of the form $D(f)=1/f^2$ would be sufficient for calculating path spectra for these earthquakes.

Balapan

Figure 7 shows the path spectra for six Balapan events that are compared with the hybrid model estimated by Walck (1988) for Balapan. This model assumes that the attenuation as a function of frequency, $G(f)$, can be written as:

$$G(f)=\exp \left(-2 \cdot f \cdot t_0 \cdot \tan^{-1} \left[\frac{2\pi f(t_M-t_m)}{1+4\pi^2 f^2 t_M t_m} \right] - \pi f t_1 \right)$$

Von Seggern-Blandford

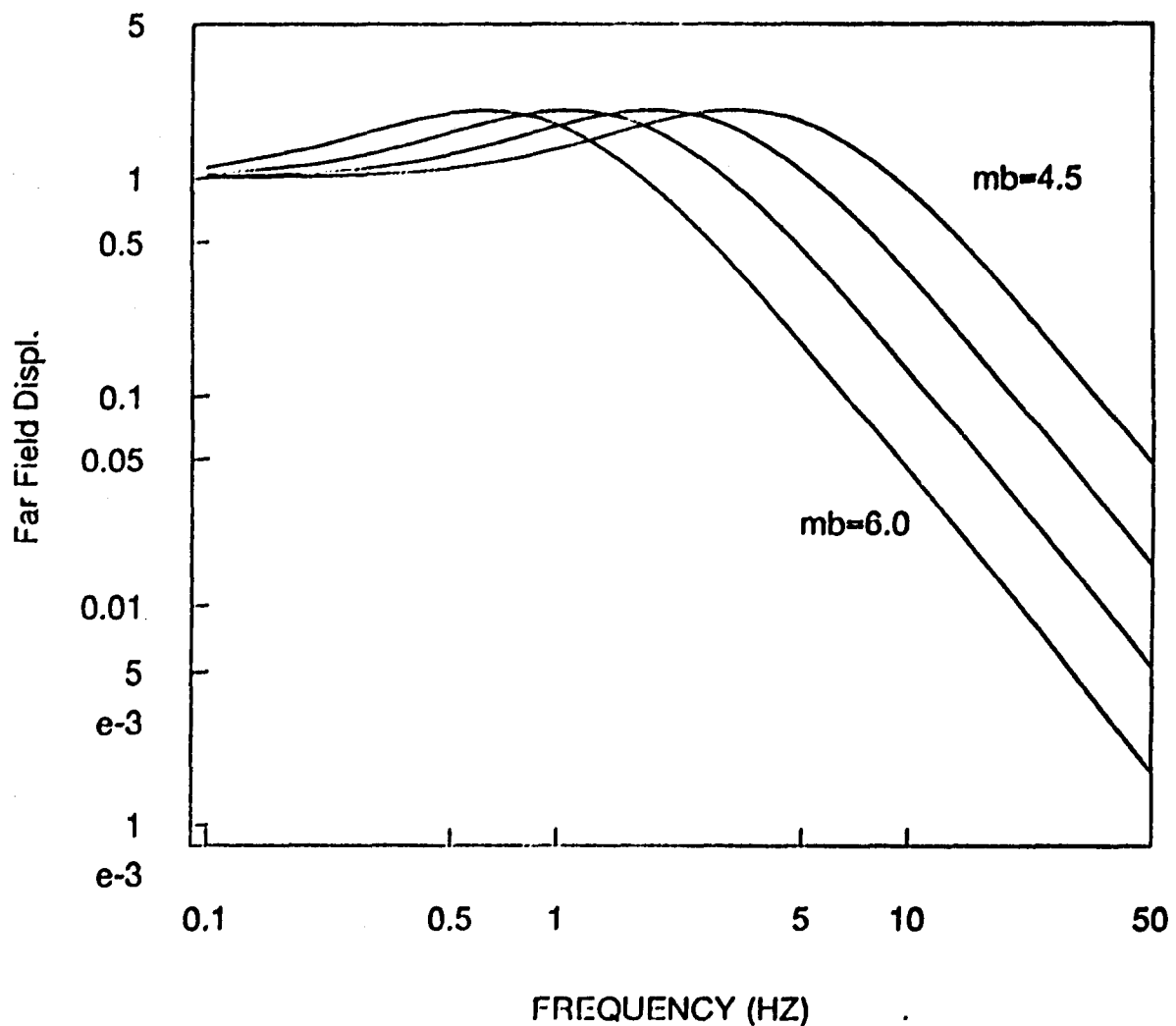


Figure 6. Far field displacements as a function of frequency for an explosion source model by Von Seggern and Blandford (1972) for m_b between 4.5-6.0. The curves are normalized to 1 at zero frequency to compare the relative location of overshoot and corner frequency as a function of source strength.

SHAGAN RIVER

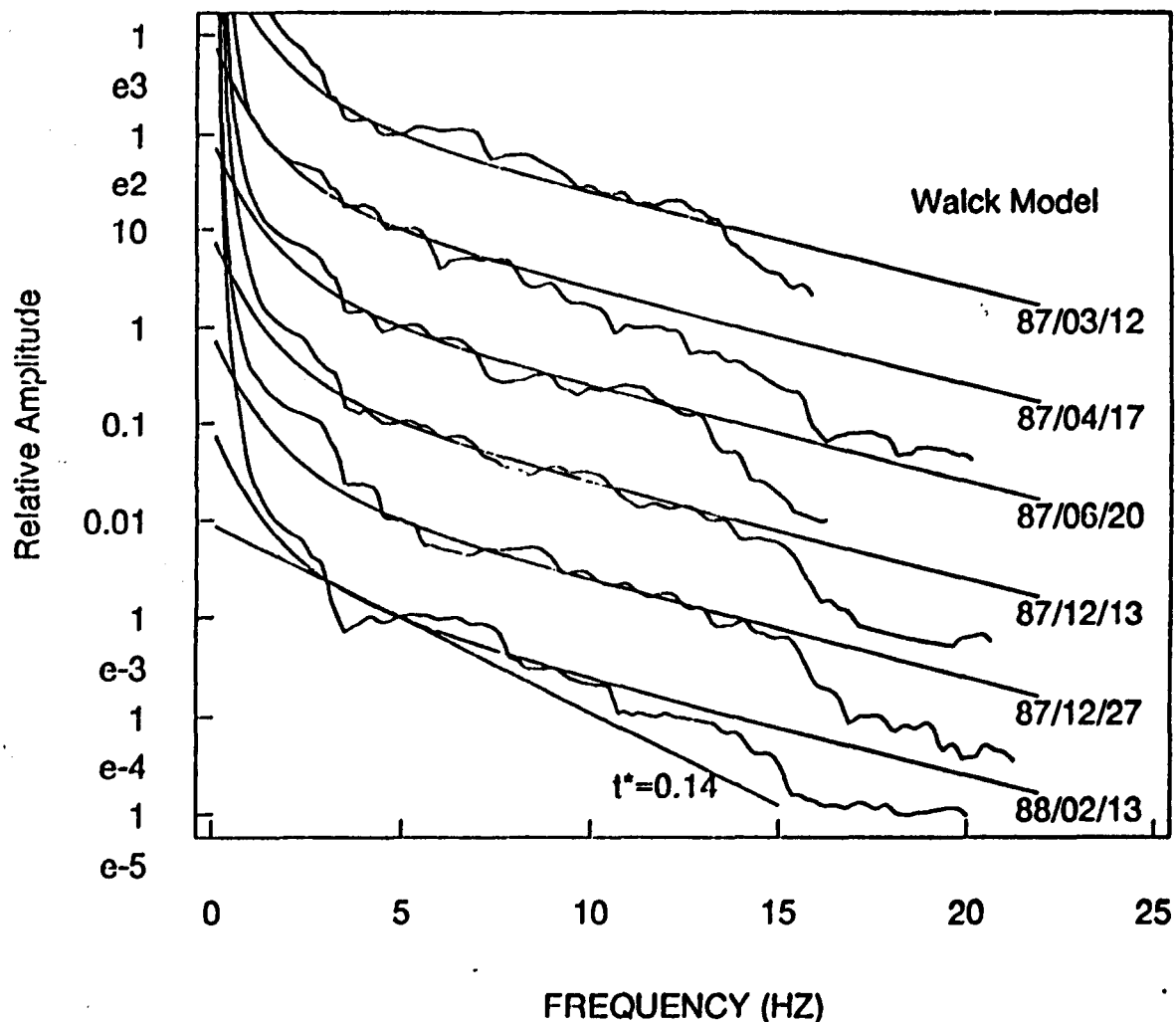


Figure 7. Path spectra for Balapan test site explosions. An attenuation model by Walck (1988) is drawn through the spectra at 5 Hz, and a standard attenuation model $t^* = 0.14$ is drawn in the lower part of the figure. The amplitude scale is arbitrary since the spectra have been shifted for clear display.

with parameter values $t_0^*=0.6$ s, $\tau_m=0.05$ s, $t_1^*=0.12$ s, and $\tau_M=10000$ s. Three of the events (87/03/12, 87/04/17, and 87/06/20) were analyzed by Walck (1988) for the NORESS array using data sampled at 40 samples/s.

All path spectra follow $G(f)$ fairly closely, i.e., $p(f) \approx G(f)$, up to some frequency between 13 and 15 Hz. However, beyond 13-15 Hz they drop off faster than $G(f)$, i.e., $p(f) < G(f)$. Clear differences among the path spectra can also be noted. The data for two of the events (87/12/13 and 87/12/27) closely follow the hybrid model up to 15 Hz, above which the attenuation increases significantly compared to the extrapolated curve for the hybrid model. Both spectra have significant energy up to and slightly above 20 Hz. The data for two other events (87/04/17 and 88/02/13) also go up to about 20 Hz. These path spectra seem to decay a bit faster than the hybrid model, $\frac{dp}{df} < \frac{dG}{df}$; but they, like the other pair of path spectra, also drop in amplitude at around 15 Hz. The remaining two events (87/03/12 and 87/06/20) contain significant energy up to about 15 Hz; and they follow the hybrid model up to around 13 Hz, above which they drop below the model.

The relative locations of the Balapan events are shown in *Figure 8*. There is no obvious correlation between shapes of the path spectra and location.

Degelen and Central Siberia

Figure 9 shows spectra for two Degelen events and three Central Siberian events. These events were also analyzed by Walck (1988) and Walck (1989) using the NORESS 40 Hz array data.

The estimated path spectra are compared with the hybrid model for Degelen estimated by Walck (1988) (with parameter $t_0^*=0.6$ s, $\tau_m=0.05$ s, $t_1^*=0.12$ s, and $\tau_M=10000$ s). The straight line corresponds to a simple attenuation model, $G(f)=\exp(-\pi f t')$ with slope $t'=0.14$, representing the apparent t' value (Der et al., 1986).

The data for the two Degelen events are in reasonable agreement with Walck's results and her estimated hybrid model. However, the spectra here go up to 15 Hz compared to 13 Hz for Walck (1988).

Similarly the spectra for the the Central Siberian events go to somewhat higher frequencies (13 compared to 12 Hz for Walck, 1989). Furthermore, they seem to decay somewhat less than predicted by a $t'=0.14$ attenuation obtained by Walck (1989). This may be due to the fact that different source models were used in calculating the path spectra. The events are rather small ($m_b(ISC) \approx 5$) and there may be some source spectrum corner frequency effect up to about 5 Hz.

SHAGAN RIVER AREA

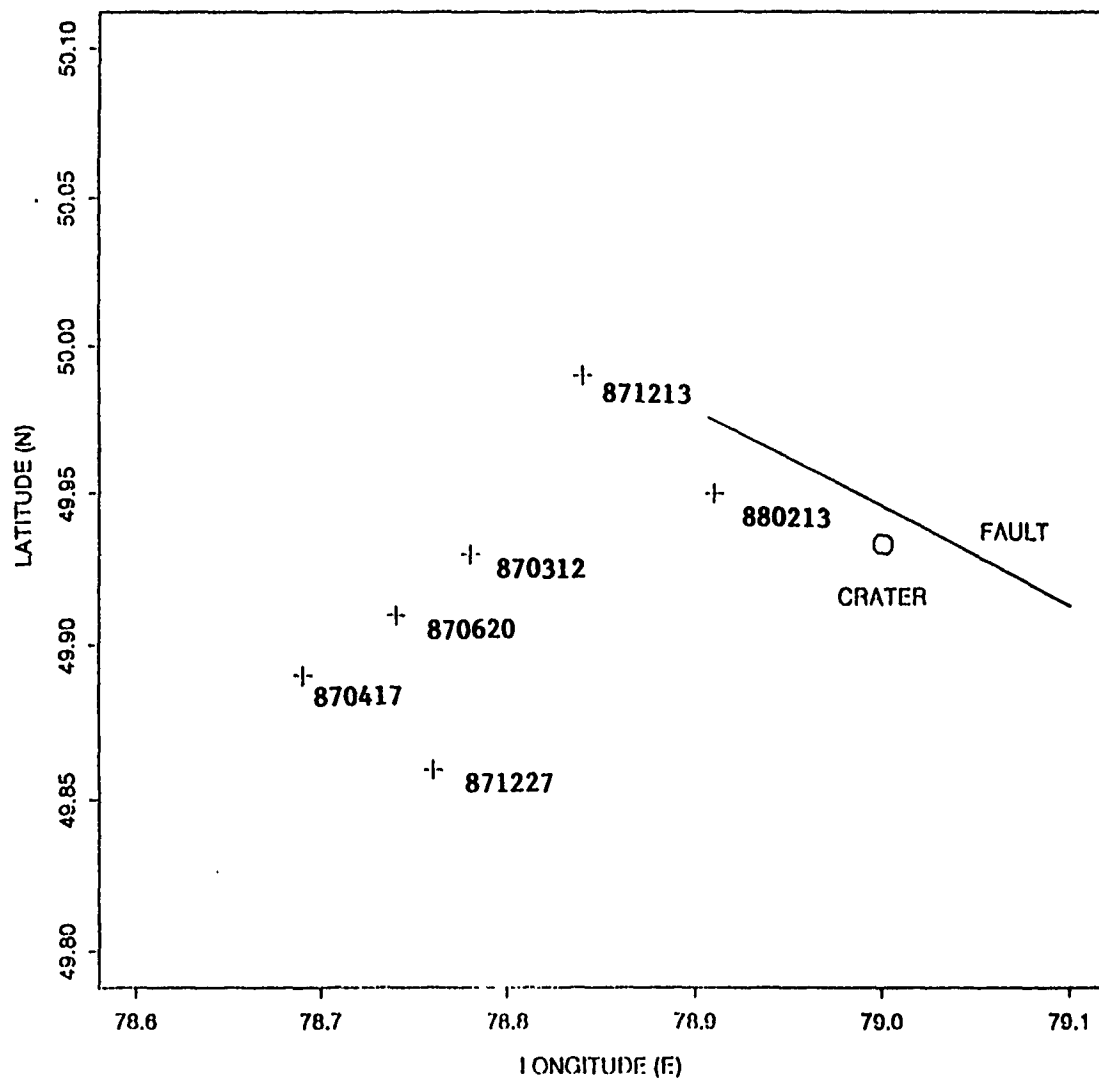


Figure 8. Relative locations of explosions in the Balapan test site.

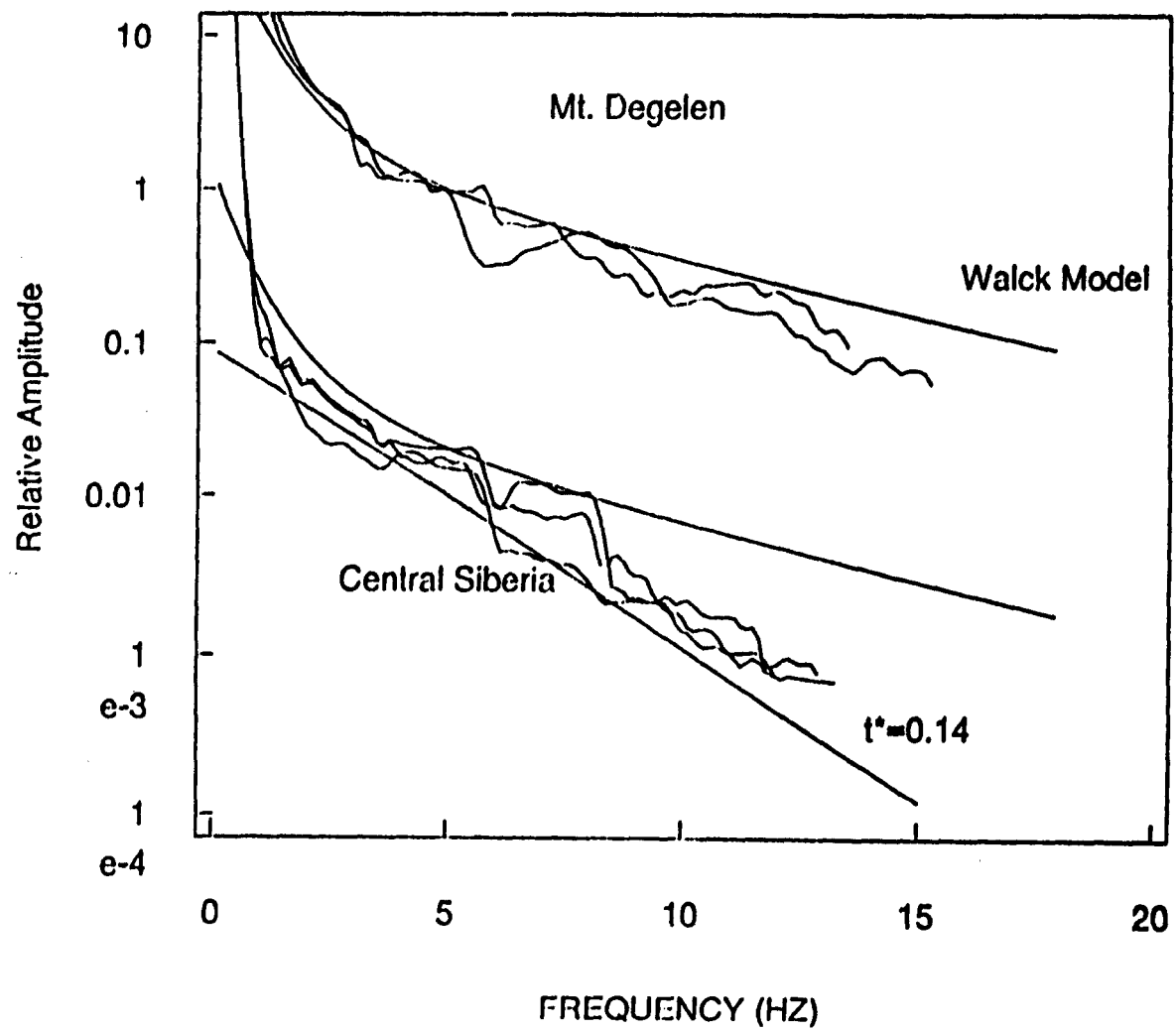


Figure 9. Path spectra for two explosions in Mount Degelen and three closely spaced explosions in Central Siberia. An attenuation model by Walck (1988) is drawn through the spectra at 5 Hz, and a standard attenuation model $t^*=0.14$ is drawn in the lower part of the figure. The amplitude scale is arbitrary since the spectra have been shifted for clear display.

Sinkiang-Kazakh-Urals-NORESS Traverse

The paths for events at the testing grounds in S. Sinkiang, E. Kazakh, and the two events in the Ural Mountains are almost at the same azimuth from NORESS (*Figure 2*). The path spectra for these explosions are compared in *Figure 10*.

The hybrid model by Walck (1988) for Balapan is drawn for comparison together with a standard attenuation model with $t^*=0.14$.

The spectra of the two Ural Mountains events are very similar and follow the Walck hybrid model fairly closely in the band 3-14 Hz, although they appear somewhat flatter than the model at frequencies below 10 Hz. It should be noted that the Ural Mountain events are much smaller in magnitude and the source corrections applied here may not be appropriate. The path spectrum for S. Sinkiang contains much less high frequencies than the Walck model. In fact, it seems to decay even faster than an apparent $t^*=0.14$. *Figure 11* shows the raypaths in the crust and the upper mantle from these sites to NORESS. The paths from Ural Mountains and E. Kazakh bottom just above the 600 and 1500 km discontinuities, respectively; and the path from Sinkiang goes just underneath the 1500 km discontinuity. A Q model by Der *et al.* (1986) has a low Q layer between 100 and 200 km (LVZ, in *Figure 11*) and a sharp increase of Q at 600 km depth. There is no obvious correlation between this Q model and the fact that the path spectra for the Sinkiang event is depleted in high frequency energy relative to those of the Ural Mountains and E. Kazakh events.

Deep Earthquakes

Figure 12 shows path spectra for the deep earthquakes analyzed here. Most of them contain significant energy: up to 10 Hz. Two events in the Se. of Okhotsk (m_b (ISC) ≈ 6.0) contain frequencies up to about 13 Hz. Most of the data follow a $t^*=0.14$ trend; however, but there is clear variations around this trend in the path spectra.

Shallow Earthquakes

The three shallow earthquakes (m (ISC) $_b=5.5-6.2$) in *Figure 13* contain significant frequencies up to about 8 Hz, but the spectra show quite a bit of variation around the attenuation $t^*=0.14$.

NORESS-URAL-E.KAZAKH-S.SINKIANG

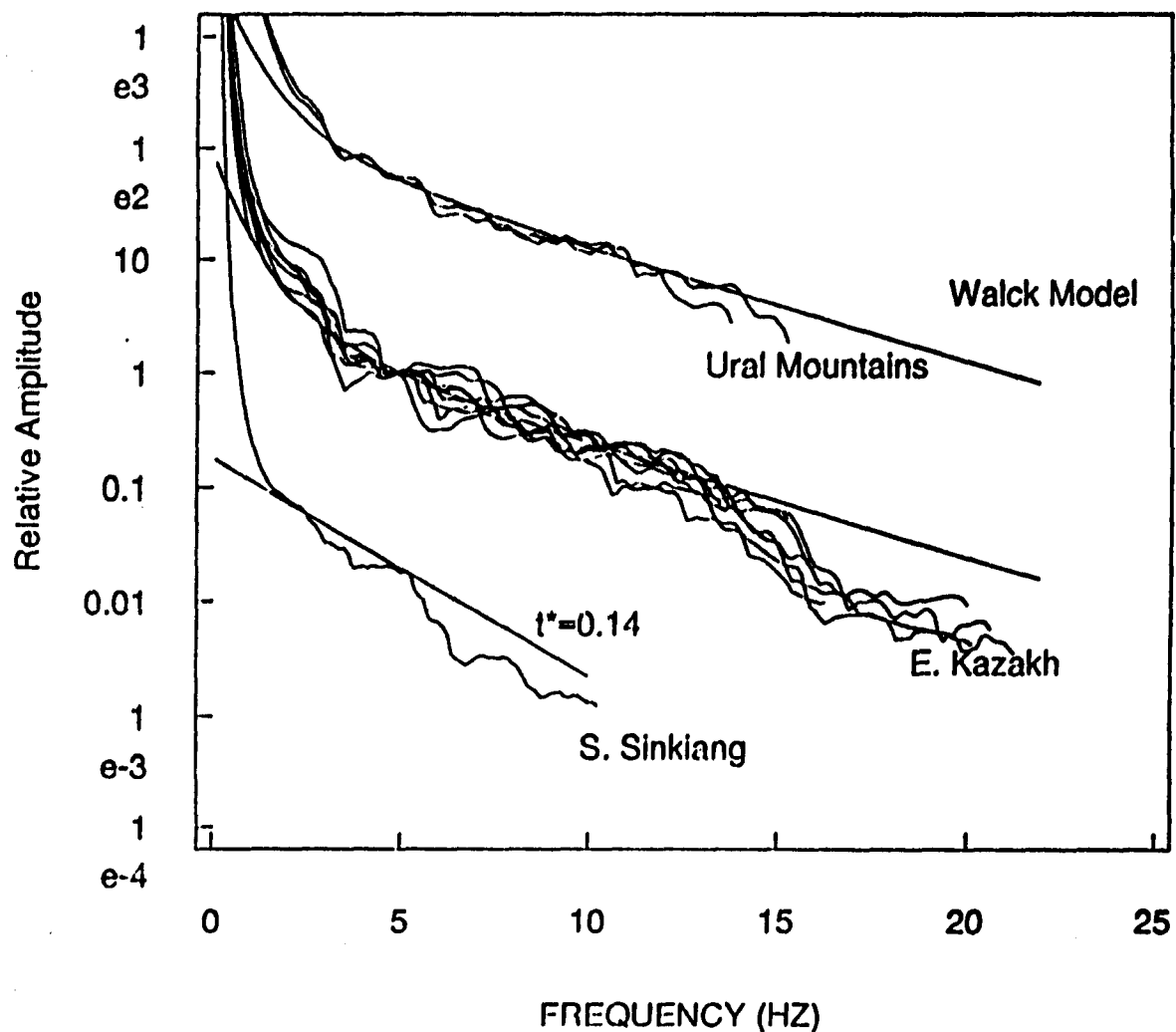


Figure 10. Path spectra for the traverse: Sinkiang-E.Kazakh-Ural Mountains- NORESS. An attenuation model by Walck (1988) is drawn through the spectra at 5 Hz, and a standard attenuation model $\bar{t} = 0.14$ is drawn in the lower part of the figure. The amplitude scale is arbitrary since the spectra have been shifted for clear display.

RAYPATHS TO NORESS

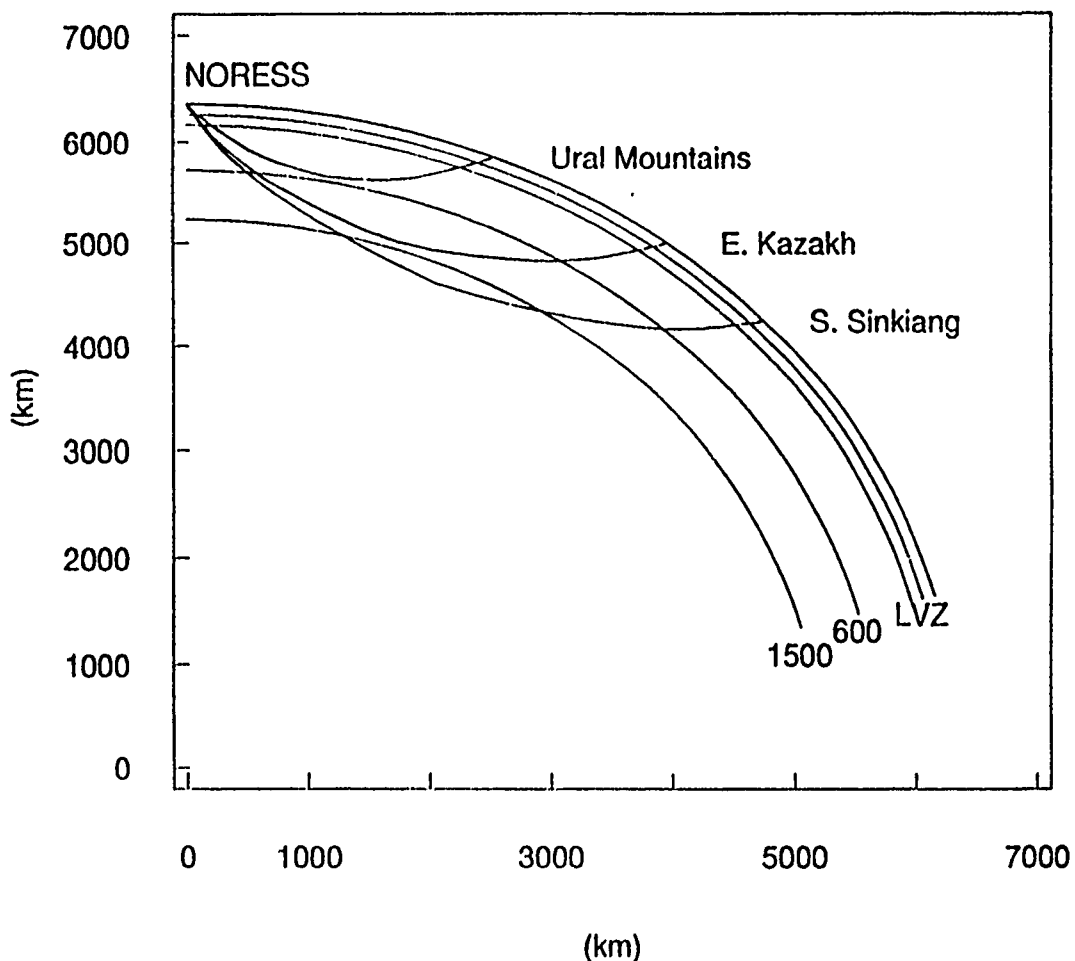


Figure 11. Schematic of ray paths for explosions along the traverse: Sinkiang-E.Kazakh-Ural Mountains- NORESS. Major discontinuities are indicated at 100-200 (marked LVZ and low Q zone according to Der *et al.*, 1986), 600 and 1500 km.

Deep Focus Events

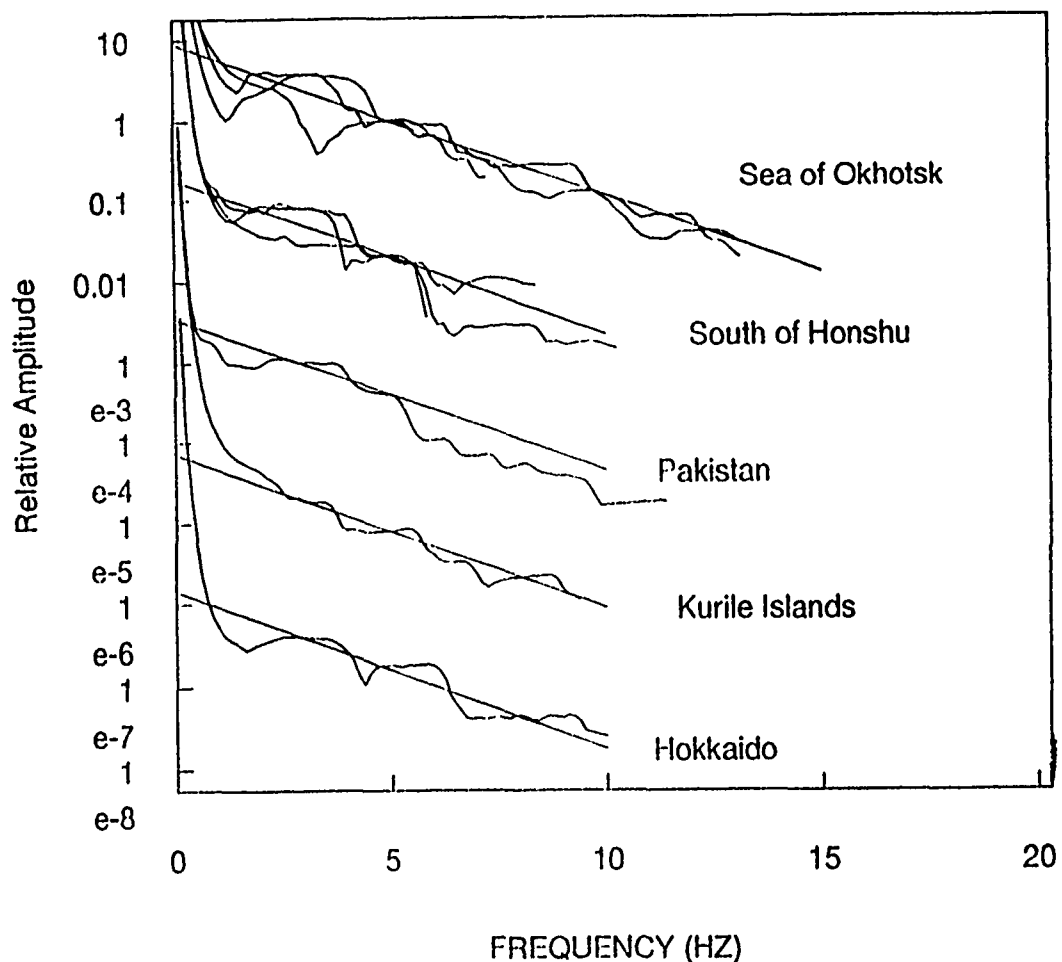


Figure 12. Path spectra for deep focus earthquakes. A standard attenuation model $\tilde{\tau} = 0.14$ is drawn through the spectra at 5 Hz. The amplitude scale is arbitrary since the spectra have been shifted for clear display.

Shallow Earthquakes

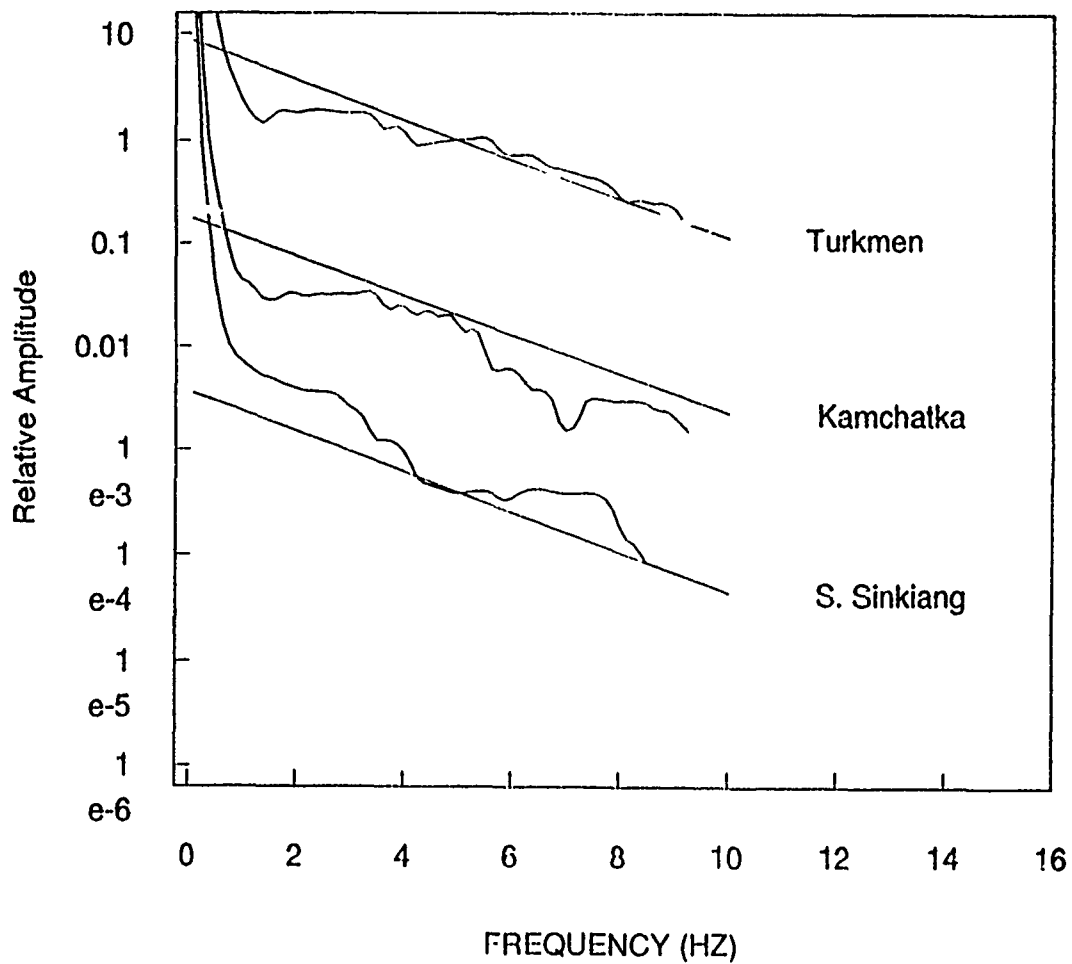


Figure 13. Path spectra of some shallow earthquakes. A standard attenuation model $t=0.14$ is drawn through the spectra at 5 Hz. The amplitude scale is arbitrary since the spectra have been shifted for clear display.

Regional Distances

Figure 14 shows path spectra for events at distances less than 30° . The explosion spectra have been corrected for source by the Von Seggern and Blandford (1972) model, and the earthquake spectrum has been multiplied by a factor of f^2 .

The events in the Ural Mountains show much less attenuation than the other events, which approximately follow a simple $t'=0.14$ model.

PKP phases

Figure 15 shows the path spectra for two deep focus events south of the Fiji Islands ($m(ISC)_b=4.9$ and 5.4) at an epicentral distance of 143.9° . There is significant energy, up to almost 10 Hz, for the larger of the two events.

1.1.5 Discussion

The path spectra for the E. Kazakh events are strikingly different from those of other events at teleseismic distances. They have the highest upper frequency limits, between 15-20 Hz.

The upper limit of the amplitude spectrum is, of course, to some extent dependent on the prevailing seismic noise level, which varies significantly in a cyclic manner with time. This is illustrated by *Figure 16*, which shows the range of variation of noise power for the data studied here. E. Kazakh explosions are usually set off early in the morning, local NORESS time, when the noise level is low.

The E. Kazakh spectra, however, appear exceptional not only with regard to upper frequency limits, but more importantly with regard to shape. They have much less amplitude decay with frequency than those of other events at teleseismic distances.

The path spectra of the two Ural Mountain explosions at *regional* distance and at virtually the same backazimuth as the E. Kazakh explosions are quite similar to the E. Kazakh spectra. For the Sinkiang explosion, also at the same backazimuth but with path lengths *greater* than the E. Kazakh events, an apparent significant depletion of high frequency energy in the path spectrum is observed. One might speculate that a high Q zone extends from NORESS to, and perhaps somewhat beyond, E. Kazakh. It should be noted, however, that the Ural Mountain path spectra are highly dependent on the assumptions of the source spectra corrections because of the small explosion sizes. The sensitivity of path spectra to assumptions about source spectra is illustrated by results for the three Central Siberian explosions. The path spectra by Walck (1989) using the source functions of Mueller and Murphy (1971)

Close Distances

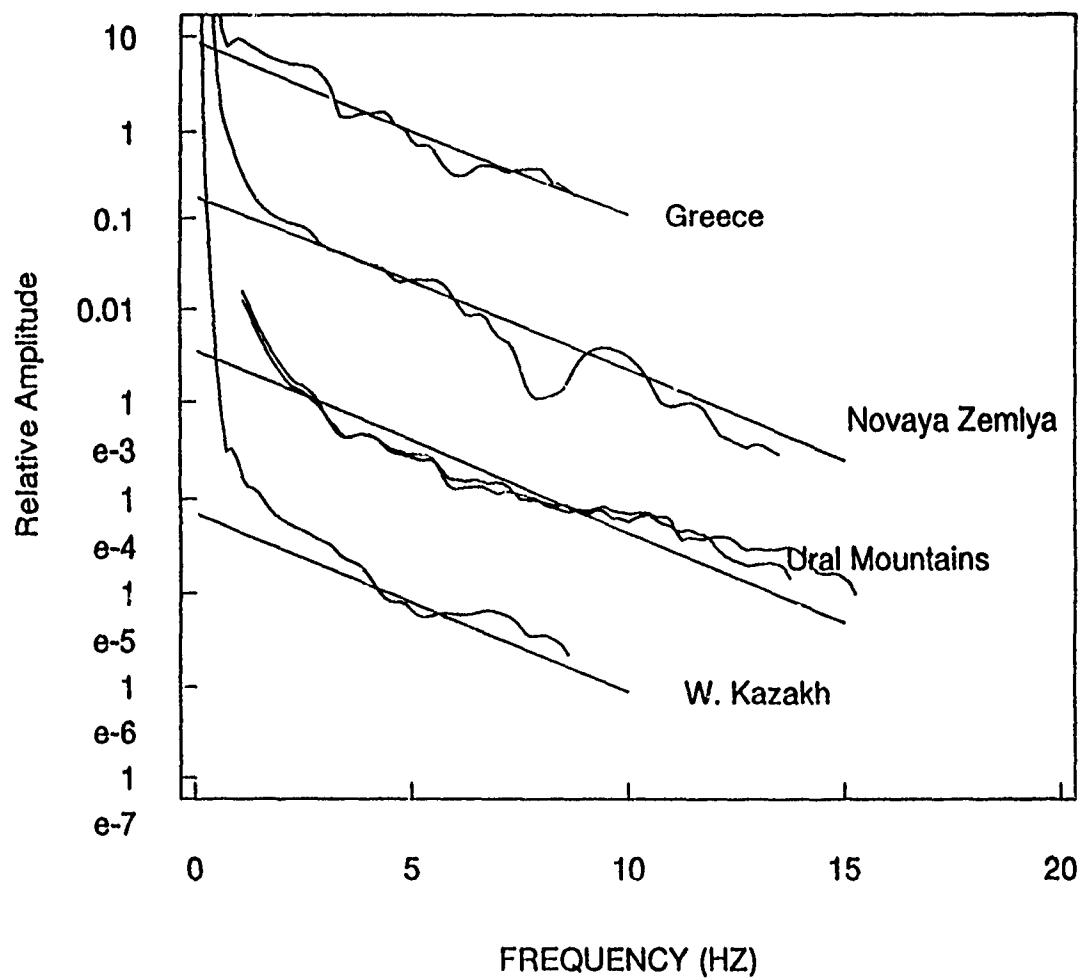


Figure 14. Path spectra for some events at regional distances (i.e., less than 30°). A standard attenuation model $\tau = 0.14$ is drawn through the spectra at 5 Hz. The amplitude scale is arbitrary since the spectra have been shifted for clear display.

PKP-South of Fiji Islands

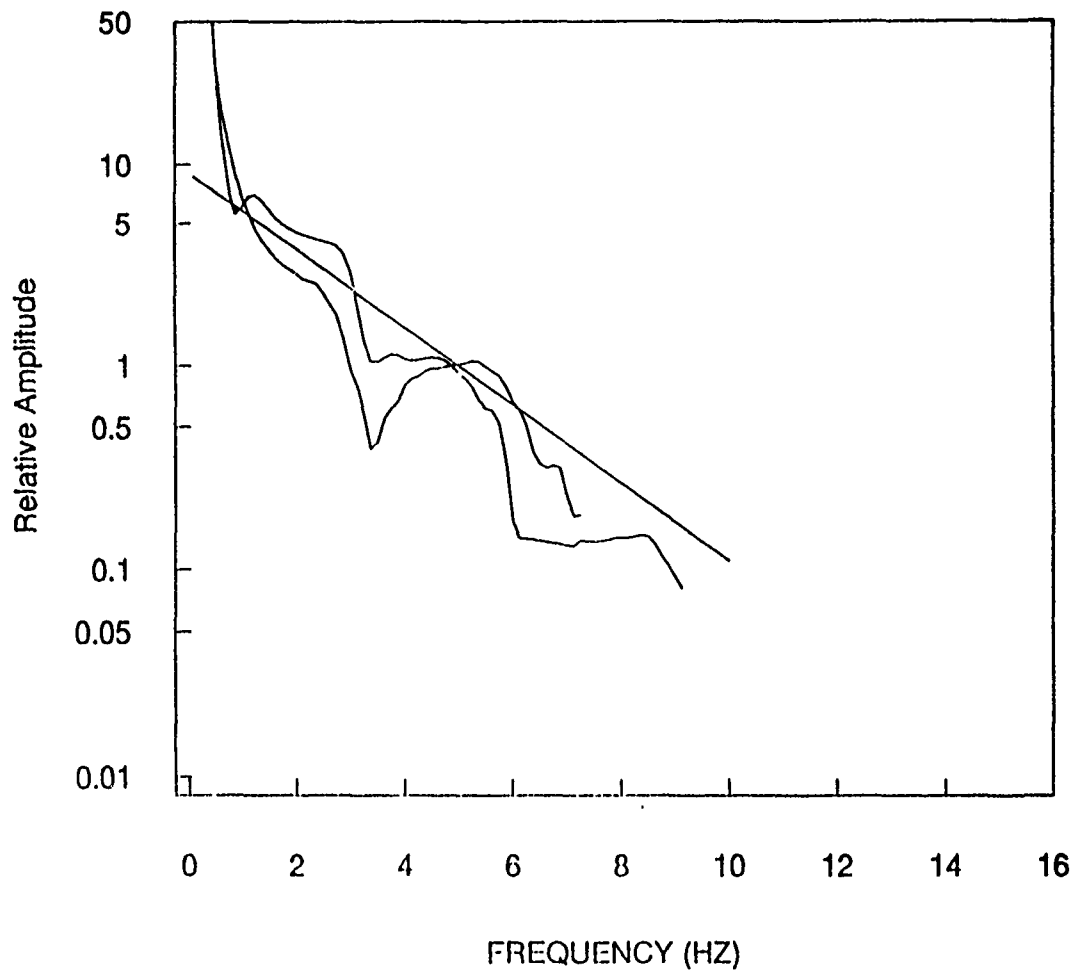


Figure 15. Path spectra for PKP phases. A standard attenuation model $\tau = 0.14$ is drawn through the spectra at 5 Hz. The amplitude scale is arbitrary since the spectra have been shifted for clear display.

RANGE OF VARIATION OF NOISE

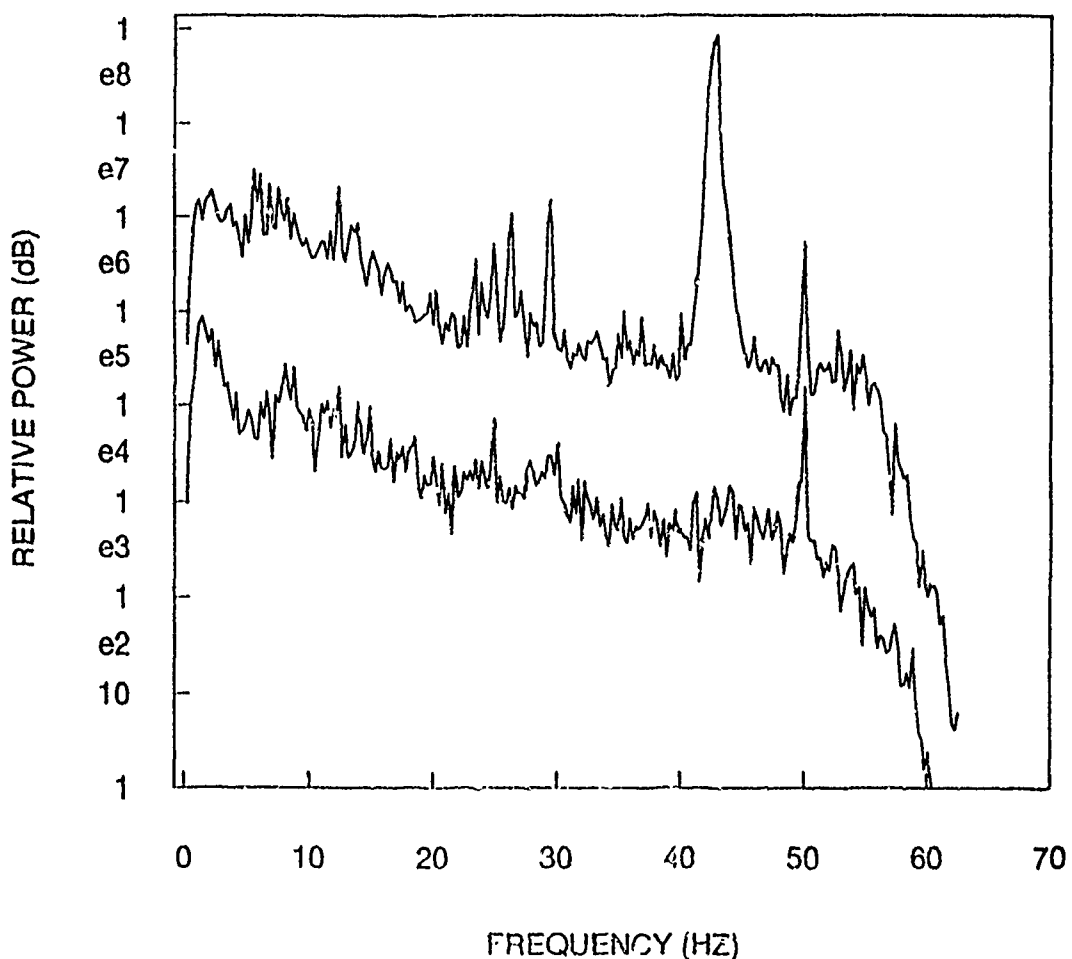


Figure 16. Range of variation for noise power spectra for the data studied here. The lower and upper curves represent minimum and maximum power taken over all individual spectra.

closely follow the standard model, $\bar{t}'=0.14$, whereas the spectra obtained here with the source function of Von Seggern and Blandford (1972) appear to be attenuated less than the standard model.

The anomalous spectral enrichment of E. Kazakh path spectra have been pointed out earlier. Bache *et al.* (1985) found that the high frequency attenuation in recordings at NORSAR for E. Kazakh events were quite different from that in recordings at UK arrays. They suggested that characteristics of the near receiver portion of the path to NORSAR must be important and that the difference for the NORSAR path appeared to be associated with some difference in the contribution of scattering to attenuation of the initial P-wave.

Walck (1989) argues, however, on the basis of the differences in NORESS/NORSAR and in UK recordings of E. Kazakh events that a region of low attenuation can not be located near the source region and that one could not further constrain its location along the remainder of the path between Eastern Kazakh and NORESS.

Walck (1989) goes on to conclude from an estimated 'normal' (i.e., $\bar{t}'=0.14$) shield attenuation for the path from Central Siberia to NORESS that since change in source region produces dramatically different path spectra at NORESS, the receiver structure immediately beneath NORESS and NORSAR is probably *not* responsible for the anomalous attenuation behavior for the E. Kazakh - NORESS path, and that a high Q zone must be located elsewhere along the path.

The study of Q is in its infancy, and results on its variation with frequency and its radial and lateral variations are afflicted with considerable uncertainties (Anderson, 1989). Der *et al.* (1986) obtain \bar{t}' values from a tentative Q-model for the shield areas of Eurasia at a distance of 60° that vary between 0.11-0.21 in the frequency band 1-10 Hz. Several of the path spectra decay largely like $\bar{t}'=0.14$ regardless of epicentral distance, at least in the teleseismic window. This is in qualitative agreement with the results of Der *et al.* (1986) and with Q increasing with depth.

Even if the path spectra for several events of different source types decay largely like $\bar{t}'=0.14$, the decay is often over-written by significant undulations. Some or most of this undulation may be due to the fact that the simplistic source models used to construct the path spectra do not adequately represent the actual source spectra. This means that the calculated path spectra are over-printed by source effects that may not readily be removed. This may make it difficult to apply source models that are smooth as a function of frequency to estimate source scaling laws.

1.1.6 Concluding Comments

In this note we determine upper frequency limits of spectra for P-waves traveling over teleseismic paths. Data recorded at the high frequency element of the NORESS mini-array are analyzed from 33 seismic events in various regions and of different source types.

The high frequency data and the procedure to estimate spectra using multiple window tapering in combination with multi sample noise corrections employed here seem to extend the upper frequency limit of the path spectra somewhat compared to conventional tapering and noise corrections applied to "low" frequency array data.

The P-wave spectra have upper frequency limits between 5 and 20 Hz. This limit is, to some extent, dependent on the seismic noise that varies considerably with daily and weekly cycles. The highest upper limits, around 20 Hz, were obtained from some large explosions in E. Kazakh. Central Siberian explosions and deep earthquakes in the Sea of Okhotsk had upper limits of about 13 Hz, and energy up to 10 Hz was detected for several other paths from deep earthquakes.

Spectra shaped by the path are constructed by correcting for instrument response and for source effects. Such path spectra for explosions at the Balapan test site area follow earlier proposed attenuation models fairly closely up to the upper limit of 15 Hz. In the 15-20 Hz band, however, the attenuation of the Balapan path spectra is higher than would be expected from extrapolation of the models beyond 15 Hz. This illustrates that extrapolation outside the frequency band of actual recording may give misleading results. Actual observations at high frequencies are important in assessing the value of high frequency data for seismic verification.

Path spectra for other teleseismic paths (30°-90°) are reduced as a function of frequency according to a standard attenuation model with apparent $\bar{t} = 0.14$.

The reduction of these path spectra is, however, often over-written by a significant undulation. Some or most of this undulation may be due to the fact that simple smooth source models were used to construct the path spectra. This undulation may not, therefore, be easily removed.

Hans Israelsson

References

- Anderson, D. L. (1989) *Theory of Earth*, Blackwell Scientific Publ., Boston.
- Bache, T., Marshall, P.D., and I.B. Bache (1985). Q for Teleseismic P waves from Central Asia, *J.Geophys.Res.* Vol. 90, pp. 3575-3588.
- Bache, T., Bratt, S.R., and H. Bungum (1986). High frequency P-wave attenuation along five paths from Central Asia, *Geophys.J.R.astr.Soc.* Vol. 85, pp. 505-522.
- Der, Z.A., Lees, A.C., and V.F. Cormier (1986). Frequency dependence of Q in the mantle underlying the shield areas of Eurasia, part III: The Q model, *Geophys.J.R.astr.Soc.* Vol. 87, pp. 1103-1110.
- Fyen, Jan (1987). NORESS noise spectral studies - Noise level characteristics, *Semi-annual Technical Summary 1 October 1986 - 31 March 1987*, pp 46-58.
- Hanks, T.C. and D.M. Boore (1984). Moment magnitude relations and theory and practice, *J.Geophys.Res.* Vol. 89, pp. 6229-6235.
- Molnar, P. and M. Wyss (1972). Moments, source dimensions, and stress drops of shallow-focus earthquakes in Tonga-Kermadec, *Phys. Earth and Planet. Interiors*, Vol. 6, pp. 263-278.
- Mueller, R.A. and J.A. Murphy (1971). Seismic Characteristics of underground nuclear detonations, *Bull. Seism. Soc. Am.* Vol. 61, pp. 1675-1692.
- Thompson, D.J. (1982). Spectrum Estimation and Harmonic Analysis, *IEEE Proc.*, Vol. 70, pp. 1055-1096.
- Vergino, E. (1989) Soviet Test Yields, *Transactions, American Geophysical Union*, Vol. 70, p. 1511.
- Von Seggern, D.H. and R.R. Blandford (1972). Source time functions and spectra from underground nuclear explosions, *Geophys.J.R.astr.Soc.* Vol. 31, pp. 83-97.
- Walck, Marianne C. (1988). Spectral Estimates of Teleseismic P-wave Attenuation to 15 Hz, *Bull. Seism. Soc. Am.* Vol. 78, pp. 726-740.
- Walck, Marianne C. (1989). P-wave attenuation from Siberia to Norway, *Bull. Seism. Soc. Am.* Vol. 79, pp. 910-913.
- Zhu Taipei, Kin-Yip Chun, and Gordon T. West (1989). High Frequency P-wave

Attenuation Determination Using Multiple-Window Spectral Analysis *Bull. Seism. Soc. Am.*, Vol. 79, pp. 1054-1069.

2.1 ESTIMATING CHARACTERISTICS OF RIPPLE-FIRED EXPLOSIONS

2.1.1 Introduction

Identifying large numbers of chemical explosions for mining and other industrial purposes presents a major challenge to seismic verification systems operating in the low magnitude range: 2.0-2.5. In a study of mine blast activity, Richards *et al.* (1990) estimated that in 1987 there were about 15,000 chemical explosions in the U.S., virtually all ripple-fired, with charges larger than 50 tons. The data in *Figure 1*, showing ML magnitudes and explosion charge for some ripple-fired explosions in Scandinavia, indicate that magnitudes between 2-2.5, indeed, correspond to charges of 50-100 tons.

Some methods of identifying ripple-fired explosions draw upon the assumption of equal time delays between successive blasts in a ripple-fire. In theory, spectra of recorded signals will then be overprinted by a modulation pattern that should be easily observed and that directly relates to the time delay between blasts (see e.g., Baumgardt, 1988). Case studies with these methods have, so far, been limited to small numbers of events compared to the scale of the overall activity of chemical explosions (Baumgardt, 1988; Smith, 1989; Hedlin *et al.*, 1989; Kim *et al.*, 1990). Furthermore, these studies appear to have had mixed success in observing any spectral modulation effects. In some cases, accurate and independent information on the characteristics of the mining explosions is not available to confirm conclusions from observed spectral modulation.

In this note we discuss the deteriorating effect on spectral modulation that scatter in delay times between successive blasts of a ripple-fired explosion may have. The study is based on actual observations of scatter in time delays of some explosive detonators used by the mining industry. In addition we present a method attempting to estimate the autocorrelation for the modulation function of an *ideal* ripple-fired explosion, i.e., having no or negligible errors in time delays. This somewhat novel approach allows an estimate of not only the delay time between shots, but also the *number* of shots of the explosion.

2.1.2 Deterioration Of Modulation Function With Scatter in Delay Times

The standard model for the source function of a ripple-fired explosion, $x(t)$, consisting of N equal explosions delayed by the interval, τ , assumes that it can be written as:

$$x(t) = \sum_{k=0}^{N-1} s(t-k\tau).$$

EXPLOSION CHARGES AND ML

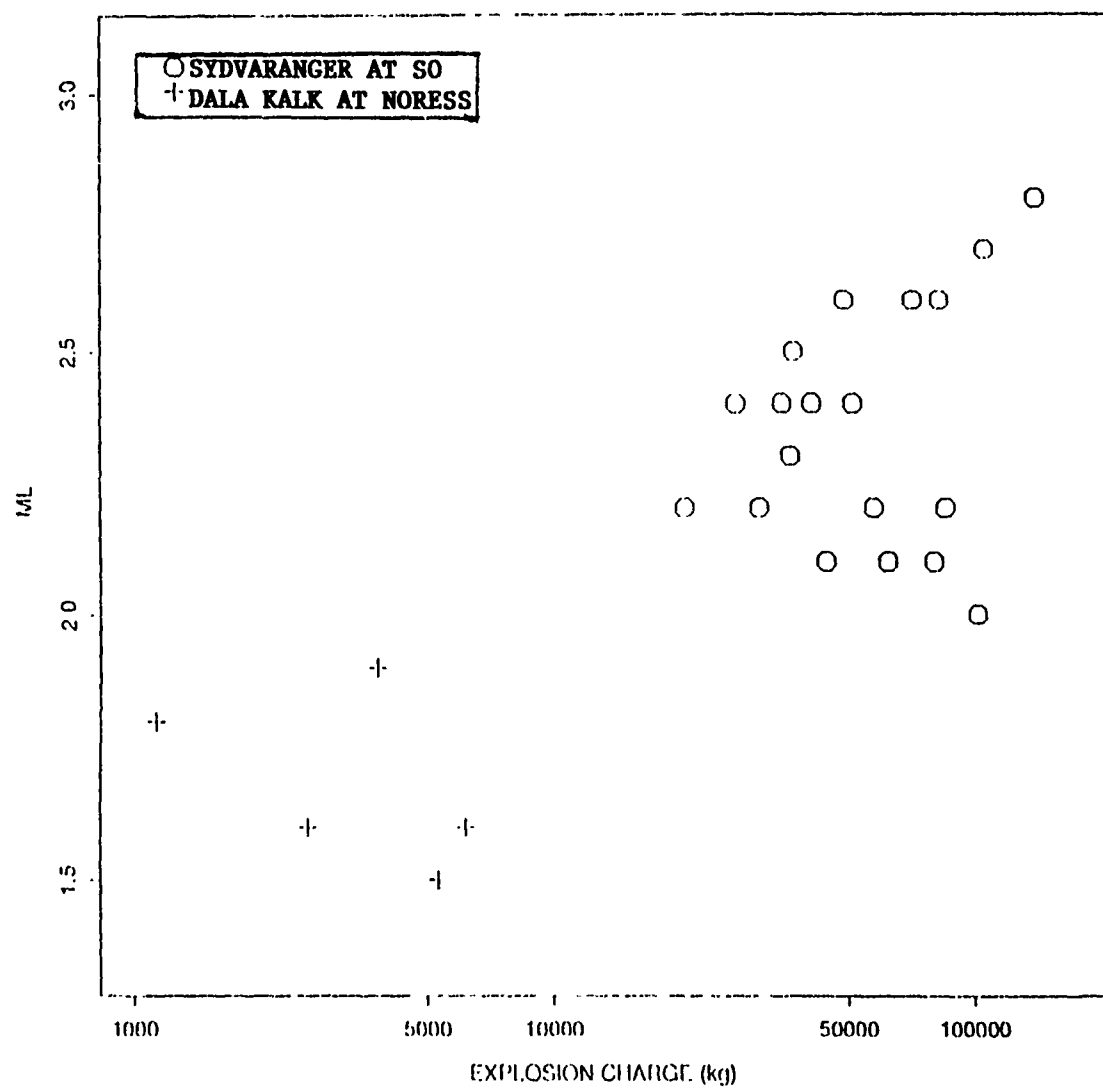


Figure 1. Local magnitudes, M_L , plotted against charges of ripple-fired explosions for two paths in Fennoscandia. Information on explosions have been obtained from a database compiled by Dahle *et al.* (1989). Crosses represent M_L in the NORESS bulletin from dynamex explosions in the Dala Kalk open pit (limestone). Open circles are for M_L at the station SO of the Finnish Station Network from slurry explosions in the Sydvaranger open pit mine (iron ore). The nominal charges of slurry explosions have been multiplied by a grade factor of 0.9.

Here $s(t)$ is the source function for each individual explosion. By applying the Fourier transform to the source function for the total ripple-fired explosion, the source function for an individual explosion and a modulation function are separated:

$$X(j\omega) = S(j\omega) \cdot M(j\omega).$$

The Fourier transform of the modulation function, $M(j\omega)$, can in turn be represented as:

$$M(j\omega) = \sum_{k=0}^{N-1} \exp(-j\omega k \tau).$$

If we assume that there is a scatter in the delay time, τ_k , for shot k , we can write: $\tau_k = k \cdot \tau + \epsilon_k$, where the error term ϵ_k is assumed to be normally distributed with zero mean and standard deviation σ_k . The detonators of a ripple-fired explosion go off independently and ϵ_k are therefore independent (Fauske, 1990). Moreover, it is reasonable to assume that the standard deviation increases linearly with shot number (Fauske, 1990 and Stump and Reamer, 1990), e.g., $\sigma_k = \sigma_0 + k \cdot \sigma_1$. The average value (expectation operator) of each exponential term in the sum that makes up the Fourier transform of the modulation function, $M(j\omega)$ is:

$$\mathbb{E}[\exp(-j\omega(k\tau + \epsilon_k))] = \exp(-j\omega\tau k - \frac{1}{2}\omega^2(\sigma_0 + k\sigma_1)^2).$$

It is not obvious how to reduce the expression for the average of the power spectrum of the modulation function into a simple analytical form because k , the shot number, is quadratic. However, the average of the power spectrum of the modulation function, $M(j\omega) \cdot M^*(j\omega)$, can be written in a simple closed form if $\sigma_1 = 0$ (Israelson, 1990).

Data on Scatter in Delays

Estimates of the standard deviation, σ_k , as a function of shot number have been given for some detonators used on the Norwegian market by Fauske (1990). Examples of these estimates are shown in *Figure 2*, where the standard deviation is plotted as a function of percent of the delay time, τ , for millisecond ($\tau = 25$ ms) and quarter second ($\tau = 250$ ms) detonators. For example, this means that for the 25 ms delay times the standard deviation increases from about 2 to 6 ms for shot numbers $k=1$ and $k=20$, respectively.

These detonators are used for no more than 25 intervals, i.e., $k \leq 25$, and the standard deviations are clearly within the requirement, $\sigma_k < \tau/3$, that such detonators are supposed to meet (Fauske, 1990). This requirement would avoid successive

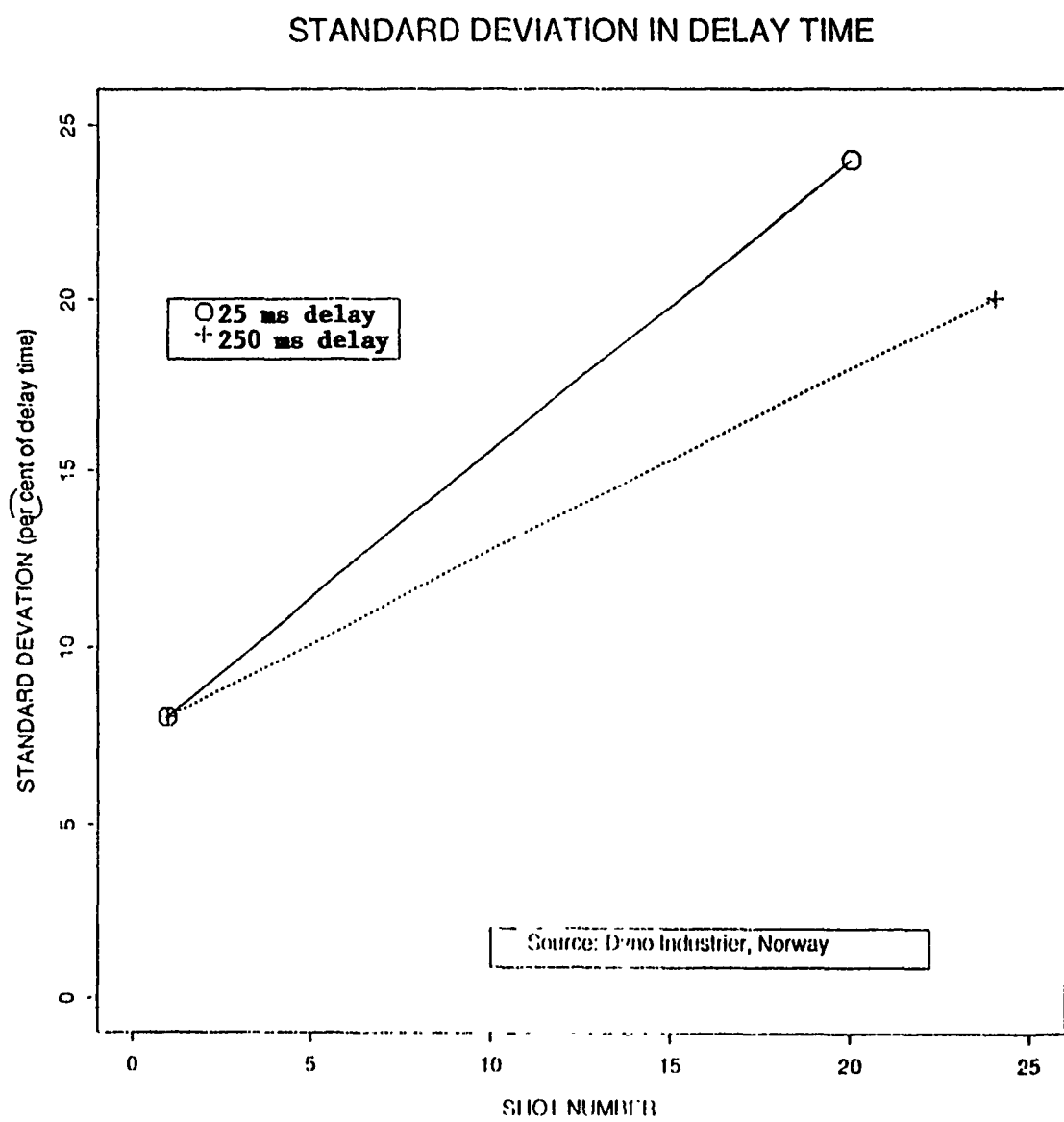


Figure 2. Standard deviation of time delay (in percent of delay between successive shots) as a function of shot number (after Fauske, 1990).

shots being fired almost simultaneously at a 1.5σ level (or $\approx 93\%$). For comparison, it can be noted that according to Hedlin *et al.* (1989), deviations between actual and intended delay times could be as high as 34% of the delay time between shots for some quarries in the Eastern U.S.

Examples of Modulation Functions

Dahle *et al.* (1989) have compiled a database with information on ripple-fired explosions in Fennoscandia including delay times between individual shots and their charges. *Figure 3* illustrates schematically the delays and charges for a ripple-fired explosion in this database (at Dala Kalk AB in Sweden, open pit near latitude 60.62N and longitude 15.1E). It consists of five shots with 25 ms delay time; the charges of the two first shots are about one third of the three last shots.

The modulation function for this rippled fired explosion, assuming no scatter in delay times, is drawn as a heavy line in *Figure 4* together with results from simulations assuming scatter with a standard deviation increasing linearly with shot number in accordance with the data in *Figure 2*. The average curve represents a mean of 1000 simulated modulation functions using a normal random number generator to add errors to the time delays of individually simulated modulation functions. The estimated average of the modulation curve shows a significantly reduced second peak around 80 Hz and a generally increased amplitude level at higher frequencies compared to the ideal case with no errors. More important, perhaps, is the large standard deviation of the average curve. This effect is more clearly demonstrated by the variation in the 10 simulated modulation functions in *Figure 5*. There is dramatic variation among the simulated modulation functions which also differ significantly from the theoretical modulation function having no scatter in the delay times (heavy line in *Figure 4*).

The curves in *Figure 5* clearly illustrate that significant scatter in the delay times may also hamper the identification of ripple-fired explosions using methods based on the detection of a spectral modulation pattern.

2.1.3 Number of Explosions From Autocorrelation of Modulation Function

Most methods to identify ripple-fired explosions that have recently been suggested attempt to detect modulation or scalloping of the frequency spectrum of one or more recorded phases (Baumgardt, 1988). As mentioned earlier, spectral scalloping can be directly related to the *time delay* between successive shots of the ripple-fire, but does not provide direct information on the *number* of shots. Here we discuss the possibility of estimating both delay time and number of shots.

Distribution of Charges

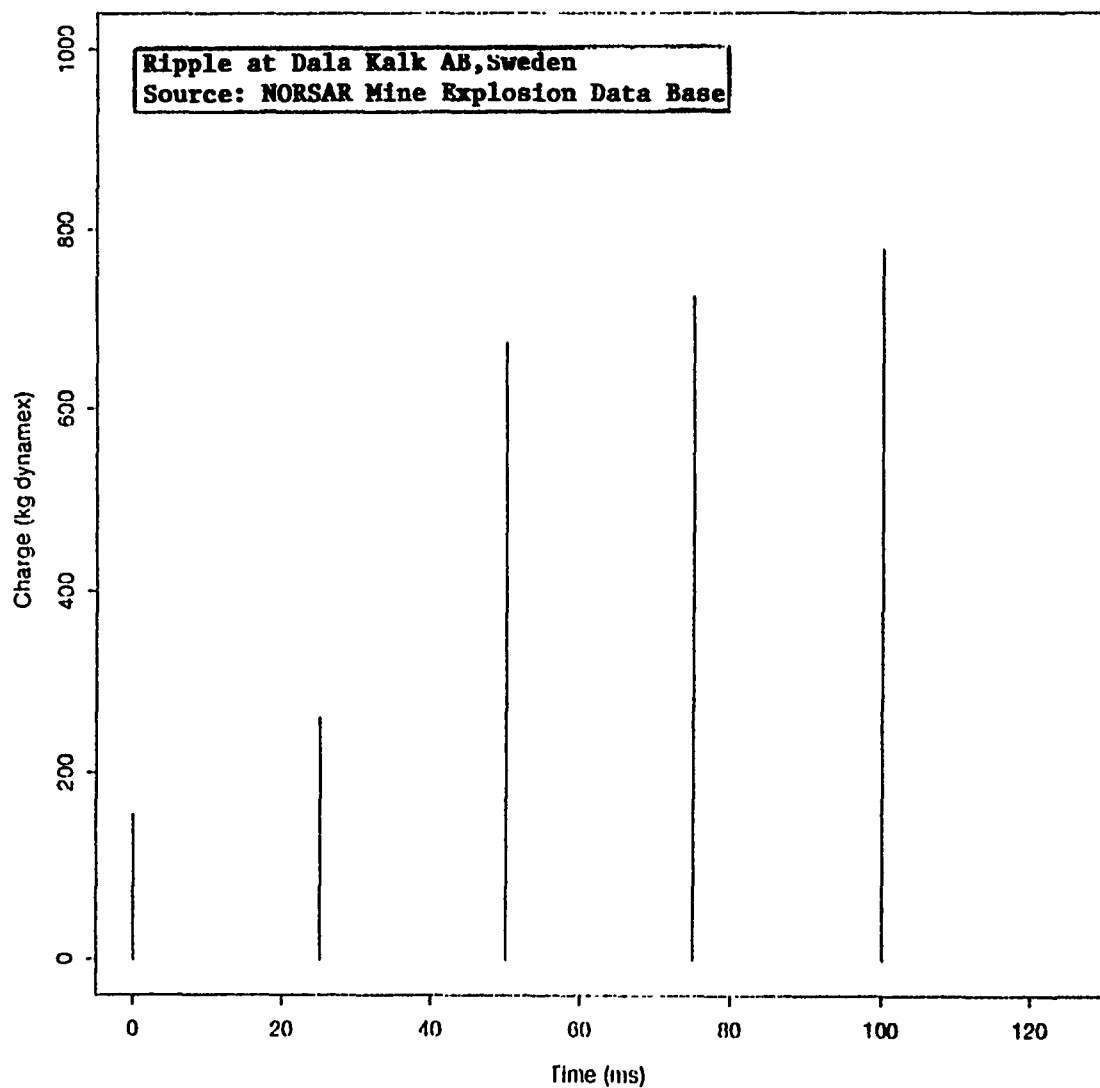


Figure 3. Time delays and charges of a ripple-fired explosion at Dala Kalk consisting of five individual blasts (from Dahle *et al.*, 1989).

MODULATION FUNCTIONS

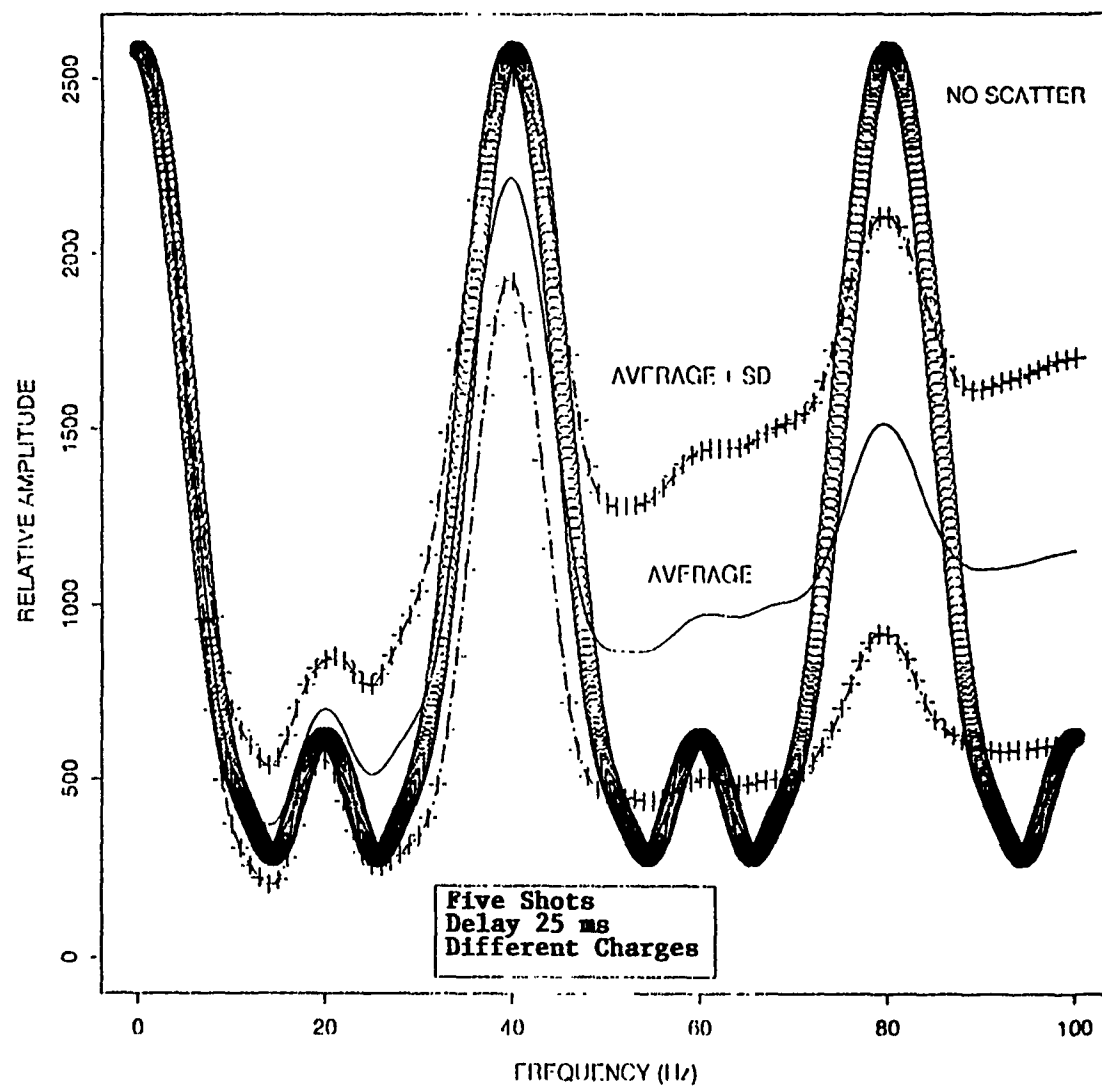


Figure 4. Modulation functions for ripple-fired explosion defined in *Figure 3*. The heavy line (circles) represents no errors in delay times. The average curve (thin line) and associated ones with \pm one standard deviations (crosses) are for errors in time delays with standard deviations according to *Figure 2*.

SIMULATED MODULATION FUNCTIONS

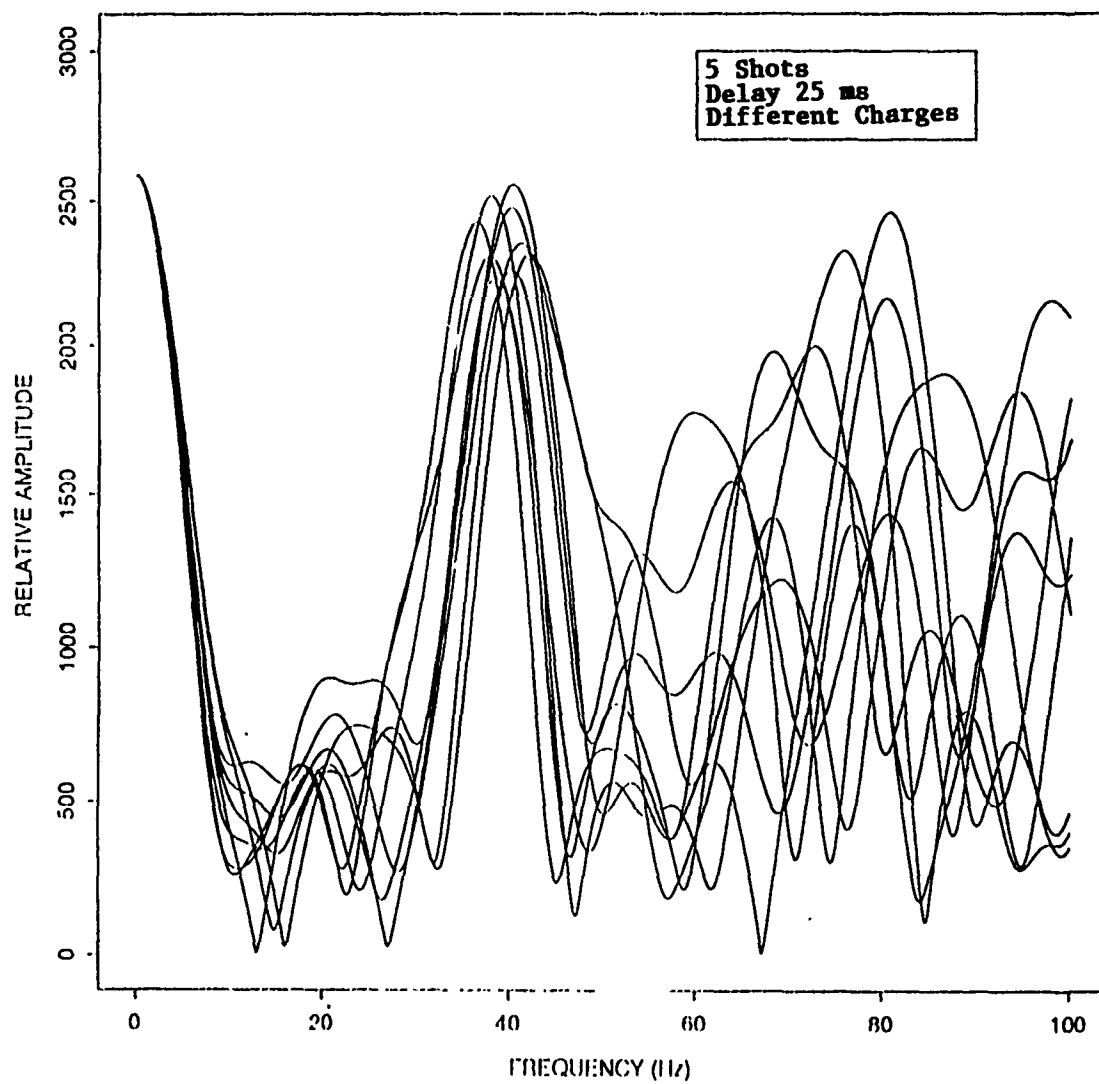


Figure 5. Examples of modulation functions for the ripple-fired explosion defined in Figure 3, assuming errors in scatter of delay times according to Figure 2. The nine curves were simulated using random number generators to assign values to time delays.

As shown above, the Fourier transform of the modulation function of a ripple-fired explosion can be represented as:

$$M(j\omega) = \sum_{k=0}^{N-1} \exp(-j\omega k\tau).$$

We assume no or negligible errors in the delay times. The inverse Fourier transform of the power spectrum of the modulation function which is equal to the autocorrelation, can be written in the form:

$$(M(j\omega) \cdot M^*(j\omega))^{-1} = \sum_{k=0}^{N-1} (N-k) \cdot \delta(t-k\tau).$$

This is a series of spikes delayed by τ s and with decreasing amplitude from N to 1.

We may assume that the recording, $r(t)$, --of a phase or the entire wave train-- for a ripple-fired explosion is the modulation function, $m(t)$, convolved with another term:

$$r(t) = m(t) * v(t).$$

The term $v(t)$ takes into account the source function of individual shots, path effects, and instrument response by convolution.

We use a heavily smoothed power spectrum of the recorded signal, $r(t)$, as an estimate of the power spectrum for the term $v(t)$. The smoothing is obtained by a standard running average technique. This means that:

$$\hat{M}(j\omega) \cdot \hat{M}^*(j\omega) = \frac{R(j\omega) \cdot R^*(j\omega)}{R_{smooth}(j\omega) \cdot R_{smooth}^*(j\omega)}$$

is an estimate (indicated with a hat) of the power spectrum of the modulation function. By taking the inverse Fourier transform of this ratio, we get an estimate of the autocorrelation of the modulation function, which should ideally consist of a series of spikes, delayed by τ and with linearly decreasing amplitudes.

Test on Synthetic Data

Figure 6 shows an estimate of the autocorrelation of the modulation function for a synthetic example. The recording at the NRDC station KKL of a single chemical explosion (top trace) has been used to generate a signal consisting of five explosions with delay time 124 ms by just delaying and adding five copies of the recording for the single explosion (middle trace). This synthetically generated "ripple-fired" explosion trace has a somewhat larger P coda than the recording for the single explosion. The autocorrelation for the modulation function at the bottom trace

SYNTHETIC EXAMPLE

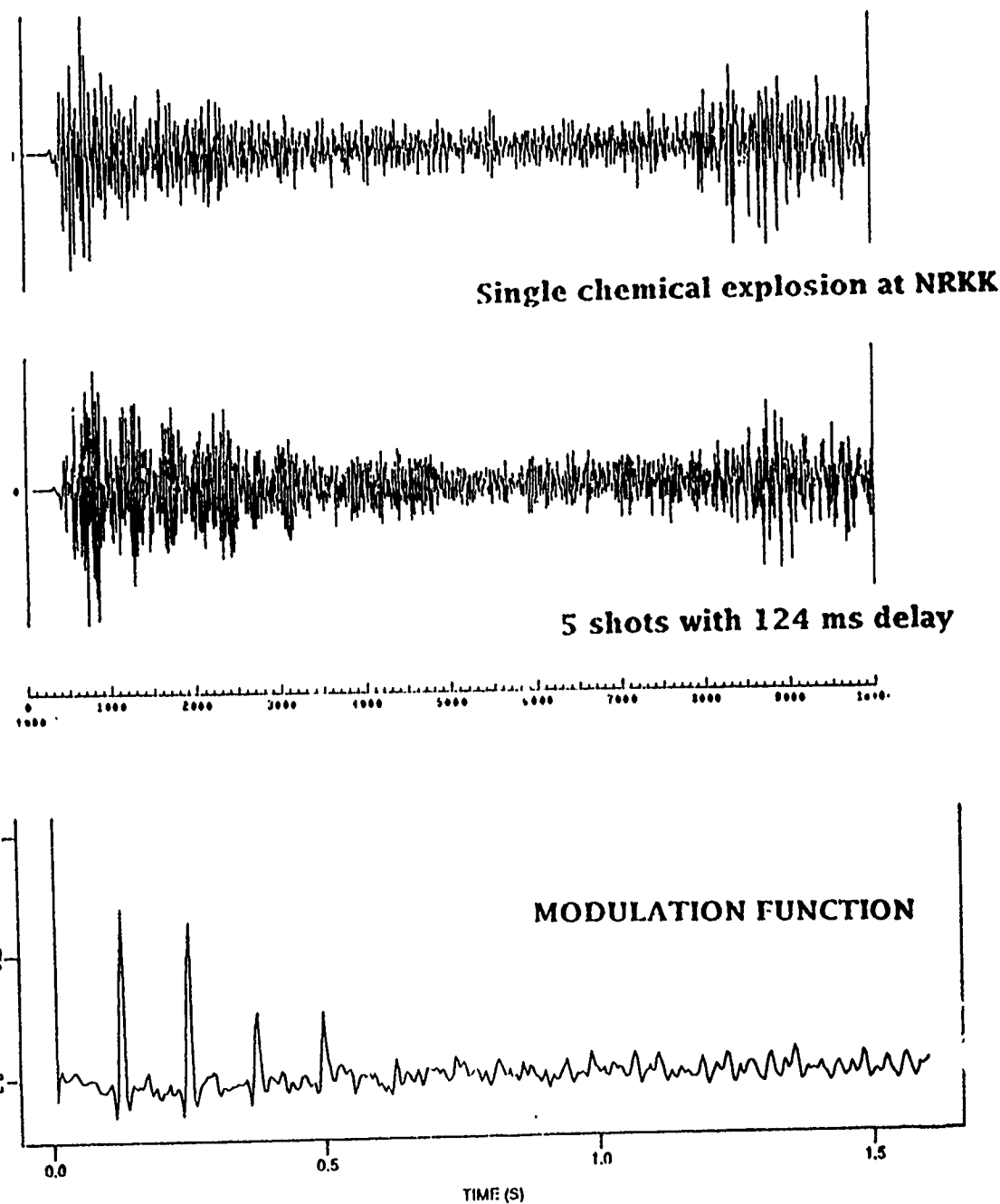


Figure 6. Synthetic example illustrating the computation of the autocorrelation function for the modulation function. The upper trace is a recording for a single chemical explosion in E. Kazakhstan at the NRDC station NRKK in Karkaralinsk. The middle trace was obtained by adding five copies of the top trace and successively delayed 124 ms; the sampling rate of the data is 250 Hz. The bottom trace is the estimated autocorrelation of the modulation function showing four clear spikes, with delays of about 124 ms, after the initial large amplitude.

shows four clear spikes after the zero-delayed initial large spike. Experiments using this recording of the single chemical explosion with different delays and numbers of explosions gave similar results.

Examples with real data

The autocorrelation for the modulation function estimated for two presumed ripple-fired explosions, one recorded at the NRDC station NRKK in Karkaralinsk and the other at the high frequency element of the NORISS array, are shown in *Figure 7*. In both cases, clear trains of spike-like pulses following the initial large amplitude (at zero delay) can be seen. The number of spikes and estimated delay times are indicated in the figure. At this point in time, however, no independent information is available on the characteristics of these presumed ripple-fired explosions to verify the estimates on delay times and number of shots.

2.1.4 Acknowledgements

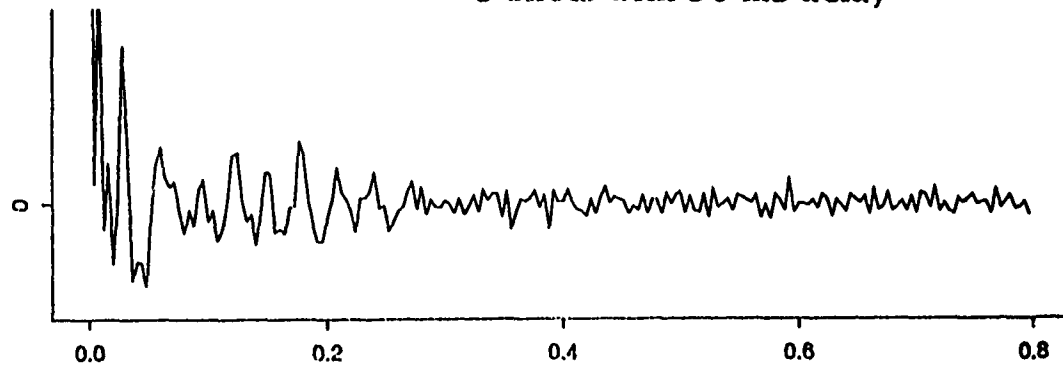
I would like to thank Dr. Anders Dahle at NORSAR and Dr. Arve Fauske at Dyno Industrier As in Saetre, Norway, for providing information on mining explosions and explosion detonators.

Hans Israelsson

MODULATION FUNCTIONS

87175 10:35:00.2 49.3N 72.7E at NRKK

9 shots with 30 ms delay



Explosion Blaasjoen, Norway at NRAO

6 shots with 65 ms delay

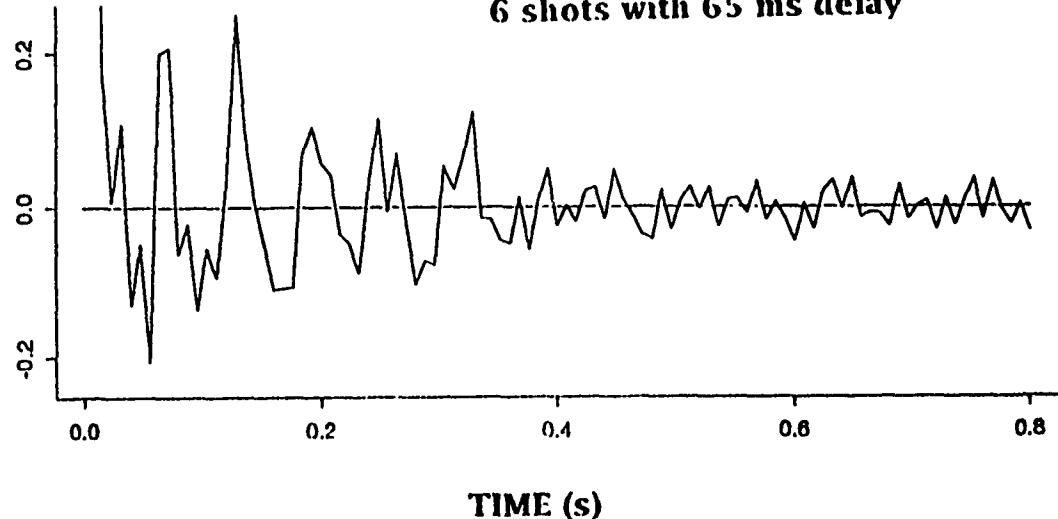


Figure 7. Estimated autocorrelations of the modulation function for two presumed ripple-fired explosions. The top trace is for recordings at the NRDC station NRKK at Karkaralinsk and the bottom is for recordings at the high frequency element of the NORESS array. The number of spikes and their successive delay, indicated in the figure, are used to estimate the number of shots and time intervals between shots.

References

- Baumgardt, D. R. and K. A. Ziegler (1988). Spectral Evidence for Source Multiplicity in Explosions: Application to regional discrimination of earthquakes and explosions, *Bull. Seism. Soc. Am.* Vol. 78, pp. 1773-1795.
- Dahle, A., A. Alsaker, and S. Mykkeltveit (1989) Establishment of a mining explosion data base. Semiannu. Tech. Summ., 1 April - 30 September 1989, Rep. No. 1-89/90, Kjeller, Norway.
- Fauske, A. (1988), Modern detonators used in ripple-firing (in Norwegian), Dyno Industrier AS
- Jan Fyen (1987). NORESS noise spectral studies - Noise level characteristics, *Semi-annual Technical Summary 1 October 1986 - 31 March 1987*, pp 46-58.
- Hedlin, M. A. H., Minster, J. B., and Orcutt, J.A. (1989) The Time Frequency Characteristics of Quarry Blasts and Calibration Explosions Recorded in Kazakhstan U.S.S.R. *Geophysical Journal* Vol. 99, pp. 109-122.
- Kim, W.Y., D.W. Simpson, and P.G. Richards (1990), Characteristics of high frequency spectra of regional phases from earthquakes and chemical explosions. In Proceedings of the Twelfth Annual DARPA/GL Seismic Research Symposium. (Eds J. Lewkowics and J McPhetres), GL-TR-90-0212 Geophysics Laboratory, Hanscom AFB, MA ADA226635
- Richards, P.G., D.W. Simpson, D.A. Anderson, and R. Such (1990), Survey of Blasting Activity in the U.S.; and observations from the New York State Network of Chemical Explosions in Northeastern America. In Proceedings of the Twelfth Annual DARPA/GL Seismic Research Symposium. (Eds J. Lewkowics and J McPhetres), GL-TR-90-0212 Geophysics Laboratory, Hanscom AFB, MA ADA226635
- Smith, A. T. (1988). High frequency seismic observations and models of chemical explosions: implications for the discrimination of ripple-fired mining blasts. *Bull. Seism. Soc. Am.* Vol. 79, pp. 1089-1110.

3.1 SLOWNESS ESTIMATION WITH INTERPOLATED NORESS DATA

ABSTRACT

In this note we explore the potential of using the NORESS mini-array to locate large teleseismic events with data resampled to very high frequencies (1 kHz). P-wave recordings from 15 explosions at the Balapan test site in E. Kazakh between 1984 and 1988 were analyzed. Time delays between array elements of the initial P-waves are determined to the nearest ms by interpolation of waveform data and cross correlation. The time delay patterns for closely spaced events show high repeatability and correlate to some degree with element elevation. The smallest standard deviations in azimuth and slowness estimated from the time delays (0.26 ° and 0.7 ms/degree respectively) are obtained only if the data from the outer ring are used. The standard deviations for azimuth and slowness from $f-k$ analysis of the same data were 1.45 ° and 1.9 ms/km, respectively. The average P-wave velocity below the NORESS array is estimated to be $6.1 \text{ km} \pm 0.7 \text{ km}$ by fitting time delays to a three-dimensional plane wavefront. Time residuals for the array elements from the estimated plane range between $\pm 10 \text{ ms}$. These residuals can be used to define the shape of the wavefront of the initial P-wave. They outline a smooth surface that deviates from a plane by about two percent over one wavelength. The shape of this smooth surface is highly repeatable for all Balapan events, but the surfaces for events in the southwestern and northeastern portions of the test site appear to be tilted about 2 ° relative to one another, which is about four times the theoretical value.

3.1.1 Introduction

In this note we explore the potential of the NORESS mini-array for epicenter locations of large teleseismic events using data resampled to very high frequencies (1 kHz). The scatter in azimuth and slowness estimates of large underground nuclear explosions at the E. Kazakh testing grounds are studied using precise determinations of time delays between array elements. This approach makes it possible to relate possible errors in azimuth and slowness estimates to anomalies at individual array elements.

3.1.2 Data

Table 1 lists source parameters, reported by the ISC, of the explosions in E. Kazakh for which recordings at NORESS were analyzed. The epicentral distance between the E. Kazakh testing grounds and NORESS is about 38 °. The events were all located in the Balapan area and had magnitudes in the range $m_b(\text{ISC})=5.5-6.2$.

TABLE 1

EVENT SOURCE PARAMETERS (ISC)					
	Date	Time	Lat(N)	Long(E)	mb
1984	Oct 27	1:50:10.6	49.95	78.83	6.2
1984	Dec 2	3:19:06.3	49.95	79.03	5.9
1984	Dec 16	3:55:05.1	49.88	78.82	6.1
1984	Dec 28	3:50:10.7	49.86	78.75	6.0
1985	Feb 10	3:27:07.6	49.88	78.82	5.9
1985	Apr 25	0:57:06.5	49.88	78.69	5.9
1985	Jun 15	0:57:00.7	49.85	78.87	6.1
1985	Jun 30	2:39:02.7	49.84	78.69	6.0
1985	Jul 20	0:53:14.5	49.95	78.83	6.0
1987*	Mar 12	1:57:17.0	49.90	78.83	5.5
1987*	Apr 17	1:03:08.2	49.84	78.67	6.0
1987	Aug 2	0:58:06.8	49.88	78.92	5.9
1987	Nov 15	3:31:06.7	49.84	78.77	6.1
1988	Nov 12	3:30:03.7	50.08	78.99	6.0
1988	Dec 17	4:18:06.9	49.89	78.93	6.0

Data for events marked with * were found to be spurious and were not used in the analysis.

The relative locations of the events are shown in *Figure 1*. There are 13 events southwest of the fault marked on the map, and 2 events to the northeast. Observations of P-waveforms at the UK arrays (Marshall *et al.*, 1985), of P-wave amplitudes and I.g measurements at NORESS (Ringdal and Hokland, 1987), and of I.g measurements at Grafenberg (Ringdal and Syen, 1988) suggest that these two areas are characterized by different geophysical properties.

Waveform data recorded for the events were retrieved from the databases at the Center for Seismic Studies. Only data recorded at the short period *vertical* components (in all 25) were used. The coordinates (x_i, y_i, z_i) of the elements of the NORESS array relative to the center element NRA0 are listed in Table 2. The data were originally sampled at 25 ms intervals, which corresponds to about 10 percent of the time it takes a plane P wavefront from an E. Kazakh event to cross the NORESS array.

Typical unfiltered traces of P-wave signals are shown in *Figure 2*. All signals are of short duration and have a very high signal-to-noise ratio. Their amplitude spectra are also sharply peaked around 2 Hz. Because of these characteristics the signal processing for this study was based on unfiltered records.

3.1.3 Estimation of Time Delays

Data windows were chosen manually for each signal. The beginning of the window was about 0.15 s prior to the pick of the P-onset at the center element of the array (NRA0), and the end of the window was set just after the first zero crossing of the first significant peaks. The lengths of the data windows varied between 1.6 - 2.7 s for the events, i.e., the number of data points, J , varied between 64 and 108.

High Frequency Interpolation

The time resolution of the originally recorded data (25 ms between successive samples) was improved by interpolation to 1 ms between samples. Standard cubic splines were used to interpolate the data. The value of $s(t)$ for a time t between sampled values $j \cdot \Delta t$ and $(j+1) \cdot \Delta t$ was obtained from:

$$s(t) = A \cdot s(j \cdot \Delta t) + B \cdot s((j+1) \cdot \Delta t) + C \cdot Y_j + D \cdot Y_{j+1}$$

with

$$A = (j+1) \cdot \Delta t - t / \Delta t$$

$$B = 1 - A$$

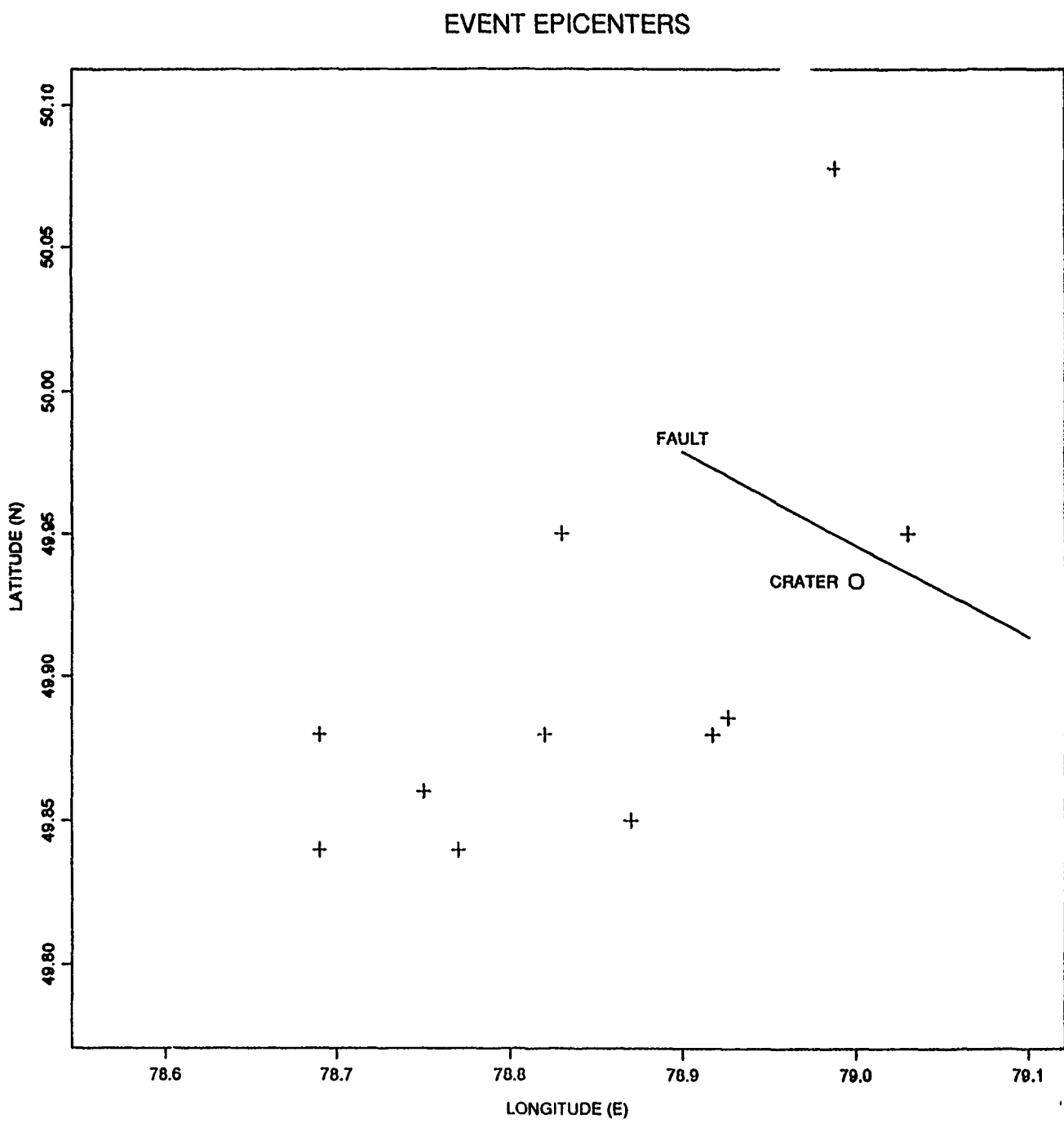


Figure 1. Epicenters of the events at the Balapan Test Site.

TABLE 2.

ARRAY CO-ORDINATES AND ELEMENT CORRECTIONS					
Station	Coordinates (km)			Correction(s)	
Code	x	y	z	Mean	Std
NRA0	0.000	0.000	0.000	-0.0002	0.0015
NRA1	0.045	0.142	-0.011	-0.0008	0.0006
NRA2	0.104	-0.108	0.009	0.0020	0.0016
NRA3	-0.146	-0.034	-0.006	-0.0034	0.0013
NRB1	0.066	0.318	-0.003	-0.0020	0.0004
NRB2	0.331	0.025	0.013	0.0072	0.0009
NRB3	0.139	-0.302	0.012	-0.0002	0.0017
NRB4	-0.233	-0.222	-0.003	-0.0065	0.0008
NRB5	-0.276	0.158	-0.013	-0.0041	0.0008
NRC1	0.106	0.683	-0.003	-0.0005	0.0017
NRC2	0.599	0.337	0.037	0.0092	0.0008
NRC3	0.643	-0.241	0.050	0.0165	0.0012
NRC4	0.204	-0.661	0.009	-0.0101	0.0014
NRC5	-0.400	-0.571	-0.003	-0.0143	0.0005
NRC6	-0.692	-0.053	0.001	-0.0079	0.0010
NRC7	-0.451	0.544	-0.027	-0.0087	0.0015
NRD1	0.189	1.477	0.003	0.0104	0.0013
NRD2	1.094	1.010	0.070	0.0188	0.0009
NRD3	1.489	0.072	0.151	0.0313	0.0032
NRD4	1.186	-0.905	0.077	0.0136	0.0009
NRD5	0.331	-1.454	0.046	-0.0177	0.0010
NRD6	-0.684	-1.331	0.050	-0.0183	0.0010
NRD7	-1.371	-0.568	0.035	-0.0106	0.0008
NRD8	-1.341	0.411	-0.001	-0.0008	0.0023
NRD9	-0.806	1.254	-0.024	-0.0030	0.0007

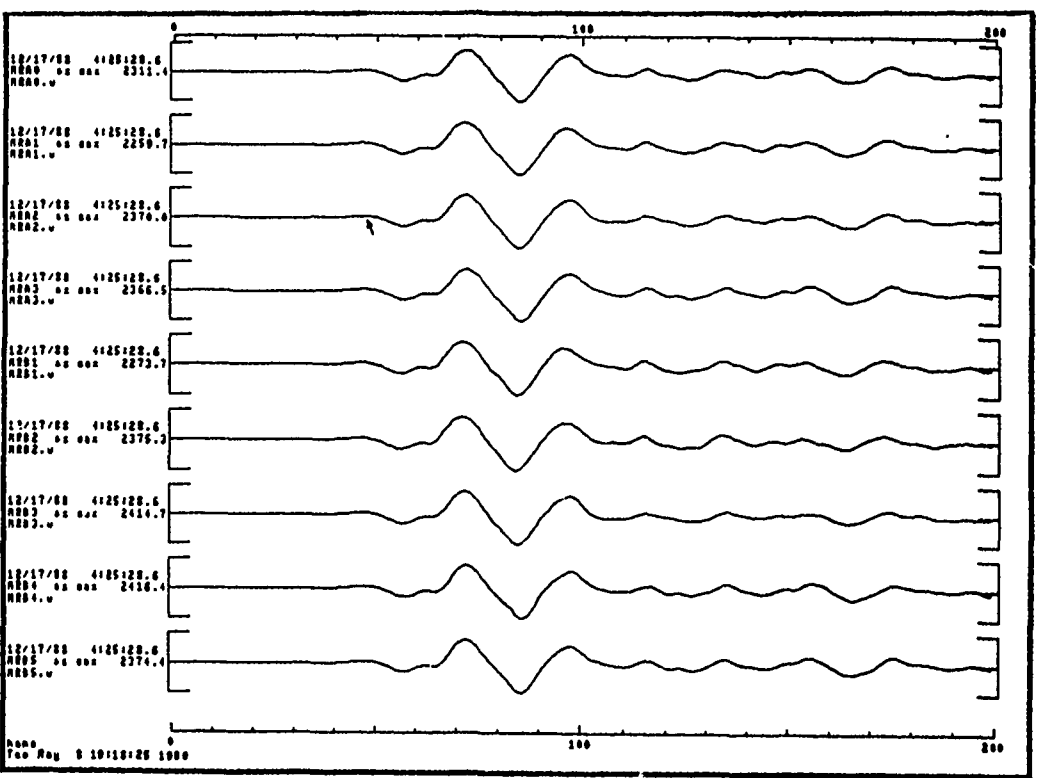
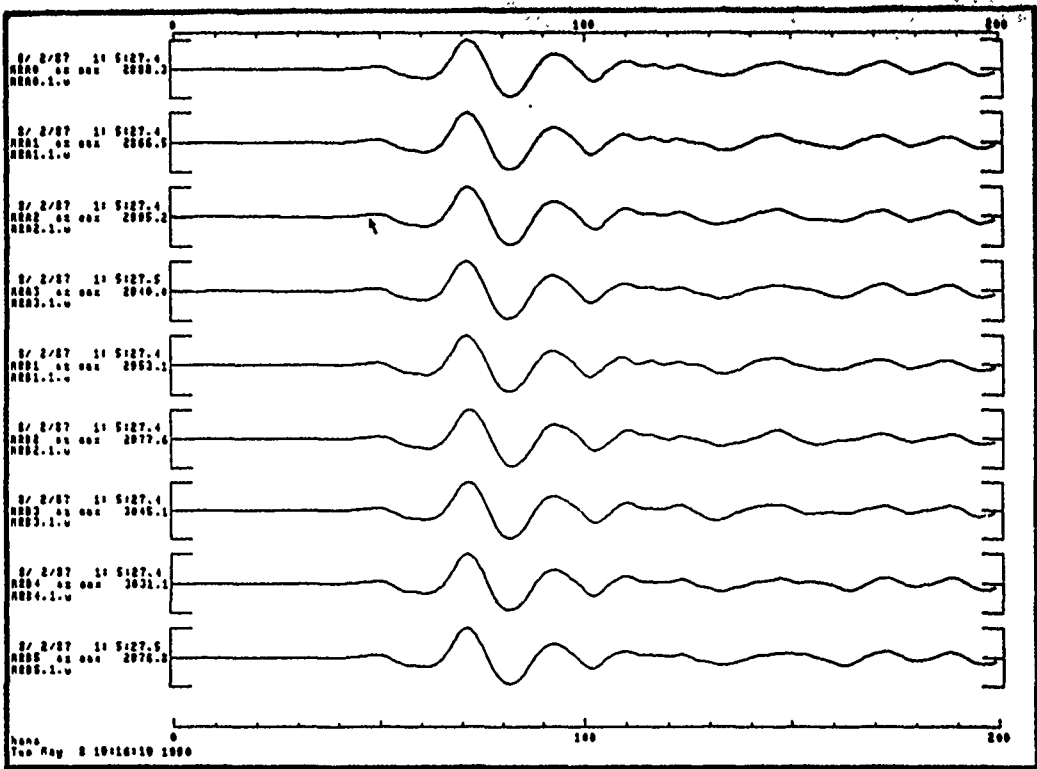


Figure 2. Examples of recorded P-waves at some of the elements at NORESS from events on Aug 2 1987 and Dec 17 1988.

$$C = \frac{1}{6} (A^3 - A) \cdot \Delta t^2$$

$$D = \frac{1}{6} (B^3 - B) \cdot \Delta t^2$$

and the "second derivatives", Y_j , derived from the equations:

$$\Delta t^2 / 6 (Y_{j-1} + 4Y_j + Y_{j+1}) = Y_{j+1} - 2Y_j + Y_{j-1} \quad j=2, \dots, J-1$$

Subroutines by Press *et al.* (1986) were employed for the computations. The values of Y_1 and Y_J were set to 0, giving the natural cubic spline, which has zero derivative on both end points. A five percent cosine taper was applied to the resampled data window. An example of interpolated values is given in *Figure 3*.

Waveform Correlation

For each event, k , we obtained time delays, τ_{ijk} , of the P-wave between array elements i and j from the cross correlation function, ρ_{ijk} , calculated for the interpolated and tapered data. The ρ_{ijk} was calculated in a straightforward manner using FFTs to increase computational speed.

The time delay, τ_{ijk} , is defined by the time-shift, u , that maximizes the cross correlation, i.e., $\rho_{ijk}(\tau_{ijk}) \geq \rho_{ijk}(u)$ for all u . This means that the time delays were determined to the nearest ms.

The maximum values of the cross correlation functions, i.e., $\rho_{ijk}(\tau_{ijk})$ are plotted in *Figure 4* against distance (see Table 2):

$$d_{ij} = \left((x_i - x_j)^2 + (y_i - y_j)^2 + (z_i - z_j)^2 \right)^{\frac{1}{2}}$$

There is large scatter in the data, but ρ_{ijk} is rarely < 0.95 .

Delays were calculated for all combinations of array element pairs, $i=1, \dots, n$ and $j=1, \dots, n$ for each event. (For events with data from 25 channels, i.e., $n=25$, the number of combinations is 300).

Figure 5 shows the traces aligned for two of the events using delays determined from this procedure.

3.1.4 Analysis of Time Delays

Since we were primarily interested in using the estimated time delays to make precise epicenter determinations, the τ_{ijk} were initially compared to those calculated from a theoretical model (P-tables of Jeffreys-Bullen). We therefore assumed that

INTERPOLATED SAMPLES

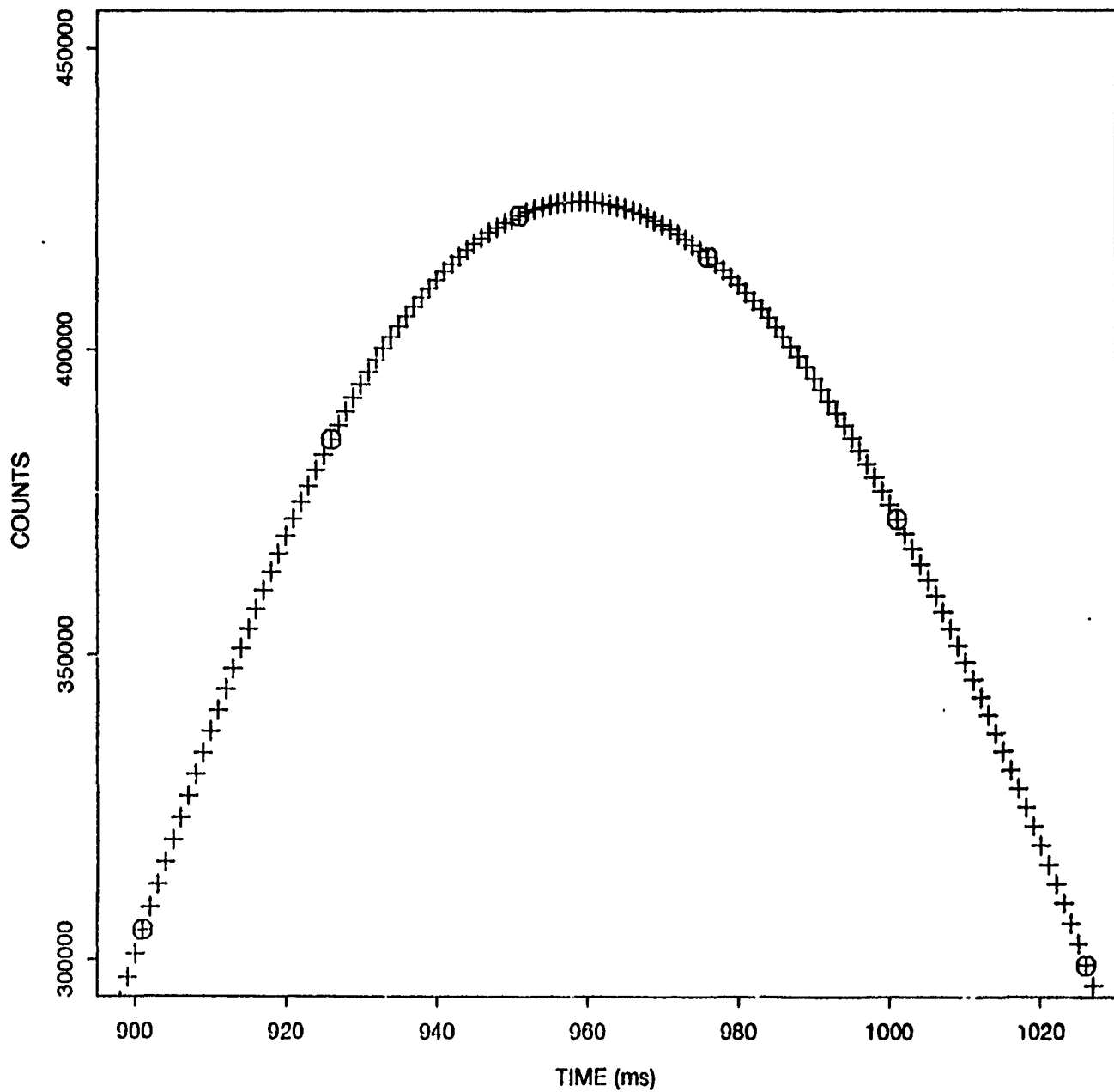


Figure 3. Example of interpolated data values. The original samples are indicated with open circles and the interpolated values with crosses. The data points cover 0.125 s.

MAXIMUM CORRELATION VALUES

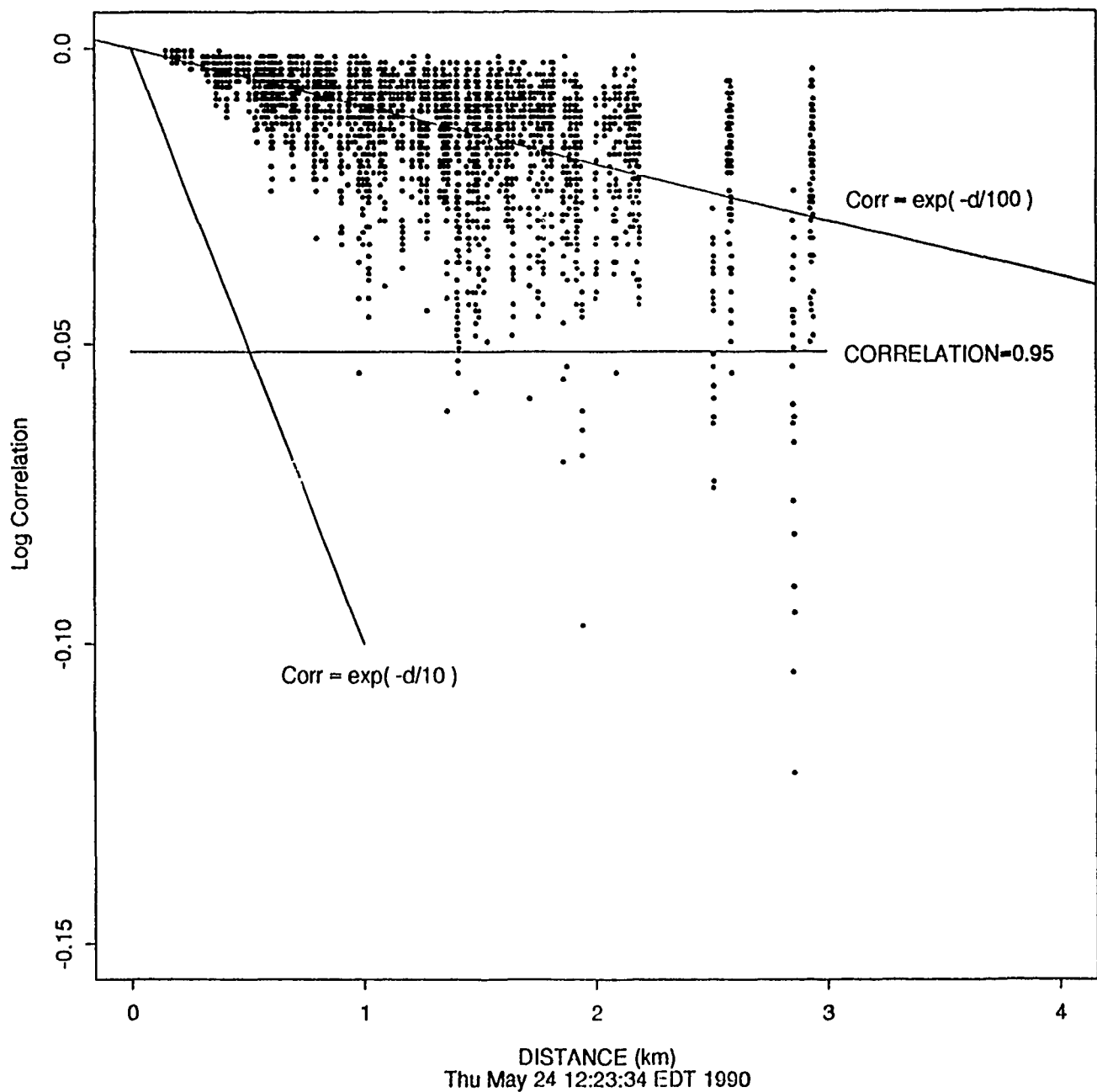


Figure 4. Maximum correlation values against distance, d , between element pairs for all events analyzed here. De-correlation curves, $\exp(-d/1000)$ from a linear regression, and $\exp(-d/10)$ (from Pg data, Mykkeltveit *et al.*, 1983) are drawn for comparison.

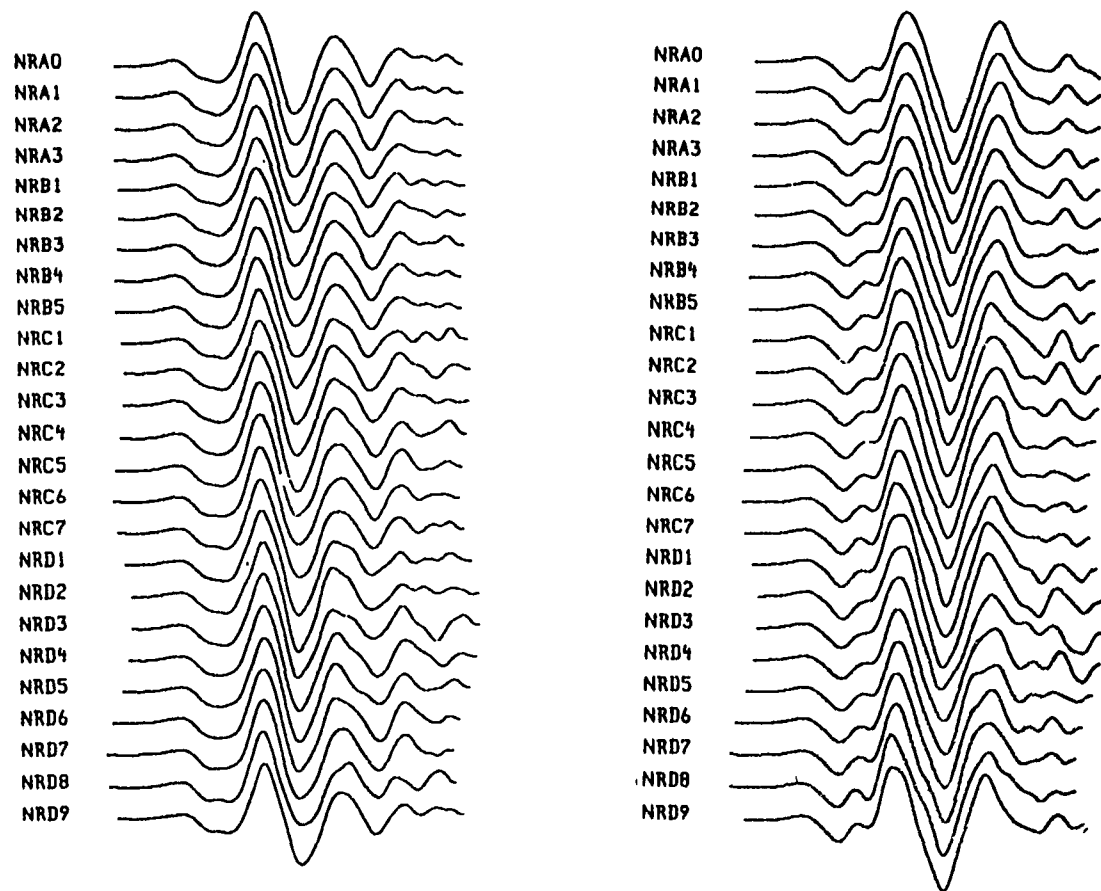


Figure 5. Traces aligned from time delays determined to the nearest ms, for events on Aug 2 1987 and Dec 17 1988.

the observed time delay, τ_{ijk} , between array elements i and j for event k could be written as:

$$\tau_{ijk} = \bar{r}_{ij} \cdot \bar{p}_k + c_{ik} - c_{jk} + \epsilon_{ijk}.$$

The theoretical horizontal slowness vector, \bar{p}_k , is given by:

$$\bar{p}_k = (p_k \cdot \sin(\phi_k), p_k \cdot \cos(\phi_k)),$$

where the scalar value of the slowness, p_k , was calculated from the travel time tables, and the back-azimuth, ϕ_k , was calculated relative to the center point, NRAO, of NORESS from the epicentral coordinates reported by ISC (see Table 1). The vector \bar{r}_{ij} is defined by the relative coordinates of the two array elements (see Table 2):

$$\bar{r}_{ij} = (x_i - x_j, y_i - y_j).$$

The terms c_{ik} for array element i ($i=1, 2, \dots, n$) are called *element corrections* and are analogous to station corrections of travel times for seismological station networks. The error terms ϵ_{ijk} were assumed to be Gaussian with zero mean and standard deviation σ_{0k} . We also assumed the ϵ_{ijk} to be independent.

Estimates of Element Corrections

For each event, k , one can estimate the element corrections c_i from a least squares fit to the equations (in all 301):

$$c_{ik} - c_{jk} = \tau_{ijk} - \bar{r}_{ij} \cdot \bar{p}_k \quad i=1, 2, \dots, 24; j=i, i+1, \dots, 25$$

$$\sum_{i=1}^n c_{ik} = 0$$

The average c_{ik} is given by:

$$\bar{c}_i = \frac{1}{K} \sum_{k=1}^K c_{ik}.$$

The \bar{c}_{ik} averaged over five of the events (i.e., $k=1, \dots, 5$) (all located in southwestern Balapan) for which data were available for all elements of the array and the associated standard deviations, $\sigma(c_i)$, are listed in Table 2. The estimated element corrections were quite consistent from one event to another. This is reflected by the small standard deviations: $\sigma(c_i) < 1$ ms for 14 of the 25 elements and $\sigma(c_i) < 2$ ms for all elements except NRD3 and NRD8.

The standard deviations of the errors ϵ_{ijk} were $\sigma_{0k} = 0.7$ ms, with virtually no variation among events, k . The contribution in standard deviation due to rounding error (1 ms) in the time delays is about 0.3 ms.

Erroneous Data

Data for the events on Mar 12 and Apr 17, 1987, were not used to obtain the average element corrections c_i . *Figure 6* shows the residuals ($c_{ik} - \bar{c}_i$) for these two events for array elements i . A clear offset in c_{ik} of 25 ms can be seen for several of the elements for the event on Mar 12 and for one element for the event on Apr 17. The source of these apparent sampling errors is not known, and the data for these two events are omitted in the subsequent analysis. The data for all events were processed with identical procedures. It seems, therefore, unlikely that the errors are due to software errors since sampling errors of this kind were detected only for 2 of the 15 events.

Effect of Elevation

The NORESS array is not perfectly horizontal. Elevations for the array elements available at the Center for Seismic Studies (cf. z-coordinates in Table 2) vary by 178 m. Assuming a velocity $\alpha=6.0$ km/s in the surface medium, this corresponds to a time delay of about 25 ms for a plane P wavefront from E. Kazakh. This in turn is about 10% of the time it takes a wavefront to cross the array horizontally. For more distant events the effect of varying surface elevation will be more pronounced.

Figure 7 shows the element corrections \bar{c}_i as a function of elevation, z_i . A line $c = z \cdot p_z$ with the vertical slowness $p_z = 0.183$ s/km ($p_z = (1/\alpha^2 - p^2)^{1/2}$) is drawn for comparison. There is some correlation in the data. The element NRD3 at the highest point of the array has the largest correction, 31 ms. The corrections for some other elements at high elevations are also significant. From the data in Table 2, it can be seen that the element NRD3 (at the highest point of the array) also has the largest standard deviation of its estimated element correction, $\sigma(c_i)$, among the elements (see Table 2).

Factors other than elevation clearly influence the element corrections, as indicated by the five outlying data points in *Figure 7*. In *Figure 8* the corrections are plotted as a function of relative horizontal location of the elements. A correction for delay due to elevation, $z_i \cdot p_z$ with the vertical slowness $p_z = 0.183$ s/km, has been applied to the c_i -values. Positive and negative corrections are separated by a line running in the northwest-southeast direction. There is no apparent correlation with the local surface geology, some features of which are also indicated in the figure.

Scatter in Azimuth and Slowness Estimates

We have looked at time delays among elements relative to values calculated from theoretical slowness and azimuth values. The reverse problem of estimating slowness and azimuth is of more practical interest. Such estimates can be obtained

87107

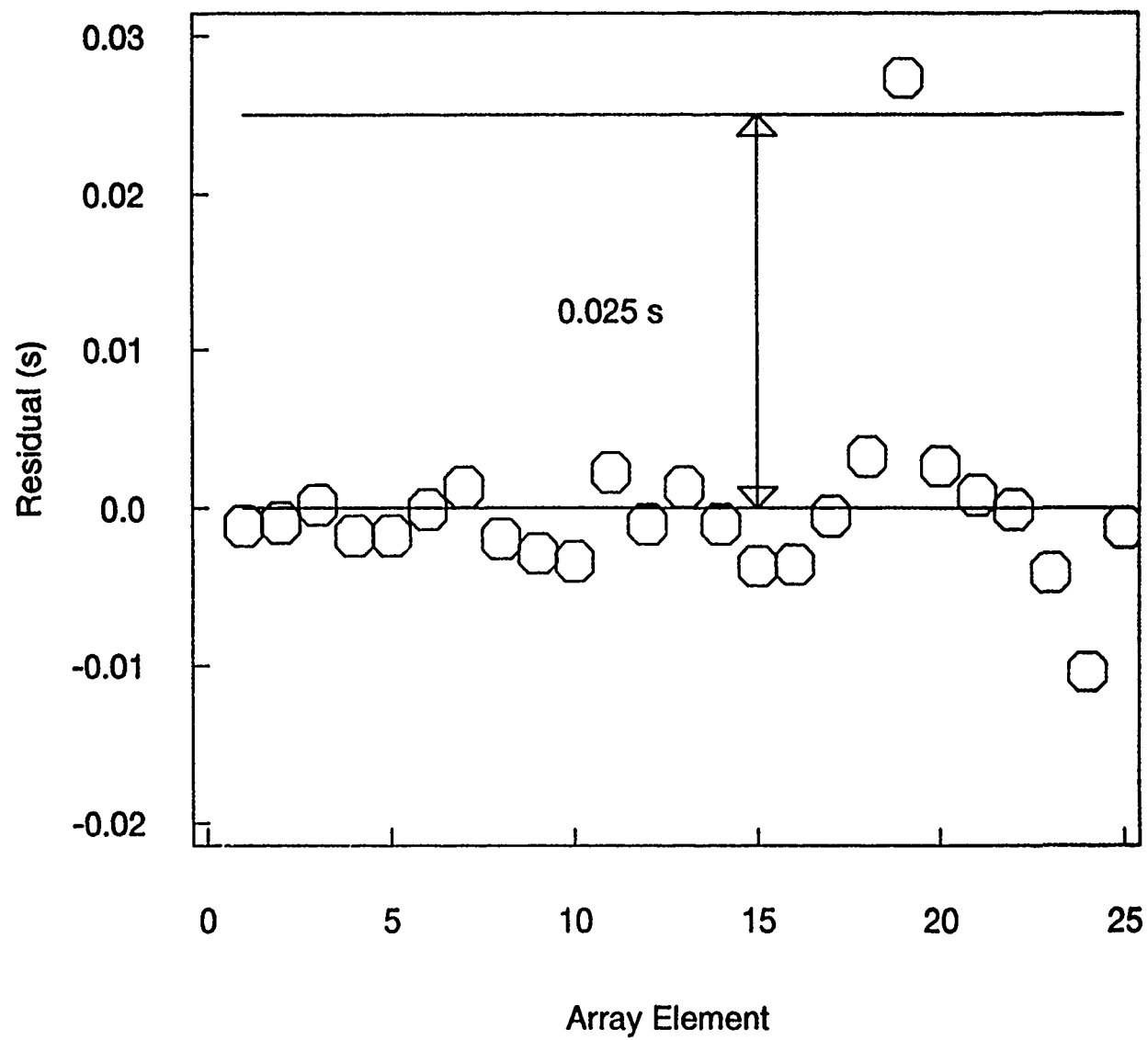
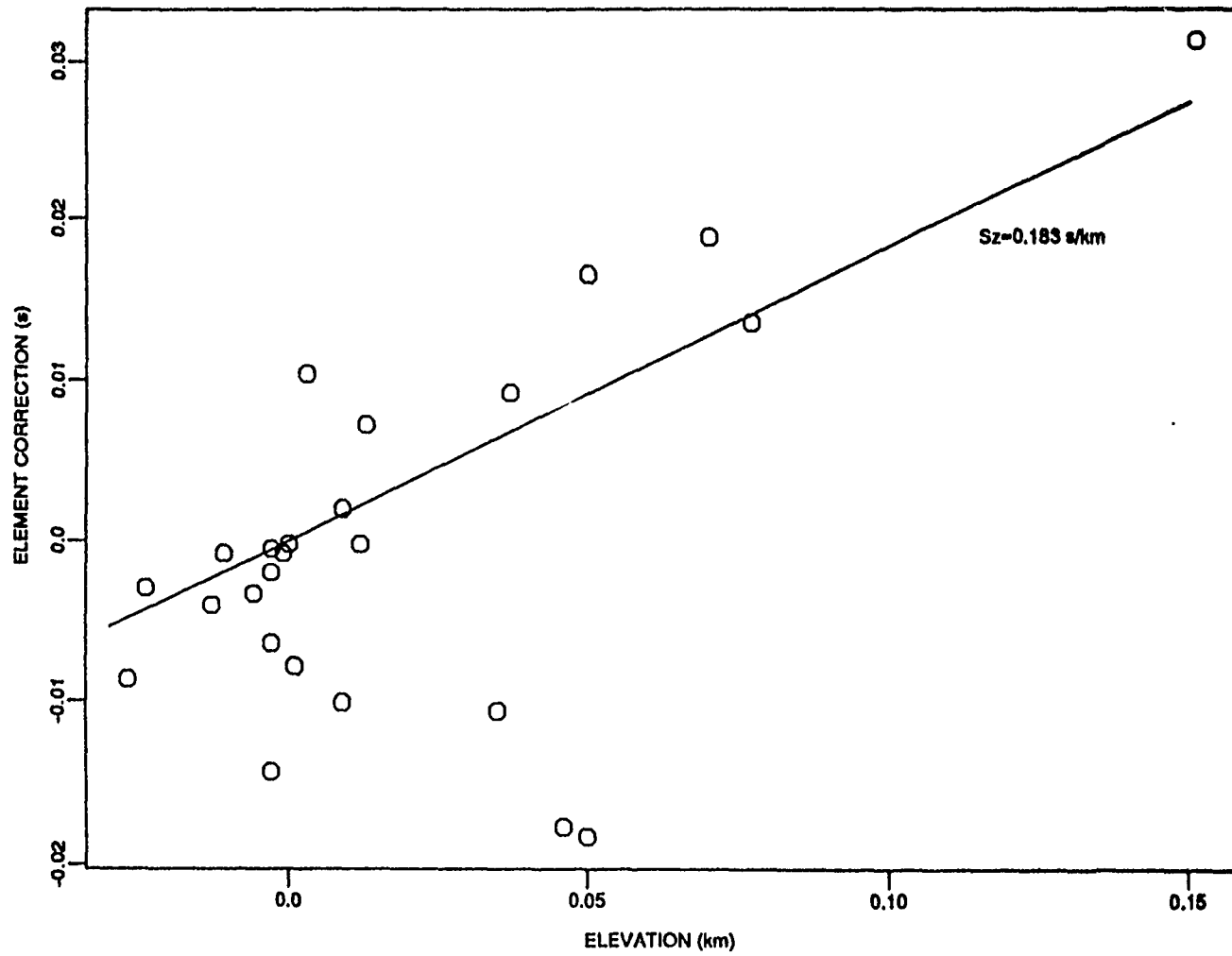


Figure 6. Difference between element corrections for events Mar 12 and Apr 17 1987 and average corrections for five events in southwestern Balapan. Notice the offset of 25 ms for some of the elements.



temp05

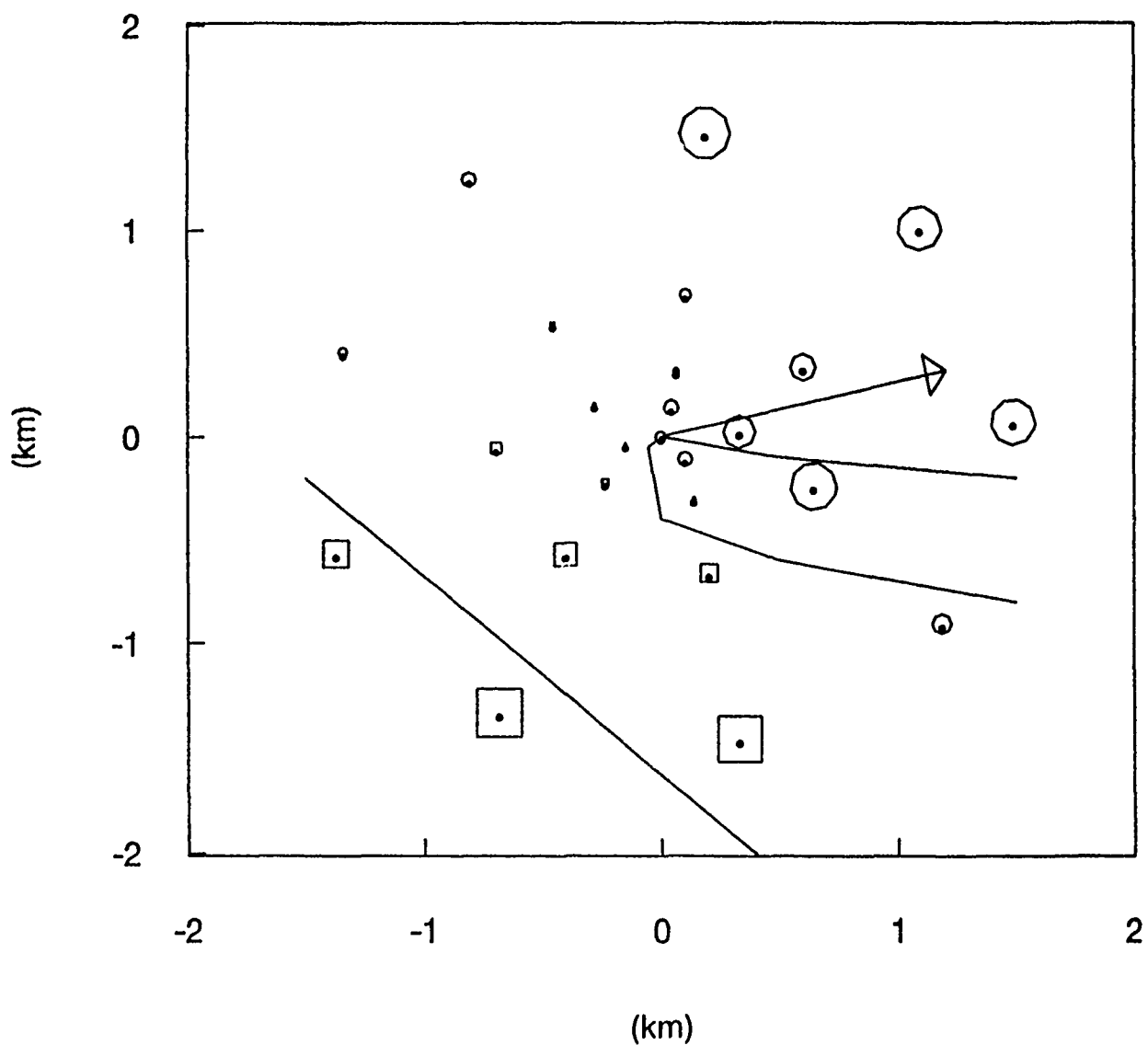


Figure 8. Average element corrections (with correction for elevation) as a function of horizontal element coordinates. Positive and negative corrections are indicated with circles and squares and imply "slow" and "fast" delays, respectively. The larger the symbol the larger its absolute value.

in a straightforward manner by fitting the time delays to those of a plane wave-front. Because of the significant values of the element corrections, c_i , such estimates will, in all likelihood, be biased. However, by subtracting the estimated element corrections \hat{c}_i from the observed time delays τ_{ijk} , unbiased estimates may be obtained. That is to say, we can estimate the components of the slowness vector, $\hat{p}_k = (p_{xk}, p_{yk})$ for event k from a least squares fit to the equations:

$$\hat{\tau}_{ijk} \cdot \hat{p}_k = \tau_{ijk} - (\hat{c}_i - \hat{c}_j) \quad i=1, \dots, n-1; j=1+1, \dots, n$$

Estimates of azimuth, $\hat{\phi}_k$, and slowness, \hat{p}_k , are obtained in the usual manner:

$$\hat{\phi}_k = \text{atan}(\hat{p}_{xk}/\hat{p}_{yk}),$$

$$\hat{p}_k = \left(\hat{p}'_{xk} + \hat{p}'_{yk} \right)^{1/2}.$$

Errors in azimuth and slowness are defined as the difference between estimated values and those calculated from the Jeffreys-Bullen travel time model and the coordinates reported by the ISC:

$$\Delta\phi_k = \hat{\phi}_k - \phi_k,$$

$$\Delta p_k = \hat{p}_k - p_k.$$

The quality of such unbiased estimates may then be described by standard deviations of the errors, $\sigma(\Delta\phi)$ and $\sigma(\Delta p)$, for the events. The element corrections estimated from data of five of the events in the southwestern part of the Balapan test site are applied to the time delays for all events. As the estimates of element corrections for NRD3 and NRD8 have large standard deviations, time delays involving those elements were omitted in the estimation.

We estimated the slowness and azimuth for each ring of the array separately. Estimates from, for example, the B-ring were thus based on time delays among the elements NRB1, NRB2, NRB3, NRB4, and NRB5. The 11 events in the southwestern part of Balapan were analyzed first. Figures 9 and 10 show the standard deviation of the azimuth and slowness errors, respectively, for the four rings. The standard deviation in azimuth is reduced from just below 2.0° for the A-ring to 0.26° for the D-ring. The standard deviation in the theoretical azimuth for these 11 events is 0.08°. The standard deviation in slowness is reduced in a similar way from approximately 0.004 s/km to 0.0007 s/km. The smallest standard deviation in slowness corresponds to a standard deviation in estimated epicentral distance of about 1.45°. It can be noted that the standard deviations for the entire array (except elements NRD3 and NRD8) are somewhat larger than those for the D-ring. This means that the best results for estimating slowness and azimuth of this group of events is obtained from relative time delays of 7 of the 25 elements of the array.

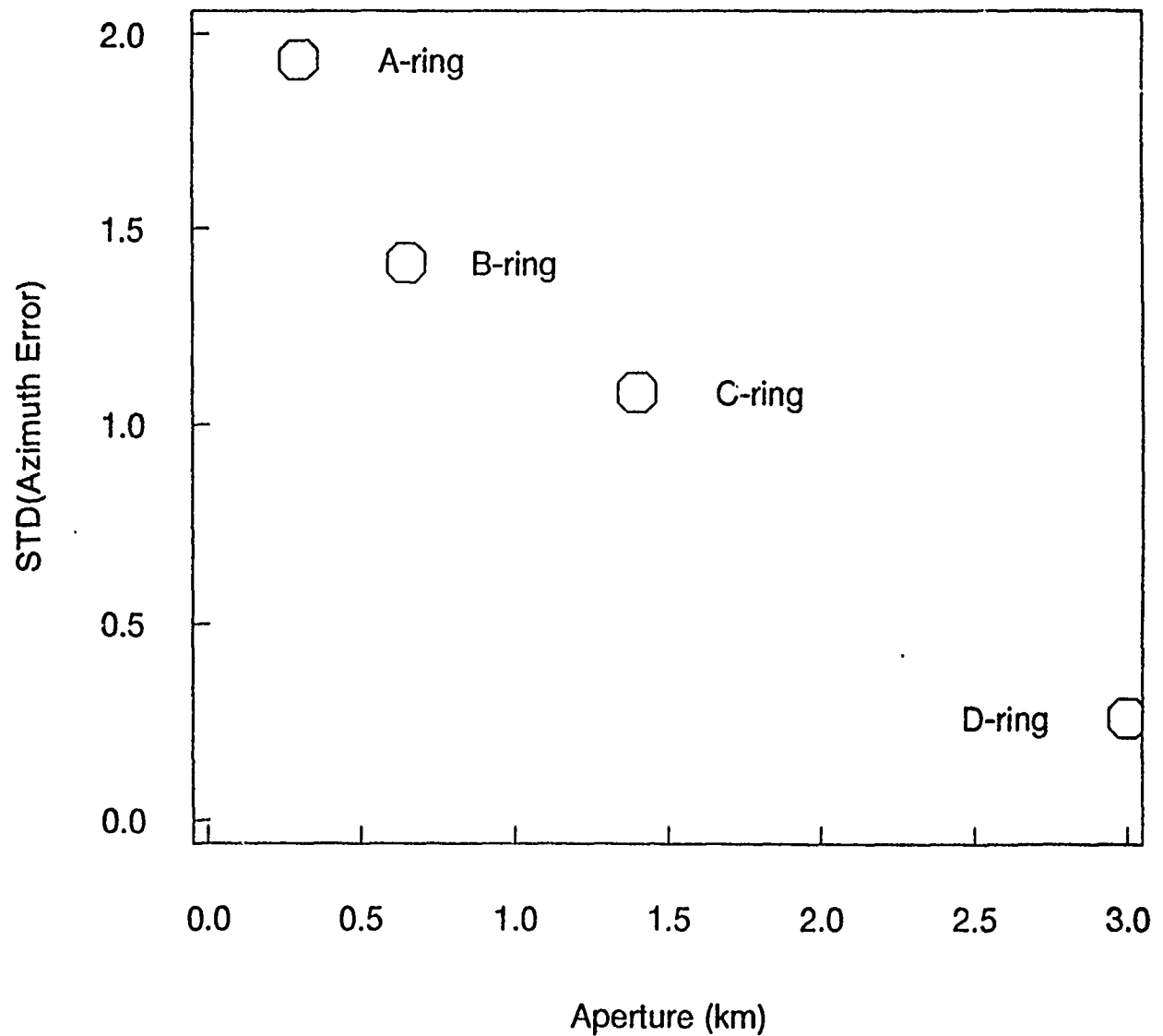


Figure 9. Standard deviation of azimuth error for 11 events in southwestern Balapan as a function of array ring.

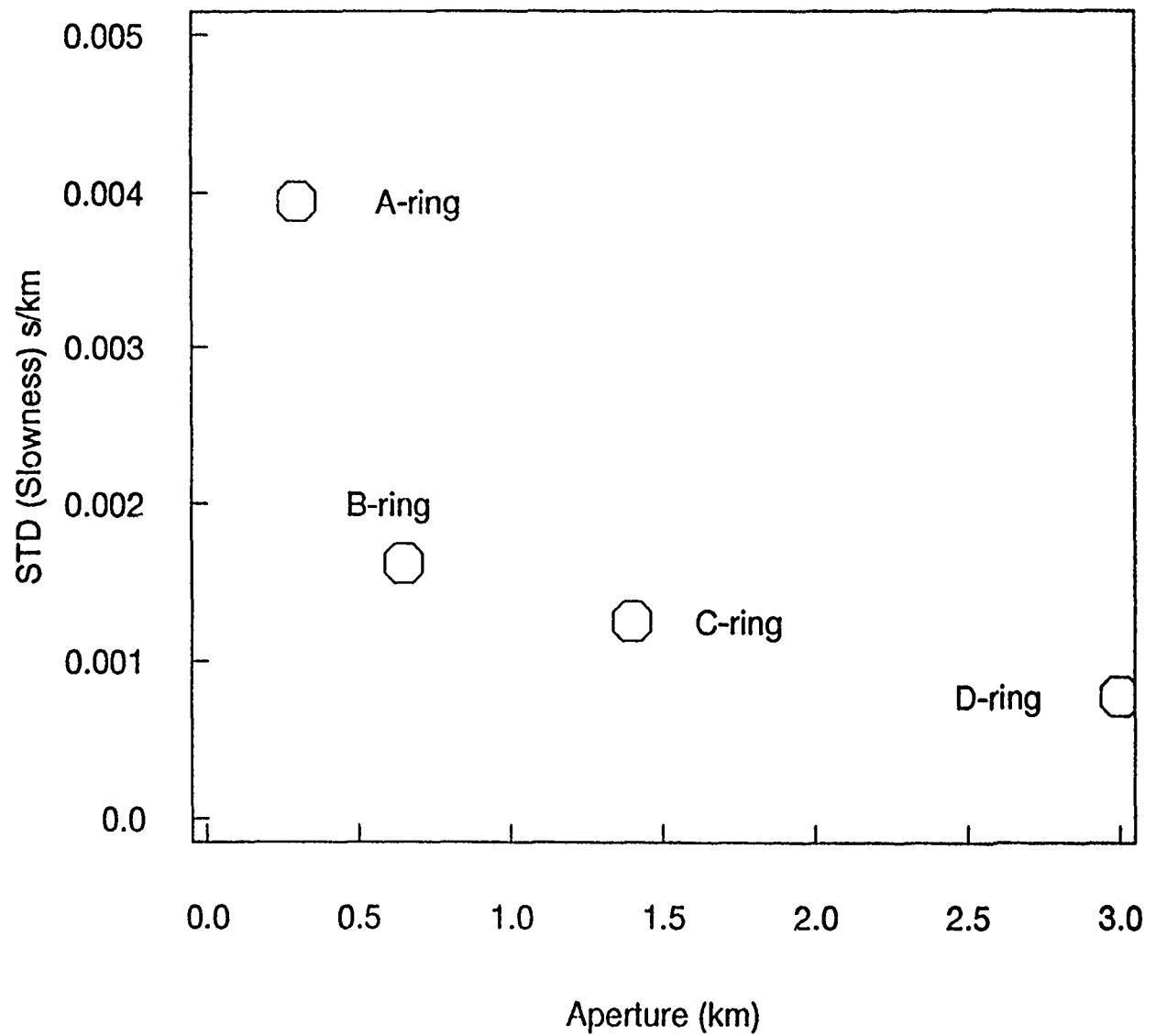


Figure 10. Standard deviation of slowness error for 11 events in southwestern Balapan as a function of array ring.

Figure 11 shows the azimuth error as a function of theoretical azimuth for the D-ring estimates. We have included the data for the two events in the northeastern Balapan. These two data points fall in the lower left corner of the diagram, which corresponds to a shift of 1.7° for a change in theoretical azimuth of about only 0.3°. This shift in azimuth is caused by shifts in the element corrections, c_{ik} , for the two northeastern Balapan events relative to the average corrections, \bar{c}_i , for the southwestern Balapan events. *Figure 12* shows the residuals, $c_{ik} - \bar{c}_i$, for the two events. Positive and negative shifts of about 5 ms can be noticed.

Comparison with f-k analysis

For the sake of comparison, azimuth and slowness values were also calculated using *f-k* analysis, which has become a standard processing techniques for small aperture seismic arrays. The algorithm based on broad band *f-k* analysis at the Center for Seismic Studies was employed for this purpose. Data for all elements were used (except for channels with spurious data). The *f-k* analysis was applied to the same data windows as used in the correlation analysis here. The standard deviations in the azimuth and slowness errors for the 11 events in the southwestern part of the Balapan test site were 1.45° and 0.0019 s/km, respectively. This azimuth error is comparable to that of the B-ring data and about five times the D-ring error in *Figure 9*.

Planarity of the wavefront

Up to this point we have compared the time delays with values corresponding to a plane wavefront derived from a *theoretical velocity model*. The time delays can, of course, also be used to *estimate* the slowness and azimuth of a plane wavefront without applying any element corrections. Such estimates will in all likelihood be biased, but it is of some interest to see how well the time delays fit those of an *estimated* plane wavefront.

Because of the differences in elevation among the array elements, we estimate the components of a three dimensional slowness vector ($\bar{p}_k = (p_{xk}, p_{yk}, p_{zk})$) for event k from a least squares fit to the time delays:

$$\bar{r}_{ij} \cdot \bar{p}_k = \tau_{ijk} \quad (i=1, \dots, n-1; j=i+1, \dots, n)$$

Errors in the estimated values for azimuth and horizontal slowness, i.e., $\text{atan}(p_x/p_y)$ and $(p_x^2 + p_y^2)^{1/2}$, for the 11 events at southwestern Balapan were $6.28 \pm 0.80^\circ$ and -0.0088 ± 0.0014 s/km, respectively. The vertical slowness p_z is related to the surface P-wave velocity, v , and the horizontal slowness by:

$$\frac{1}{v^2} = p_x^2 + p_y^2 + p_z^2.$$

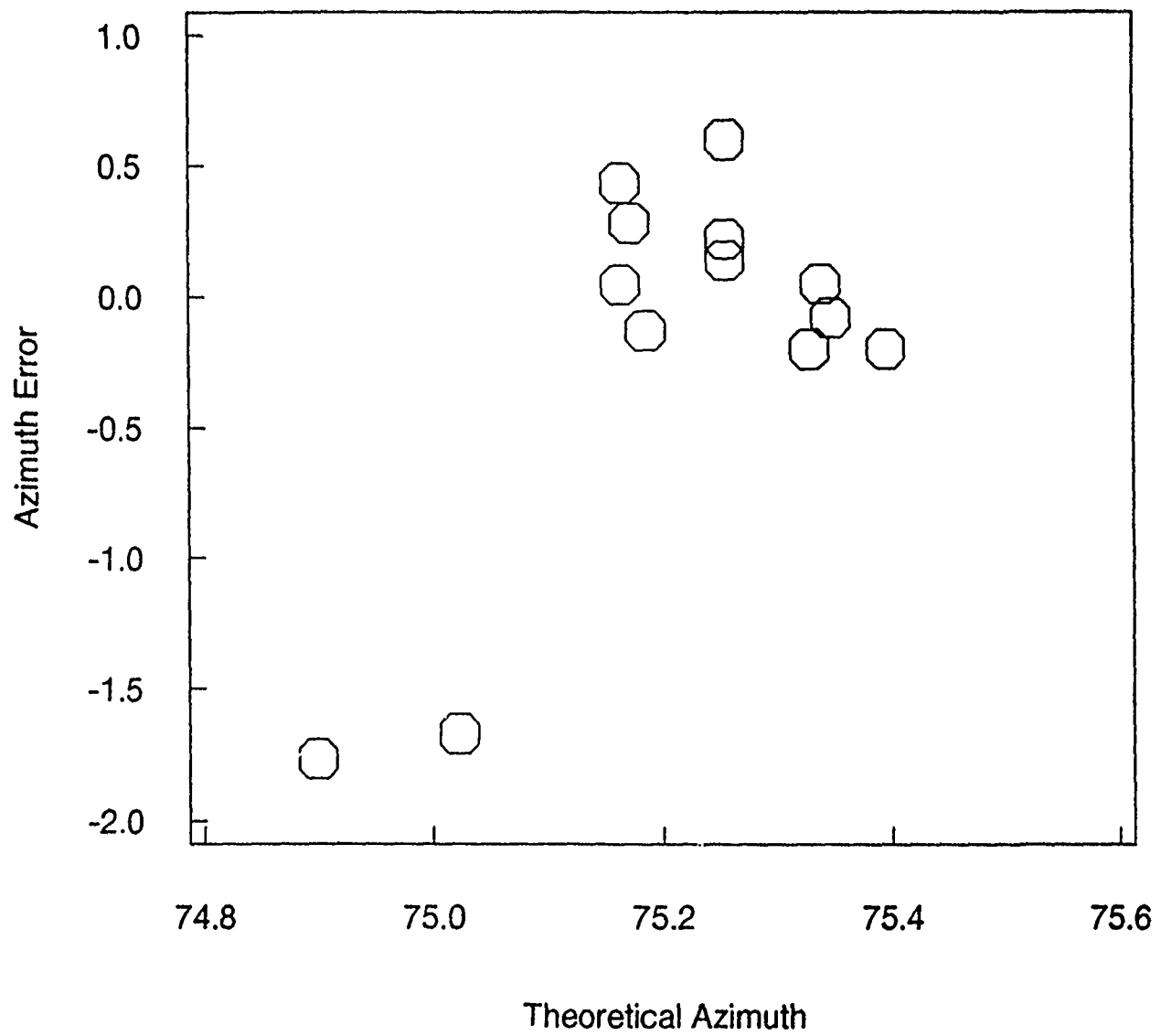


Figure 11. Azimuth error (from D-ring data) as a function of theoretical azimuth for all Balapan events.

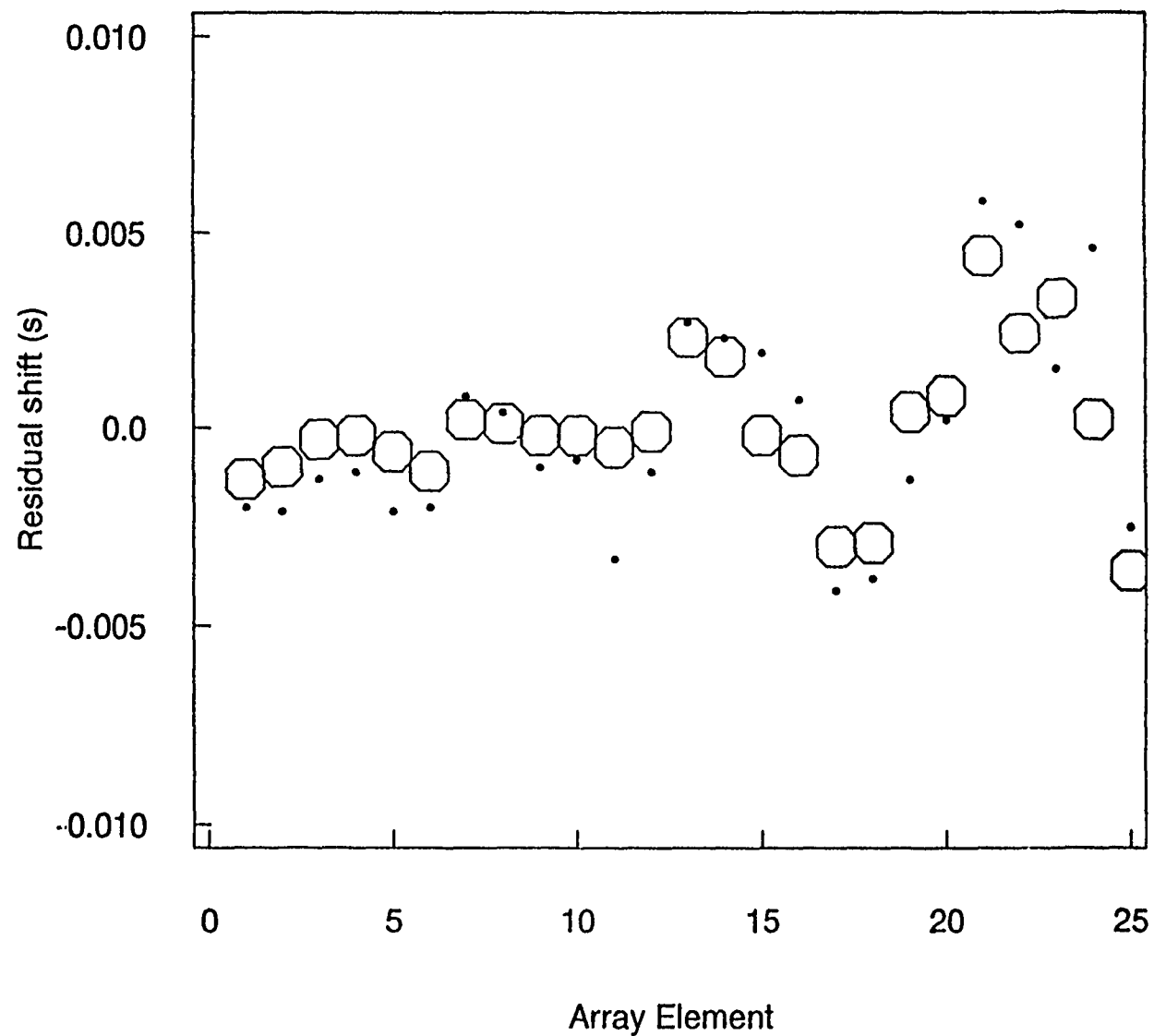


Figure 12. Difference between element corrections for events in northeastern Balapan (Dec 2 1984 and Nov 12 1988) and average corrections for five events in southwestern Balapan. The differences are quite similar for the two events.

Estimated mean and standard deviations of α from this relation for the 11 southwestern Balapan events were 6.1 ± 0.7 km/s.

The residuals, c_{ik} , from the estimated plane wavefront at element i for event k can be estimated in a way similar to the element corrections above:

$$c_{ik} - c_{jk} = r_{ij}\hat{p}_k \quad (i=1,\dots,n-1; j=i+1,\dots,n)$$

$$\sum_{i=1}^n c_{ik} = 0$$

here \hat{p}_k represent the 3-dimensional slowness vector already estimated from the time delays.

The average residual for the 11 events in southwestern Balapan has a standard deviation of $\sigma(c_i) = 4.5$ ms. For comparison, the standard deviation for data estimated by fitting a plane wave with only a *horizontal* slowness, i.e., only p_x and p_y components of \bar{p} , was 6.3 ms.

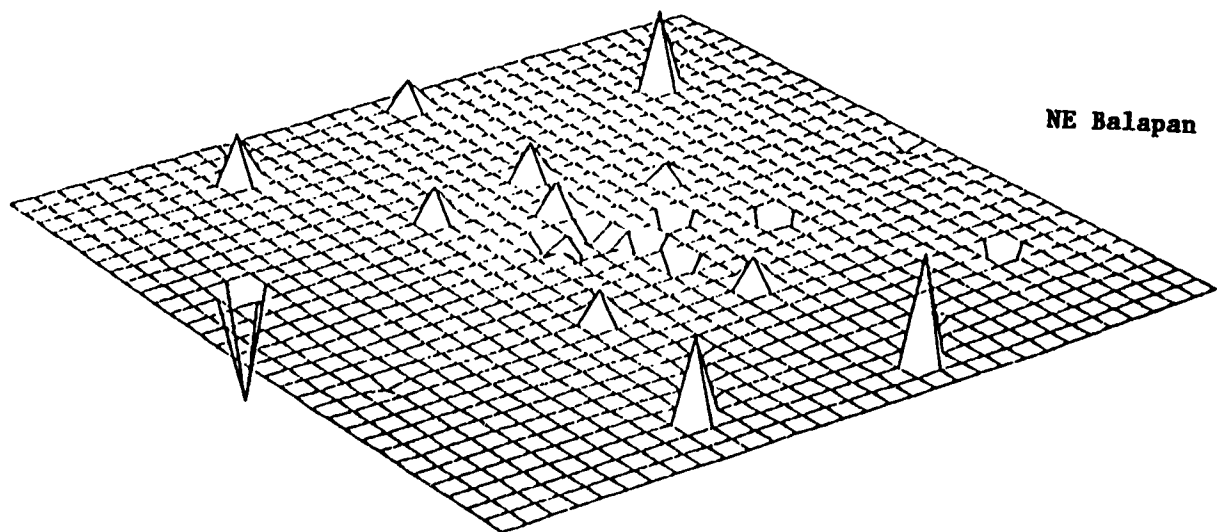
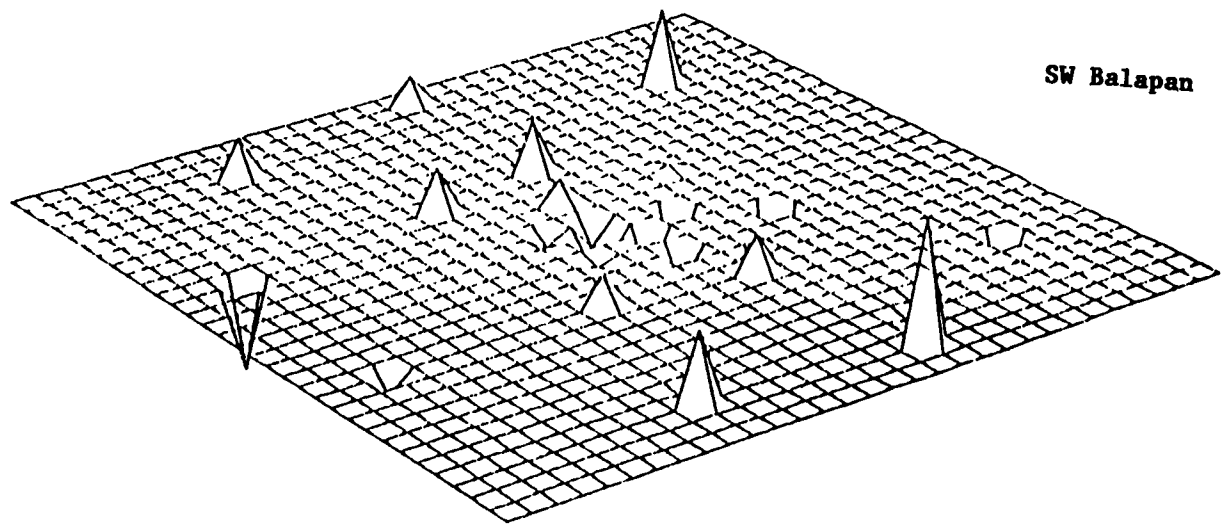
Average residuals for the 11 events in the southwestern part of Balapan, which range between -10 to 10 ms, are shown as a function of horizontal location in *Figure 13* in a perspective diagram. If the velocity below NORESS is about 6 km/s, this corresponds to an undulation of about 60 m of the wavefront over a horizontal distance of about 2.67 km (about one wavelength), which corresponds to about 2%. Positive and negative residuals divide the plane into two portions: the central northern and southern part of the array have positive residuals, whereas the east west and central parts have negative residuals. The residuals define the surface of the front of the initial P-wave.

The residuals are also plotted in the horizontal plane in *Figure 14*, where some features of the surface geology at the array are indicated (Mykkeltveit, 1987). Some of the "slow" portion of the wavefront coincides with a large tongue of gabbro extending almost due east from the center of the array.

The residuals for the two events in the northeastern part of Balapan are very similar to those of the southwestern part. However, the errors in azimuth and slowness are clearly different, 4.73° and -0.0066 s/km, respectively. *Figure 15* shows the direction of the normal to the estimated plane wavefronts (assuming the surface velocity $\alpha = 6$ km/s) projected on the lower hemisphere. It appears, therefore, as if the *shape* of the wavefronts from the two areas of Balapan are very similar, but they are slightly *tilted* relative to one another: differing by 1.55° in backazimuth and 0.82° relative to the vertical (incidence angle).

It might be more plausible to relate this tilt to the local structure beneath the NORESS array than to effects near the source regions or along the propagation

PLANE WAVE RESIDUALS



Maximum residual 10 ms

Figure 13. Perspective diagram of plane wave residuals plotted as a function of horizontal coordinates and second degree polynomial surface approximation to the residuals.

PLANE WAVE RESIDUALS

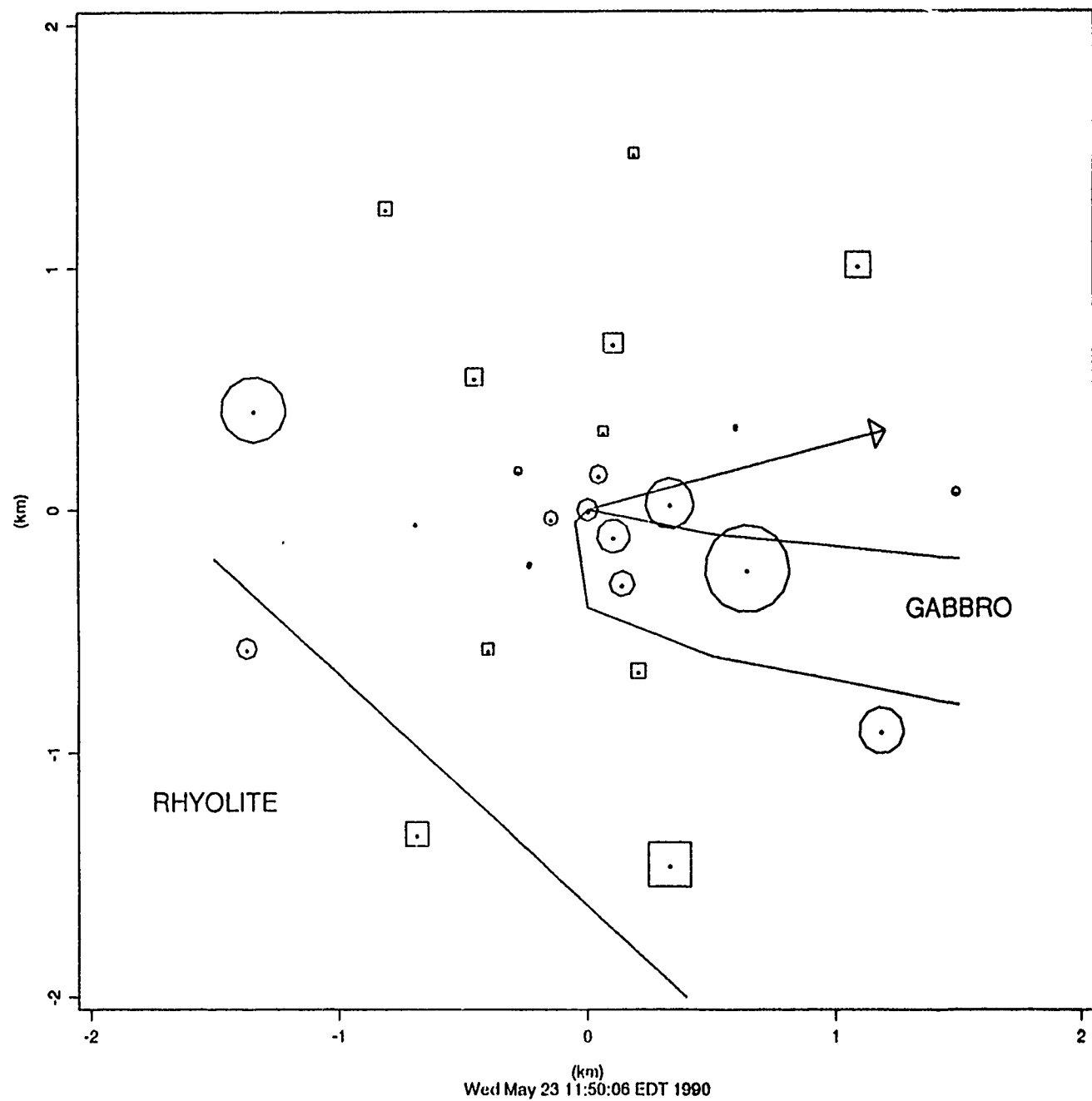


Figure 14. Plane wave residuals as a function of horizontal coordinates. Circles and squares are used for positive and negative values, respectively, corresponding to "slow" and "fast" portions of the wavefront. Some surface geological features (after Mykkeltveit, 1987) are indicated.

SHIFT IN DIRECTION OF PLANE WAVE

FOR SW AND NW BALAPAN EVENTS

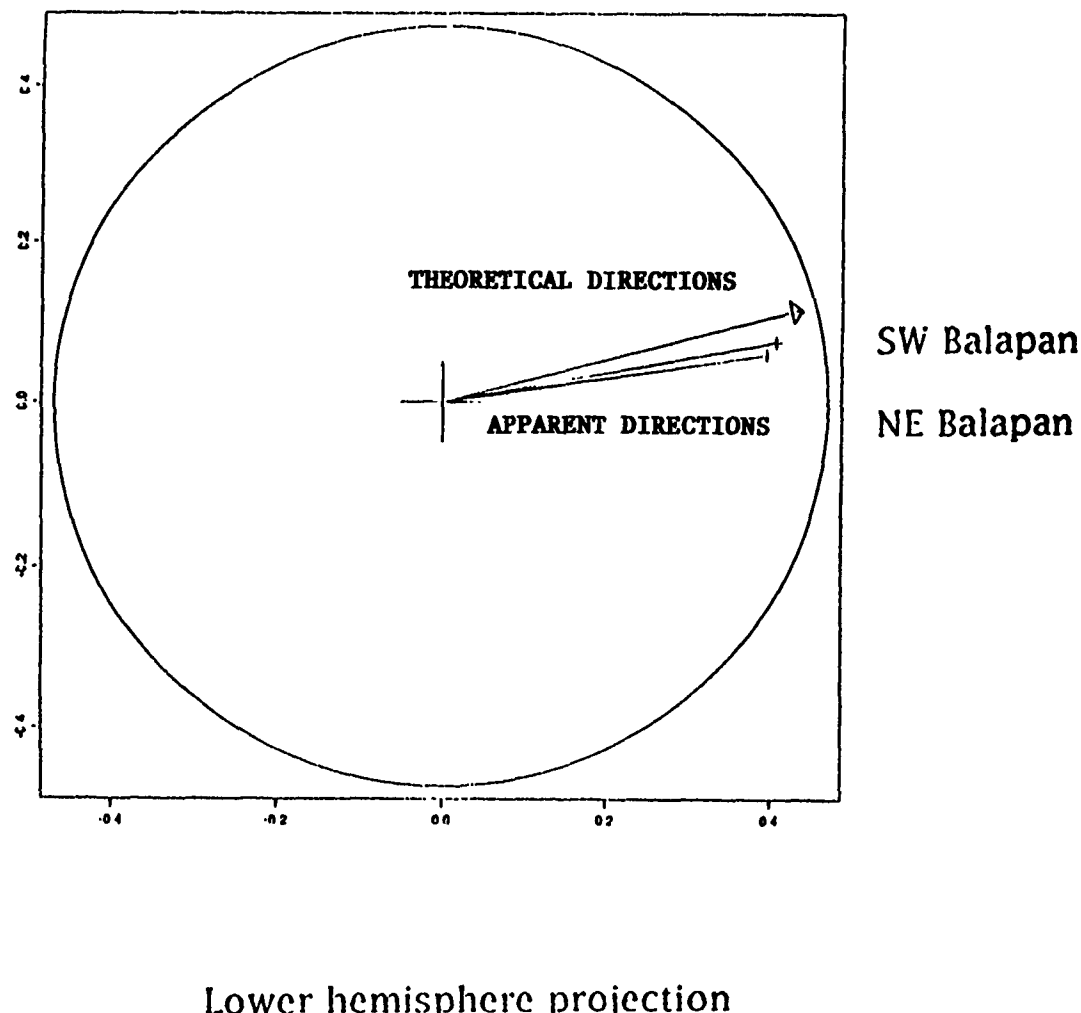


Figure 15. Lower hemisphere projection of the directions of a theoretical plane wave and apparent plane waves for the two portions of the Balapan test site.

paths. However, there are observations from teleseismic recordings at other seismic stations that show clear differences for the northeast and southwest sections of Balapan. Systematic differences in short period waveforms at the UK arrays were noted by Marshall *et al.* (1985), who also suggested that these differences might be due to systematic differences in corner frequencies of explosions at the two regions. Analyzing broad band recordings, Stewart (1988), however, suggests that the differences are more likely to be related to source depth of the explosions. Ringdal and Marshall (1989) suggested that the two sections of Balapan are characterized by different geophysical properties. They observed a systematic variation in the P-Lg bias for explosions across the Balapan region. For events with similar Lg magnitudes, the P amplitudes from explosions in the northeast were smaller than those from events in the southwest. If the tilt observed here is attributed to the near source structure it appears that the outgoing rays are deflected more strongly from events in the northeast than in the southwest part.

3.1.5 Concluding Remarks

In this study, we analyzed NORESS P-wave recordings for 15 explosions from the Balapan test site in E. Kazakh between 1984 and 1988. P-wave time delays between array element pairs were determined to the nearest ms from cross correlations of interpolated waveform data. The pattern of time delays shows high repeatability for events in the same area of Balapan.

Estimates of time delay corrections for the elements relative to delays for a theoretical plane wavefront varied between -19 to 31 ms. The standard error in the estimation was 0.7 ms. The element corrections correlate to some degree with element elevation.

Azimuth and slowness were estimated from the time delays and the element corrections. The best results were obtained if data from only the outer ring of NORESS were used. The standard deviations in azimuth and slowness estimates, 0.26 ° and 0.7 ms/degree, respectively, in this case were significantly smaller than those obtained from *f-k* analysis on the same data, 1.45 ° and 1.9 ms/km, respectively.

The average P-wave velocity below the NORESS array was estimated to be 6.1 ± 0.7 km/s by fitting the time delays to those of a three-dimensional plane wavefront.

Element travel-time residuals from the estimated plane wavefront varied between ± 10 ms. These residuals define a smooth surface for the wavefront of the initial P-wave. The maximum undulation of this surface was about 60 m or about 2% across one wavelength of the plane. The shape of wavefront surface was highly repeatable for all Balapan events, whereas the wavefronts for events in the southwestern and northeastern Balapan appeared to be tilted about 2 ° relative to

one another, which is about four times the theoretical value. This implies that outgoing rays from the Balapan area may be deflected more strongly in the near source region from events in the northeast section of the test site than from events in the southwestern section.

Hans Israelsson

References

- Mykkeltveit, S. (1987). Local Geology of the Regional Array Sites in Norway Semiannual Technical Summary, 1 Apr - 30 Sep 1987, NORSAR Sci. Rep. No. 1-87/88, Kjeller, Norway.
- Press, W.H., Flannery, B. P., Teukolsky, S.A. and W.T. Vetterling (1986). Numerical Recipes, The Art of Scientific Computing, Cambridge University Press, Cambridge, pp 818.
- Ringdal, F. and B.K. Hokland (1987). Magnitudes of Large Semipalatinsk Explosions using the P Coda and Lg Measurements at NORSAR, Semiannual Technical Summary, 1 Apr - 30 Sep 1987, NORSAR Sci. Rep. No. 1-87/88, Kjeller, Norway.
- Ringdal, F. and J. Fyen (1988). Analysis of Grafenberg Lg recordings of Semipalatinsk Explosions, Semiannual Technical Summary, 1 Oct 1987 - 31 March 1988, NORSAR Sci. Rep. No. 2-87/88, Kjeller, Norway.
- Marshall, P.D., T.C. Bache, and R.C. Lilwal (1985). Body wave magnitudes and locations of Soviet underground nuclear explosions at the Semipalatinsk test site, AWRE Report No. O 16/84 (re-issue), HMSO, London.
- Ringdal, F. and P.D. Marshall (1989). Yield determination of Soviet underground nuclear explosions at the Shagan River test site, in: Semiann. Tech. Summ. 1 Oct- 31 March 1989, NORSAR Sci. Rep. 2-22/89, Kjeller, Norway.
- Stewart, R.C. (1988). P-wave seismograms from underground nuclear explosions at the Shagan River Test Site recorded at four arrays, AWE Report No. O 4/88, HMSO, London.

25 FEB 1991

Prof. Thomas Ahrens
 Seismological Lab, 252-21
 Division of Geological & Planetary Sciences
 California Institute of Technology
 Pasadena, CA 91125

Prof. Charles B. Archambeau
 CIRES
 University of Colorado
 Boulder, CO 80309

Dr. Thomas C. Bache, Jr.
 Science Applications Int'l Corp.
 10260 Campus Point Drive
 San Diego, CA 92121 (2 copies)

Prof. Muawia Barazangi
 Institute for the Study of the Continent
 Cornell University
 Ithaca, NY 14853

Dr. Douglas R. Baumgardt
 ENSCO, Inc
 5400 Port Royal Road
 Springfield, VA 22151-2388

Prof. Jonathan Berger
 IGPP, A-025
 Scripps Institution of Oceanography
 University of California, San Diego
 La Jolla, CA 92093

Dr. Lawrence J. Burdick
 Woodward-Clyde Consultants
 566 El Dorado Street
 Pasadena, CA 91109-3245

Dr. Jerry Carter
 Center for Seismic Studies
 1300 North 17th St., Suite 1450
 Arlington, VA 22209-2308

Dr. Karl Coyner
 New England Research, Inc.
 76 Olcott Drive
 White River Junction, VT 05001

Prof. Vernon F. Cormier
 Department of Geology & Geophysics
 U-45, Room 207
 The University of Connecticut
 Storrs, CT 06268

Professor Anton W. Dainty
 Earth Resources Laboratory
 Massachusetts Institute of Technology
 42 Carleton Street
 Cambridge, MA 02142

Prof. Steven Day
 Department of Geological Sciences
 San Diego State University
 San Diego, CA 92182

Dr. Zoltan A. Der
 ENSCO, Inc.
 5400 Port Royal Road
 Springfield, VA 22151-2388

Prof. John Ferguson
 Center for Lithospheric Studies
 The University of Texas at Dallas
 P.O. Box 830688
 Richardson, TX 75083-0688

Dr. Mark D. Fisk
 Mission Research Corporation
 735 State Street
 P. O. Drawer 719
 Santa Barbara, CA 93102

Prof. Stanley Flatte
 Applied Sciences Building
 University of California
 Santa Cruz, CA 95064

Dr. Alexander Florence
 SRI International
 333 Ravenswood Avenue
 Menlo Park, CA 94025-3493

Prof. Henry L. Gray
 Vice Provost and Dean
 Department of Statistical Sciences
 Southern Methodist University
 Dallas, TX 75275

Dr. Indra Gupta
 Teledyne Geotech
 314 Montgomery Street
 Alexandria, VA 22314

Prof. David G. Harkrider
 Seismological Laboratory
 Division of Geological & Planetary Sciences
 California Institute of Technology
 Pasadena, CA 91125

Prof. Donald V. Helmberger
Seismological Laboratory
Division of Geological & Planetary Sciences
California Institute of Technology
Pasadena, CA 91125

Prof. Eugene Herrin
Institute for the Study of Earth and Man
Geophysical Laboratory
Southern Methodist University
Dallas, TX 75275

Prof. Bryan Isacks
Cornell University
Department of Geological Sciences
SNEE Hall
Ithaca, NY 14850

Dr Rong-Song Jih
Teledyne Geotech
314 Montgomery Street
Alexandria, VA 22314

Prof. Lane R. Johnson
Seismographic Station
University of California
Berkeley, CA 94720

Dr. Richard LaCoss
MIT-Lincoln Laboratory
M-200B
P. O. Box 73
Lexington, MA 02173-0073 (3 copies)

Prof Fred K. Lamb
University of Illinois at Urbana-Champaign
Department of Physics
1110 West Green Street
Urbana, IL 61801

Prof. Charles A. Langston
Geosciences Department
403 Deike Building
The Pennsylvania State University
University Park, PA 16802

Prof. Thorne Lay
Institute of Tectonics
Earth Science Board
University of California, Santa Cruz
Santa Cruz, CA 95064

Prof. Arthur Lerner-Lam
Lamont-Doherty Geological Observatory
of Columbia University
Palisades, NY 10964

Dr. Christopher Lynnes
Teledyne Geotech
314 Montgomery Street
Alexandria, VA 22314

Professor Peter E. Malin
Department of Geology
Old Chemistry Building
Duke University
Durham, NC 27706

Dr. Randolph Martin, III
New England Research, Inc.
76 Olcott Drive
White River Junction, VT 05001

Prof. Thomas V. McEvilly
Seismographic Station
University of California
Berkeley, CA 94720

Dr. Keith L. McLaughlin
S-CUBED
A Division of Maxwell Laboratory
P.O. Box 1620
La Jolla, CA 92038-1620

Prof. William Menke
Lamont-Doherty Geological Observatory
of Columbia University
Palisades, NY 10964

Stephen Miller
SRI International
333 Ravenswood Avenue
Box AF 116
Menlo Park, CA 94025-3493

Prof. Bernard Minster
IGPP, A-025
Scripps Institute of Oceanography
University of California, San Diego
La Jolla, CA 92093

Prof. Brian J. Mitchell
Department of Earth & Atmospheric Sciences
St. Louis University
St. Louis, MO 63156

Mr. Jack Murphy
S-CUBED, A Division of Maxwell Laboratory
11800 Sunrise Valley Drive
Suite 1212
Reston, VA 22091 (2 copies)

Prof. John A. Orcutt
IGPP, A-025
Scripps Institute of Oceanography
University of California, San Diego
La Jolla, CA 92093

Prof. Keith Priestley
University of Cambridge
Bullard Labs, Dept. of Earth Sciences
Madingley Rise, Madingley Rd.
Cambridge CB3 OEZ, ENGLAND

Dr. Jay J. Pulli
Radix Systems, Inc.
2 Taft Court, Suite 203
Rockville, MD 20850

Prof. Paul G. Richards
Lamont Doherty Geological Observatory
of Columbia University
Palisades, NY 10964

Dr. Wilmer Rivers
Teledyne Geotech
314 Montgomery Street
Alexandria, VA 22314

Prof. Charles G. Sammis
Center for Earth Sciences
University of Southern California
University Park
Los Angeles, CA 90089-0741

Prof. Christopher H. Scholz
Lamont-Doherty Geological Observatory
of Columbia University
Palisades, NY 10964

Thomas J. Sereno, Jr.
Science Application Int'l Corp.
10260 Campus Point Drive
San Diego, CA 92121

Prof. David G. Simpson
Lamont-Doherty Geological Observatory
of Columbia University
Palisades, NY 10964

Dr. Jeffrey Stevens
S-CUBED
A Division of Maxwell Laboratory
P.O. Box 1620
La Jolla, CA 92038-1620

Prof. Brian Stump
Institute for the Study of Earth & Man
Geophysical Laboratory
Southern Methodist University
Dallas, TX 75275

Prof. Jeremiah Sullivan
University of Illinois at Urbana-Champaign
Department of Physics
1110 West Green Street
Urbana, IL 61801

Prof. Clifford Thurber
University of Wisconsin-Madison
Department of Geology & Geophysics
1215 West Dayton Street
Madison, WI 53706

Prof. M. Nafi Toksoz
Earth Resources Lab
Massachusetts Institute of Technology
42 Carleton Street
Cambridge, MA 02142

Prof. John E. Vidale
University of California at Santa Cruz
Seismological Laboratory
Santa Cruz, CA 95064

Prof. Terry C. Wallace
Department of Geosciences
Building #77
University of Arizona
Tucson, AZ 85721

Dr. William Wortman
Mission Research Corporation
735 State Street
P. O. Drawer 719
Santa Barbara, CA 93102

OTHERS (UNITED STATES)

Dr. Monem Abdel-Gawad
Rockwell International Science Center
1049 Camino Dos Rios
Thousand Oaks, CA 91360

Prof. Keiiti Aki
Center for Earth Sciences
University of Southern California
University Park
Los Angeles, CA 90089-0741

Prof. Shelton S. Alexander
Geosciences Department
403 Deike Building
The Pennsylvania State University
University Park, PA 16802

Dr. Kenneth Anderson
BBNSTC
Mail Stop 14/1B
Cambridge, MA 02238

Dr. Ralph Archuleta
Department of Geological Sciences
University of California at Santa Barbara
Santa Barbara, CA 93102

Dr. Jeff Barker
Department of Geological Sciences
State University of New York
at Binghamton
Vestal, NY 13901

Dr. Susan Beck
Department of Geosciences
Bldg. # 77
University of Arizona
Tucson, AZ 85721

Dr. T.J. Bennett
S-CUBED
A Division of Maxwell Laboratory
11800 Sunrise Valley Drive, Suite 1212
Reston, VA 22091

Mr. William J. Best
907 Westwood Drive
Vienna, VA 22180

Dr. N. Biswas
Geophysical Institute
University of Alaska
Fairbanks, AK 99701

Dr. G.A. Bollinger
Department of Geological Sciences
Virginia Polytechnical Institute
21044 Derring Hall
Blacksburg, VA 24061

Dr. Stephen Bratt
Center for Seismic Studies
1300 North 17th Street
Suite 1450
Arlington, VA 22209

Michael Browne
Teledyne Geotech
3401 Shiloh Road
Garland, TX 75041

Mr. Roy Burger
1221 Serry Road
Schenectady, NY 12309

Dr. Robert Burridge
Schlumberger-Doll Research Center
Old Quarry Road
Ridgefield, CT 06877

Dr. W. Winston Chan
Teledyne Geotech
314 Montgomery Street
Alexandria, VA 22314-1581

Dr. Theodore Cherry
Science Horizons, Inc.
710 Encinitas Blvd., Suite 200
Encinitas, CA 92024 (2 copies)

Prof. Jon F. Claerbout
Department of Geophysics
Stanford University
Stanford, CA 94305

Prof. Robert W. Clayton
Seismological Laboratory
Division of Geological & Planetary Sciences
California Institute of Technology
Pasadena, CA 91125

Prof. F. A. Dahlen
Geological and Geophysical Sciences
Princeton University
Princeton, NJ 08544-0636

Mr. Charles Doll
Earth Resources Laboratory
Massachusetts Institute of Technology
42 Carleton St.
Cambridge, MA 02142

Dr. Jeffrey W. Given
SAIC
10260 Campus Point Drive
San Diego, CA 92121

Prof. Adam Dziewonski
Hoffman Laboratory, Harvard Univ.
Dept. of Earth Atmos. & Planetary Sciences
20 Oxford St
Cambridge, MA 02138

Prof. Stephen Grand
University of Texas at Austin
Department of Geological Sciences
Austin, TX 78713-7909

Prof. John Ebel
Department of Geology & Geophysics
Boston College
Chestnut Hill, MA 02167

Prof. Roy Greenfield
Geosciences Department
403 Deike Building
The Pennsylvania State University
University Park, PA 16802

Eric Fielding
SNEE Hall
INSTOC
Cornell University
Ithaca, NY 14853

Dan N. Hagedorn
Battelle
Pacific Northwest Laboratories
Battelle Boulevard
Richland, WA 99352

Dr. John Foley
Phillips Laboratory - OL-AA/LWH
Hanscom AFB, MA 01731-5000

Dr. James Hannon
Lawrence Livermore National Laboratory
P. O. Box 808
Livermore, CA 94550

Prof. Donald Forsyth
Department of Geological Sciences
Brown University
Providence, RI 02912

Prof. Robert B. Herrmann
Dept. of Earth & Atmospheric Sciences
St. Louis University
St. Louis, MO 63156

Dr. Cliff Frolich
Institute of Geophysics
8701 North Mopac
Austin, TX 78759

Ms. Heidi Houston
Seismological Laboratory
University of California
Santa Cruz, CA 95064

Dr. Anthony Gangi
Texas A&M University
Department of Geophysics
College Station, TX 77843

Kevin Hutchenson
Department of Earth Sciences
St. Louis University
3507 Laclede
St. Louis, MO 63103

Dr. Freeman Gilbert
IGPP, A-025
Scripps Institute of Oceanography
University of California
La Jolla, CA 92093

Dr. Hans Israelsson
Center for Seismic Studies
1300 N. 17th Street, Suite 1450
Arlington, VA 22209-2308

Mr. Edward Giller
Pacific Sierra Research Corp.
1401 Wilson Boulevard
Arlington, VA 22209

Prof. Thomas H. Jordan
Department of Earth, Atmospheric
and Planetary Sciences
Massachusetts Institute of Technology
Cambridge, MA 02139

Prof. Alan Kafka
Department of Geology & Geophysics
Boston College
Chestnut Hill, MA 02167

Robert C. Kemerait
ENSCO, Inc.
445 Pineda Court
Melbourne, FL 32940

William Kikendall
Teledyne Geotech
3401 Shiloh Road
Garland, TX 75041

Prof. Leon Knopoff
University of California
Institute of Geophysics & Planetary Physics
Los Angeles, CA 90024

Prof. L. Timothy Long
School of Geophysical Sciences
Georgia Institute of Technology
Atlanta, GA 30332

Dr. Gary McCartor
Department of Physics
Southern Methodist University
Dallas, TX 75275

Prof. Art McGarr
Mail Stop 977
Geological Survey
345 Middlefield Rd.
Menlo Park, CA 94025

Dr. George Mellman
Sierra Geophysics
11255 Kirkland Way
Kirkland, WA 98033

Prof. John Nabelek
College of Oceanography
Oregon State University
Corvallis, OR 97331

Prof. Geza Nagy
University of California, San Diego
Department of Ames, M.S. B-010
La Jolla, CA 92093

Dr. Keith K. Nakanishi
Lawrence Livermore National Laboratory
L-205
P. O. Box 808
Livermore, CA 94550

Dr. Bao Nguyen
Phillips Laboratory - OL-AA/LWH
Hanscom AFB, MA 01731-5000

Prof. Amos Nur
Department of Geophysics
Stanford University
Stanford, CA 94305

Prof. Jack Oliver
Department of Geology
Cornell University
Ithaca, NY 14850

Dr. Kenneth Olsen
P. O. Box 1273
Linwood, WA 98046-1273

Howard J. Patton
Lawrence Livermore National Laboratory
L-205
P. O. Box 808
Livermore, CA 94550

Prof. Robert Phinney
Geological & Geophysical Sciences
Princeton University
Princeton, NJ 08544-0636

Dr. Paul Pomeroy
Rondout Associates
P.O. Box 224
Stone Ridge, NY 12484

Dr. Norton Rimer
S-CUBED
A Division of Maxwell Laboratory
P.O. Box 1620
La Jolla, CA 92038-1620

Prof. Larry J. Ruff
Department of Geological Sciences
1006 C.C. Little Building
University of Michigan
Ann Arbor, MI 48109-1063

Dr. Richard Sailor
TASC Inc.
55 Walkers Brook Drive
Reading, MA 01867

Prof. Pradeep Talwani
Department of Geological Sciences
University of South Carolina
Columbia, SC 29208

Dr. Susan Schwartz
Institute of Tectonics
1156 High St.
Santa Cruz, CA 95064

Dr. David Taylor
ENSCO, Inc.
445 Pineda Court
Melbourne, FL 32940

John Sherwin
Teledyne Geotech
3401 Shiloh Road
Garland, TX 75041

Dr. Steven R. Taylor
Lawrence Livermore National Laboratory
L-205
P. O. Box 808
Livermore, CA 94550

Dr. Matthew Sibol
Virginia Tech
Seismological Observatory
4044 Derring Hall
Blacksburg, VA 24061-0420

Professor Ta-Liang Teng
Center for Earth Sciences
University of Southern California
University Park
Los Angeles, CA 90089-0741

Dr. Albert Smith
Lawrence Livermore National Laboratory
L-205
P. O. Box 808
Livermore, CA 94550

Dr. Gregory van der Vink
IRIS, Inc.
1616 North Fort Myer Drive
Suite 1440
Arlington, VA 22209

Prof. Robert Smith
Department of Geophysics
University of Utah
1400 East 2nd South
Salt Lake City, UT 84112

Professor Daniel Walker
University of Hawaii
Institute of Geophysics
Honolulu, HI 96822

Dr. Stewart W. Smith
Geophysics AK-50
University of Washington
Seattle, WA 98195

William R. Walter
Seismological Laboratory
University of Nevada
Reno, NV 89557

Donald L. Springer
Lawrence Livermore National Laboratory
L-205
P. O. Box 808
Livermore, CA 94550

Dr. Raymond Willeman
Phillips Laboratory - OL-AA/LWH
Hanscom AFB, MA 01731-5000

Dr. George Sutton
Rondout Associates
P.O. Box 224
Stone Ridge, NY 12484

Dr. Gregory Wojcik
Weidlinger Associates
4410 El Camino Real
Suite 110
Los Altos, CA 94022

Prof. L. Sykes
Lamont-Doherty Geological Observatory
of Columbia University
Palisades, NY 10964

Dr. Lorraine Wolf
Phillips Laboratory - OL-AA/LWH
Hanscom AFB, MA 01731-5000

Prof. Francis T. Wu
Department of Geological Sciences
State University of New York
at Binghamton
Vestal, NY 13901

Dr. Gregory B. Young
ENSCO, Inc.
5400 Port Royal Road
Springfield, VA 22151-2388

Dr. Eileen Vergino
Lawrence Livermore National Laboratory
L-205
P. O. Box 808
Livermore, CA 94550

J. J. Zucca
Lawrence Livermore National Laboratory
P. O. Box 808
Livermore, CA 94550

GOVERNMENT

Dr. Ralph Alewine III
DARPA/NMRO
1400 Wilson Boulevard
Arlington, VA 22209-2308

Mr. James C. Battis
Phillips Laboratory - OL-AA/LWH
Hanscom AFB, MA 01731-5000

Dr. Robert Blandford
AFTAC/TT
Center for Seismic Studies
1300 North 17th St. Suite 1450
Arlington, VA 22209-2308

Eric Chael
Division 9241
Sandia Laboratory
Albuquerque, NM 87185

Dr. John J. Cipar
Phillips Laboratory - OL-AA/LWH
Hanscom AFB, MA 01731-5000

Cecil Davis
Group P-15, Mail Stop D406
P.O. Box 1663
Los Alamos National Laboratory
Los Alamos, NM 87544

Mr. Jeff Duncan
Office of Congressman Markey
2133 Rayburn House Bldg.
Washington, DC 20515

Dr. Jack Evernden
USGS - Earthquake Studies
345 Middlefield Road
Menlo Park, CA 94025

Art Frankel
USGS
922 National Center
Reston, VA 22092

Dr. Dale Glover
DIA/DT-1B
Washington, DC 20301

Dr. T. Hanks
USGS
Nat'l Earthquake Research Center
345 Middlefield Road
Menlo Park, CA 94025

Dr. Roger Hansen
AFTAC/TT
Patrick AFB, FL 32925

Paul Johnson
ESS-4, Mail Stop J979
Los Alamos National Laboratory
Los Alamos, NM 87545

Janet Johnston
Phillips Laboratory - OL-AA/LWH
Hanscom AFB, MA 01731-5000

Dr. Katharine Kadinsky-Cade
Phillips Laboratory - OL-AA/LWH
Hanscom AFB, MA 01731-5000

Ms. Ann Kerr
IGPP, A-025
Scripps Institute of Oceanography
University of California, San Diego
La Jolla, CA 92093

Dr. Max Koontz
US Dept of Energy/DP 5
Forrestal Building
1000 Independence Avenue
Washington, DC 20585

Dr. W.H.K. Lee
Office of Earthquakes, Volcanoes,
& Engineering
345 Middlefield Road
Menlo Park, CA 94025

Dr. William Leith
U.S. Geological Survey
Mail Stop 928
Reston, VA 22092

Dr. Richard Lewis
Director, Earthquake Engineering & Geophysics
U.S. Army Corps of Engineers
Box 631
Vicksburg, MS 39180

James F. Lewkowicz
Phillips Laboratory - OL-AA/LWH
Hanscom AFB, MA 01731-5000

Dr. Frank F. Pilote
HQ AFTAC/TT
Patrick AFB, FL 32925-6001

Mr. Alfred Lieberman
ACDA/VI-OA'State Department Bldg
Room 5726
320 - 21st Street, NW
Washington, DC 20451

Stephen Mangino
Phillips Laboratory - OL-AA/LWH
Hanscom AFB, MA 01731-5000

Dr. Robert Massie
Box 25046, Mail Stop 967
Denver Federal Center
Denver, CO 80225

Art McGarr
U.S. Geological Survey, MS-977
345 Middlefield Road
Menlo Park, CA 94025

Richard Morrow
ACDA/VI, Room 5741
320 21st Street N.W.
Washington, DC 20451

Dr. Carl Newton
Los Alamos National Laboratory
P.O. Box 1663
Mail Stop C335, Group ESS-3
Los Alamos, NM 87545

Dr. Kenneth H. Olsen
Los Alamos Scientific Laboratory
P. O. Box 1663
Mail Stop D-406
Los Alamos, NM 87545

Mr. Chris Paine
Office of Senator Kennedy
SR 315
United States Senate
Washington, DC 20510

Colonel Jerry J. Perrizo
AFOSR/NP, Building 410
Bolling AFB
Washington, DC 20332-6448

Katie Poley
CIA-ACIS/TMC
Room 4X16NHB
Washington, DC 20505

Mr. Jack Rachlin
U.S. Geological Survey
Geology, Rm 3 C136
Mail Stop 928 National Center
Reston, VA 22092

Dr. Robert Reinke
WL/NTESG
Kirtland AFB, NM 87117-6008

Dr. Byron Ristvet
HQ DNA, Nevada Operations Office
Attn: NVCG
P.O. Box 98539
Las Vegas, NV 89193

Dr. George Rothe
HQ AFTAC/TTR
Patrick AFB, FL 32925-6001

Dr. Alan S. Ryall, Jr.
DARPA/NMRO
1400 Wilson Boulevard
Arlington, VA 22209-2308

Dr. Michael Shore
Defense Nuclear Agency/SPSS
6801 Telegraph Road
Alexandria, VA 22310

Mr. Charles L. Taylor
Phillips Laboratory - OL-AA/LWH
Hanscom AFB, MA 01731-5000

Dr. Larry Turnbull
CIA-OSWR/NED
Washington, DC 20505

Dr. Thomas Weaver
Los Alamos National Laboratory
P.O. Box 1663, Mail Stop C335
Los Alamos, NM 87545

Defense Technical Information Center
Cameron Station
Alexandria, VA 22314 (5 copies)

Phillips Laboratory
Attn: OL-AA/SULL
Research Library
Hanscom AFB , MA 01731-5000 (2 copies)

Defense Intelligence Agency
Directorate for Scientific & Technical Intelligence
Attn: DT1B
Washington, DC 20340-6158

Secretary of the Air Force
(SAFRD)
Washington, DC 20330

AFTAC/CA
(STINFO)
Patrick AFB, FL 32925-6001

Office of the Secretary Defense
DDR & E
Washington, DC 20330

TACTEC
Battelle Memorial Institute
505 King Avenue
Columbus, OH 43201 (Final Report Only)

HQ DNA
Attn: Technical Library
Washington, DC 20305

DARPA/RMO/RETRIEVAL
1400 Wilson Boulevard
Arlington, VA 22209

DARPA/RMO/Security Office
1400 Wilson Boulevard
Arlington, VA 22209

Phillips Laboratory
ATTN: OL-AA/XO
Hanscom AFB, MA 01731-5000

Phillips Laboratory
ATTN: OL-AA/LW
Hanscom AFB, MA 01731-5000

DARPA/PM
1400 Wilson Boulevard
Arlington, VA 22209

CONTRACTORS (FOREIGN)

Dr. Ramon Cabre, S.J.
Observatorio San Calixto
Casilla 5939
La Paz, Bolivia

Prof. Hans-Peter Harjes
Institute for Geophysik
Ruhr University/Bochum
P.O. Box 102148
4630 Bochum 1, FRG

Prof. Eystein Husebye
NTNF/NORSAR
P.O. Box 51
N-2007 Kjeller, NORWAY

Prof. Brian L.N. Kennett
Research School of Earth Sciences
Institute of Advanced Studies
G.P.O. Box 4
Canberra 2601, AUSTRALIA

Dr. Bernard Massinon
Societe Radiomana
27 rue Claude Bernard
75005 Paris, FRANCE (2 Copies)

Dr. Pierre Mecheler
Societe Radiomana
27 rue Claude Bernard
75005 Paris, FRANCE

Dr. Svein Mykkeltveit
NTNF/NORSAR
P.O. Box 51
N-2007 Kjeller, NORWAY (3 copies)

FOREIGN (OTHERS)

Dr. Peter Basham
Earth Physics Branch
Geological Survey of Canada
1 Observatory Crescent
Ottawa, Ontario, CANADA K1A 0Y3

Dr. Tormod Kvaerna
NTNF/NORSAR
P.O. Box 51
N-2007 Kjeller, NORWAY

Dr. Eduard Berg
Institute of Geophysics
University of Hawaii
Honolulu, HI 96822

Dr. Peter Marshall
Procurement Executive
Ministry of Defense
Blacknest, Brimpton
Reading RG7-4RS, UNITED KINGDOM

Dr. Michel Bouchon
I.R.I.G.M.-B.P. 68
38402 St. Martin D'Heres
Cedex, FRANCE

Prof. Ari Ben-Menahem
Department of Applied Mathematics
Weizman Institute of Science
Rehovot, ISRAEL 951729

Dr. Hilmar Bungum
NTNF/NORSAR
P.O. Box 51
N-2007 Kjeller, NORWAY

Dr. Robert North
Geophysics Division
Geological Survey of Canada
1 Observatory Crescent
Ottawa, Ontario, CANADA K1A 0Y3

Dr. Michel Campillo
Observatoire de Grenoble
I.R.I.G.M.-B.P. 53
38041 Grenoble, FRANCE

Dr. Frode Ringdal
NTNF/NORSAR
P.O. Box 51
N-2007 Kjeller, NORWAY

Dr. Kin Yip Chun
Geophysics Division
Physics Department
University of Toronto
Ontario, CANADA M5S 1A7

Dr. Jorg Schlittenhardt
Federal Institute for Geosciences & Nat'l Res.
Postfach 510153
D-3000 Hannover 51, FEDERAL REPUBLIC OF
GERMANY

Dr. Alan Douglas
Ministry of Defense
Blacknest, Brimpton
Reading RG7-4RS, UNITED KINGDOM

Universita Degli Studi Di Trieste
Facolta Di Ingegneria
Istituto Di Miniere E. Geofisica Applicata, Trieste,
ITALY

Dr. Manfred Henger
Federal Institute for Geosciences & Nat'l Res.
Postfach 510153
D-3000 Hanover 51, FRG

Dr. John Woodhouse
Oxford University
Dept of Earth Sciences
Parks Road
Oxford OX13PR, ENGLAND

Ms. Eva Johannsson
Senior Research Officer
National Defense Research Inst.
P.O. Box 27322
S-102 54 Stockholm, SWEDEN

Dr. Fekadu Kebede
Geophysical Observatory, Science Faculty
Addis Ababa University
P. O. Box 1176
Addis Ababa, ETHIOPIA